

© 2013 Gayathri Mohan

# A NEW DYNAMIC MODE FOR FAST IMAGING IN ATOMIC FORCE MICROSCOPES

BY

GAYATHRI MOHAN

DISSERTATION

Submitted in partial fulfillment of the requirements  
for the degree of Doctor of Philosophy in Mechanical Engineering  
in the Graduate College of the  
University of Illinois at Urbana-Champaign, 2013

Urbana, Illinois

Doctoral Committee:

Associate Professor Srinivasa M Salapaka, Chair  
Associate Professor Carolyn Beck  
Professor Naira Hovakimyan  
Assistant Professor Sanjiv Sinha  
Assistant Professor Kimani C Toussaint

# ABSTRACT

Video-rate imaging and property sensing with nanoscale precision is a subject of immense interest to scientists because it facilitates a deep understanding of processes and sample properties at a molecular level. This dissertation addresses the challenges of high-bandwidth imaging and real-time estimation of sample properties in an atomic force microscope (AFM).

Atomic force microscopy has enabled high-resolution nanoscale imaging and manipulation of mechanical, biological and chemical properties of samples at atomic scales. However, current atomic force microscopy techniques suffer from limited imaging bandwidths making them impractical for applications requiring high throughput.

A dynamic mode of imaging that achieves high imaging speeds while preserving the properties of high resolution and low forcing on the samples is developed. The proposed imaging scheme is particularly significant with the advent of high-speed nanopositioning stages and electronics. The design is accomplished by model-based force regulation that utilizes the fast cantilever deflection signal instead of its slower derivative signals used in existing methods. The control design uses the vertical and dither (shake) piezo-actuators to make the probe deflection signal track an appropriately designed trajectory. The underlying idea is to treat the nonlinear tip-sample interaction forces as an extraneous disturbance and derive an optimal control design for disturbance rejection with emphasis on robustness. The tracking objective guarantees force regulation between the probe-tip and the sample.  $\mathcal{H}_\infty$  stacked sensitivity framework is used to impose the control objectives and the optimal controller is derived through multiobjective optimization. The control design achieves disturbance rejection bandwidths of 0.15 – 0.20 times the first modal frequency of cantilever used for imaging. Consequently, in the presence of appropriate lateral positioning bandwidth, imaging speeds of the order of 15 – 20% of cantilever resonance frequency as compared to current speeds

(0.5 – 3%) are made possible.

The applications of AFMs go beyond just imaging sample topography. As against conventional imaging methods where the control signal serves as an estimate of the sample surface profile, the proposed imaging mode facilitates estimation of tip-sample interaction potential. The interaction forces are nonlinear functions of the tip-sample distance and their physical properties. Hence, force estimation enables estimation of sample's topography as well as its physical properties. Force models based on the nature of sample and experimental conditions are used to interpret the force estimate data. The choice of model used, in turn, impacts property estimation. A new signal is constructed using error signal from the tracking control problem in order to estimate the tip-sample interaction forces. Thus the goals of force regulation and estimation are separated, increasing the estimation bandwidth beyond the disturbance rejection bandwidth. This allows real-time estimation of sample properties across a scan. Moreover, since the force estimates and sample properties are obtained using the tracking error signal, the role of regulation is only to ensure that the cantilever tip tracks on the sample surface. The understanding of spatial variation of properties across a sample coupled with high-speed imaging will help realize the goal of using AFM as a nano-tool for recording dynamic biological processes.

*To my parents and my adviser.*

# ACKNOWLEDGMENTS

I would like to use this space to acknowledge and thank all the people who have made this thesis possible and my grad life in Champaign enjoyable.

First, I would like to thank my adviser Prof. Srinivasa Salapaka (aka Vasu). I feel fortunate to have had the opportunity to work with him for my Masters and PhD. I have benefited immensely from his mentorship. Amongst other things, he has imparted in me the importance of rigor while not losing track of the big picture. Its common knowledge that graduate research can get frustrating at times. At such times, I could always look up to Prof Vasu for advice and encouragement. I would also like to thank Prof Vasu for the numerous fun-filled lunch sessions. It was such a pleasure working with him and I hope to take ahead with me the many valuable things I have learnt from him in and out of research.

I would also like to express my gratitude to my doctoral committee, Prof Beck, Prof Hovakimyan, Prof Sinha and Prof Toussaint for their feedback and guidance. I am extremely grateful for the opportunities I had to interact with some of the greatest minds in research and attend their lectures at Illinois. In particular, I thoroughly enjoyed Prof Kumar's classes that taught me the significance of simple and clear presentation of ideas however complicated they may be.

I thank Dr Chibum Lee for his constant advice and support. I sincerely appreciate his efforts at collaboration in spite of major time zone differences and his other commitments. I would also like to thank my colleagues, Yunwen, Mashrafi, and in particular, Nachiket, Ramsai, Mayank and Srikanthan for helping me hook up my experiments. Thanks to Dr Scott Maclaren of MRL and Dr Anil Gannepalli of Asylum Research for their timely help with this work. I would like to thank all the friends I made at MechSE and Coordinated Science Laboratory (CSL) who have made graduate school a truly delightful experience

for me. Especially Neera, for some really memorable times, and much needed advice and encouragement over the years.

Life in Champaign would have been absolutely lackluster without the following wonderful people. The volleyball games, trips to Wok at Mahomet, extended lunches and evening chai, late-night mafia and pictionary, and coffee shop “work” sessions are only some of the many memories that I will cherish forever. It is hard to tell them apart from my family after all the lovely times spent together. Thank you, VJ, Sheeru, JK, Sathe, RG, Anand, Hemant, Jay, Rajan, Anjan, Dwarak, Jayanand, Shankar, Vivek, Jagan, and Kunal. I would also like to thank my closest friends outside Illinois, Nivi, Nafee, Ranju and Bala for their love and incessant words of encouragement.

I would like to express my heartfelt thanks to my family, my in-laws, Sachi uncle and Re aunty, for believing in me and encouraging me all the way, Ramya and Arun, for their love, constant support, help with proof-reading this thesis and fun-filled trips to Madison/Champaign, and Sowmya and Sriram, for inspiring and motivating me at times when I needed it the most.

I would like to convey my deepest thanks to my younger brother Mani for his love and support. Its hard for me to believe how much he has grown. I am so glad I could turn to him from time to time for technical and non-technical advice, and chats. And his daily dose of email forwards are a very welcome distraction from my routine.

I feel extremely blessed to have married my long-time friend Vignesh during graduate school. A long, long-distance relationship across the country is no joke, and I have no words to thank Vignesh for getting through it with me. He has always put up with my mood swings that came and went with the ups and downs of research and mid-west weather, with a calm and clear head on his shoulders. He is my biggest source of support and I am thankful to him for imparting some of his calmness into me along the way. Thanks to FaceTime, At&t and multiple airlines for helping us cope with the distance.

I have absolutely no words to thank my parents Visalakshi and Mohan for their unconditional love, support and confidence in me, and the many sacrifices they have made to make my life better. It will be a personal achievement if I can strive to be at least half as good as the people they are.

# TABLE OF CONTENTS

LIST OF FIGURES . . . . .	ix
LIST OF ABBREVIATIONS . . . . .	xi
LIST OF SYMBOLS . . . . .	xii
CHAPTER 1 INTRODUCTION . . . . .	1
1.1 Atomic Force Microscope . . . . .	1
1.1.1 Needs and Challenges . . . . .	2
1.2 High-Speed AFM: State-of-the-Art . . . . .	4
1.2.1 Cantilevers . . . . .	4
1.2.2 Positioners . . . . .	4
1.2.3 Role of Controls . . . . .	5
1.3 Scope of Thesis . . . . .	6
1.4 Structure of Thesis . . . . .	7
CHAPTER 2 IMAGING FRAMEWORK AND SYSTEMS VIEWPOINT . . . . .	9
2.1 AFM Operation . . . . .	9
2.1.1 Probe and Sensing . . . . .	10
2.1.2 Controller . . . . .	11
2.1.3 Piezo-Actuators . . . . .	11
2.2 Model for Imaging . . . . .	12
2.2.1 Cantilever Model . . . . .	12
2.2.2 Tip-Sample Interaction Models . . . . .	14
2.3 Modes of Scanning . . . . .	16
2.3.1 Static or Contact Mode Scanning . . . . .	16
2.3.2 Dynamic Mode Scanning . . . . .	18
2.4 Control System Perspective for Imaging . . . . .	21
2.4.1 AFM Imaging from Systems Viewpoint . . . . .	21
2.4.2 Systems Viewpoint for Tapping Mode Dynamic AFM . . . . .	22
2.5 Cantilever Subsystem and Tip-sample Model . . . . .	23
2.6 Proposed Control System Setup for High-speed Scanning . . . . .	24
2.7 Summary . . . . .	25



CHAPTER 3	HIGH-BANDWIDTH IMAGING MODE	27
3.1	Model Details	28
3.1.1	Non-dimensionalized State-space Representation	29
3.2	Reference Trajectory Design	30
3.2.1	Error Dynamics	31
3.3	Tip-Sample Interaction Forces as Disturbance	32
3.4	Control Design	33
3.4.1	Control Objectives	33
3.4.2	Disturbance Rejection	33
3.4.3	LMI Solution	36
3.4.4	Choice of Weighting Functions	40
3.4.5	Minimization Solution	43
3.5	Summary	46
CHAPTER 4	SAMPLE PROPERTY ESTIMATION	47
4.1	Disturbance Estimation	47
4.2	Topography and Property Estimation	50
4.2.1	Generic Force Model	51
4.2.2	Topography Estimates	53
4.2.3	Property Estimates	56
4.3	Summary	58
CHAPTER 5	EXPERIMENTAL RESULTS	60
5.1	Imaging in Air: Issues	60
5.2	Imaging in Fluids: Proof of Concept	61
5.2.1	Control Design	64
5.2.2	System Identification	65
5.2.3	Experiment Setup	69
5.3	Summary	72
CHAPTER 6	CONCLUSION	73
6.1	Summary and Analysis	73
6.2	Future Research Directions	74
APPENDIX A	ALTERNATE APPROACHES	76
A.1	BACKSTEPPING	76
A.2	S-PROCEDURE	80
APPENDIX B	AVERAGING METHODS FOR AMPLITUDE DYNAMICS	82
B.1	Using Lagrangian equations for $A$ , $\phi$ dynamics	82
B.1.1	Second order equations	82
B.1.2	Reduced - first order	83
REFERENCES		84

# LIST OF FIGURES

2.1	AFM Schematic . . . . .	10
2.2	Thermal response and second-order fit . . . . .	13
2.3	Force Vs tip-sample separation showing attractive and repulsive region . . . . .	15
2.4	Force curve using a cantilever under water . . . . .	16
2.5	Schematics of (a), constant force (static) mode and (b), amplitude modulation (dynamic) mode. . . . .	17
2.6	Frequency vs Amplitude curves . . . . .	19
2.7	Feedback framework for imaging . . . . .	21
2.8	Demodulation circuit used in tapping mode AFM operation . . . . .	23
2.9	Cantilever in feedback loop with tip-sample interaction force . . . . .	24
2.10	Systems representation for the proposed new dynamic mode of imaging in AFM . . . . .	25
3.1	Spring-mass-damper model for cantilever subsystem . . . . .	28
3.2	Schematic of error signal ( $\tilde{p}$ ) dynamics $\tilde{G}$ . . . . .	30
3.3	Closed-loop feedback diagram with $\tilde{G}$ and $K_1$ , treating inter-atomic forces between tip and sample as disturbance . . . . .	32
3.4	Closed-loop system with weighting functions for the $\mathcal{H}_\infty$ stacked sensitivity framework . . . . .	34
3.5	Open-loop system $P$ in feedback with the designed controller $K_1$ . . . . .	34
3.6	Weighting functions $W_s$ and $W_t$ for the design of closed-loop functions $S$ and $T$ . . . . .	41
3.7	Design of sensitivity function $S$ : Bode plot showing $S$ and the weighting function used $\frac{1}{W_s}$ . . . . .	41
3.8	Design of complementary sensitivity function $T$ : Bode plot showing $T$ and the weighting function used $\frac{1}{W_t}$ . . . . .	42
3.9	Magnitude and phase plots of the loop transfer function $L = \tilde{G}K_1$ . . . . .	42
3.10	Magnitude and phase plots of the closed-loop transfer function $\tilde{G}S$ . . . . .	43
3.11	Magnitude and phase plots of the the closed-loop transfer function $K_1S$ . . . . .	43
3.12	$\ \cdot\ _\infty$ norms of the terms in closed-loop matrix $\Phi$ . . . . .	44
3.13	(a) shows the normalized height profile used in simulation and (b) shows the output error signal $\tilde{y}$ . . . . .	44

4.1	The controller $K_2$ used to estimate the disturbance $\tilde{d}$ from the regulation error signal $e_m$ . . . . .	48
4.2	Bode diagram of the force estimating controller $K_2$ . . . . .	48
4.3	Performance of the force estimating controller $K_2$ shown through estimates of the disturbance $\tilde{d}$ , denoted by $\hat{\tilde{d}}$ . . . . .	49
4.4	Topography estimates . . . . .	53
4.5	Force curves using force estimate data . . . . .	55
4.6	The plot of the estimate $\hat{\tilde{d}}$ compared to original interaction force difference $\tilde{d}$	56
4.7	(a) and (b) Simulated force curves plotted against the force estimate data. (c) . . . . .	57
5.1	Comparison of unforced thermal responses for the same SiNi probe (a) in air and (b) immersed in water droplet. . . . .	62
5.2	Comparison of cantilever tuning with dither forcing for the same SiNi probe (a) in air and (b) immersed in water droplet. . . . .	63
5.3	Weighting functions $W_s$ and $W_t$ used for the design of closed-loop functions $S$ and $T$ for imaging in water. . . . .	65
5.4	Design of the sensitivity transfer function $S$ with $G_c$ transfer function for in-water imaging. . . . .	66
5.5	Design of the complementary sensitivity transfer function $T$ with $G_c$ transfer function for in-water imaging. . . . .	66
5.6	Designed closed-loop transfer function $K_1S$ with $G_c$ transfer function for in-water imaging. . . . .	67
5.7	The transfer function, $G_{zc}$ , identified between the $z$ piezo input $u_z$ and cantilever deflection $y$ . . . . .	68
5.8	The transfer function, $G_{dc}$ , identified between the dither piezo input $u_d$ and cantilever deflection $y$ . . . . .	68
5.9	Frequency response of the transfer function $Q_1$ in (5.4). . . . .	69
5.10	The transfer function identified between the $z$ piezo input $u_z$ and output $v$ . .	70
5.11	Closed-loop experimental arrangement. . . . .	70
5.12	Comparison of cantilever deflection and reference trajectory in current experimental set up . . . . .	71

# LIST OF ABBREVIATIONS

AFM	Atomic Force Microscope
AM	Amplitude Modulation
DMT	Derjaguin Muller Toropov
DSP	Digital Signal Processor
FM	Frequency Modulation
FPGA	Field Programmable Gate Array
JKR	Johnson Kendall Roberts
LMI	Linear Matrix Inequalities
ODE	Ordinary Differential Equation
PI	Proportional Integral Control
PID	Proportional Integral Differential Control
PII	Proportional Double-Integral (Integral-Integral) Control
PSD	Photo-Sensitive Diode
SPM	Scanning Probe Microscope
2DOF	Two Degree of Freedom

# LIST OF SYMBOLS

$\omega_n$	First natural frequency of cantilever
$Q$	Quality factor of cantilever
$n$	Measurement noise in system
$F(t)$	Forcing terms on cantilever
$\bar{z}$	Displacement (global) of cantilever
$\bar{y}$	Measured displacement of cantilever
$G_{therm}$	Cantilever transfer function based on unforced thermal response
$a$	Amplitude of oscillation of cantilever
$\phi$	Phase of oscillation of cantilever
$k$	Stiffness of cantilever
$F_{ts}$	Tip-sample interaction forces
$z_{ts}$	Tip-sample separation distance
$m$	Mass of cantilever
$\omega_r$	Shifted first natural frequency of cantilever in rad/s
$K$	Feedback controller
$G_z$	Modeled vertical or $z$ -piezo transfer function
$\mathcal{Q}$	Demodulator or similar dynamics
$g$	Dither actuation on cantilever
$h$	Sample profile or sample height
$\eta$	Thermal noise

$\mathcal{F}$	Tip-sample dynamic model
$u_z$	Control input to $z$ -piezo
$v$	$z$ -piezo actuation
$y_m$	Measured cantilever characteristic based on mode
$e$	Error between cantilever characteristic and set point
$r$	Reference set point/trajectory
$p_1$	Displacement (local) of cantilever
$p_m$	Measured displacement (local) of cantilever
$\omega$	Cantilever drive frequency
$G_c$	Cantilever model transfer function
$u_d$	Control input to dither piezo
$u_2$	Total control signal to cantilever
$G_d$	Modeled dither piezo transfer function
$g_0$	Amplitude of dither actuation
$I$	Identity function
$\zeta$	Damping coefficient of cantilever
$\bar{\omega}$	Normalizing frequency
$\tau$	Normalizing time unit
$\Omega$	Normalized cantilever drive frequency
$\Omega_n$	Normalized cantilever first resonance frequency
$p_0$	Initial condition of cantilever subsystem
$\hat{p}_0$	Initial condition of mock system
$\hat{G}$	Mock system dynamics
$\hat{p}$	Mock system state
$\hat{y}$	Mock system output or reference trajectory
$\hat{F}_{ts}$	Mock system force model
$\hat{d}$	Mock system disturbance

$\tilde{p}$	Error between cantilever subsystem and mock system states
$\tilde{G}$	Error system dynamics
$\mathbf{K}$	Set of feasible controllers
$K_1$	Regulating controller giving $u_2$
$e_m$	Error between cantilever deflection and reference trajectory
$\tilde{r}$	Error regulation set point
$\tilde{d}$	Disturbance to error system
$S$	Sensitivity transfer function
$T$	Complementary sensitivity transfer function
$W_s$	Weighting function corresponding to $S$ design
$W_t$	Weighting function corresponding to $T$ design
$W_u$	Weighting function to keep control bounded
$z_1$	Weighted output corresponding to $W_s$
$z_2$	Weighted output corresponding to $W_t$
$z_3$	Weighted output corresponding to $W_u$
$\Phi$	Closed-loop transfer function
$\hat{\tilde{d}}$	Disturbance estimate
$e_d$	Estimation error
$K_2$	Estimating controller
$E^*$	Effective Young's modulus between tip and sample
$R$	Tip radius
$\nu$	Poisson's ratio
$H$	Hamaker's constant
$a_0$	Inter-atomic distance
$\alpha$	Generalized force term for attractive region
$\beta$	Generalized force term for repulsive region 1
$\gamma$	Generalized force term for repulsive region 2

$m, n$	Generalized force model exponents
$z_s$	Shifted tip-sample separation distance ( $a_0 - z_{ts}$ )
$\Theta$	Averaged slope of tip-sample force
$G_{zc}$	Transfer function from $z$ -piezo input to cantilever deflection
$G_{dc}$	Transfer function from dither piezo input to cantilever deflection
$W_1$	Low-pass filter to assign control effort
$Q_1$	Transfer function from controller input to actuator inputs



# CHAPTER 1

## INTRODUCTION

This dissertation develops a dynamic mode of imaging for atomic force microscopes that significantly increases imaging bandwidth in these devices. The imaging mode also facilitates reliable dynamic estimates of interaction forces between the AFM probe and sample. These force estimates can be used to deduce topographical and physical properties of the sample under study. A systems viewpoint is adopted to understand and analyze the objectives and limitations of current imaging setup in AFMs. Consequently, the application of control techniques to overcome limitations of the existing imaging modes is investigated.

Section 1.1 provides a general overview of AFMs and current challenges that require attention. In Section 1.2 the state-of-the-art techniques in the area of high-speed imaging in AFM are outlined. Following this, the key contributions of this thesis towards the goal of high-speed imaging are presented in Section 1.3.

### 1.1 Atomic Force Microscope

Scanning probe microscopes refer to the class of devices that use micro-cantilever probes to sense forces and subsequently the properties of samples. The atomic force microscope is a front runner in this family of devices [1]. The probe or micro-cantilever of an AFM gives measurable deflections while sensing forces of  $(10^{-7} - 10^{-12})$  N, which has made the measurement of atomic-scale Van der Waals forces, electrostatic forces, capillary forces and friction forces possible. This ability of force sensing enables nanoscale investigation and manipulation of samples. Molecular resolution images were reported as early as the late 1980's following the invention of AFMs [2, 3].

During imaging, the most fundamental application of AFMs, the cantilever moves over

the sample surface within Angstrom level separation distances. Changes in the sample surface height features alters interaction forces between the cantilever tip and sample. The resultant displacements of the cantilever tip are monitored by a sensing mechanism and recorded to give a measure of the sample features. Feedback control is used to maintain desired operating conditions, which translates to constant tip-sample distance during basic imaging operations. In this case, the control signal is used as a measure of the sample's spatial topography. Current imaging techniques exhibit low bandwidths, primarily arising from the constraints imposed by the means of force regulation employed.

The most favored mode of scanning in atomic force microscopy, especially for soft bio-samples, is the tapping mode or amplitude modulation mode. Here the cantilever is oscillated sinusoidally at or near its resonance frequency using a small piezo-actuator. When the sample is moved under the probe, the amplitude and phase of oscillation change owing to the inter-atomic forces between the tip and sample. In typical tapping mode, feedback alters the vertical tip-sample distance to regulate the amplitude to a desired set-point thereby compensating for the features on the sample. This feedback signal forms the image of sample topography [4].

### 1.1.1 Needs and Challenges

The primary requirements to achieve the goal of nanoscale investigation of samples and processes can be classified as follows.

#### 1.1.1.1 Resolution

In order to understand and explore nanoscale processes, for example protein behavior, sub-atomic resolution is required. However, such ultra-high resolution imaging can often not be performed under ambient conditions. Sub-atomic resolutions have been demonstrated under vacuum and very low temperatures [5]. However, the behavior of materials under such conditions vary significantly from their behavior under normal conditions. Achieving such sub-atomic resolutions under normal scanning conditions poses severe challenges due to uncertainties in the environment. These remain to be addressed by the systems community.

#### 1.1.1.2 Robustness

Maintaining the high resolution sensing properties of the AFM despite the uncertainties presented by sensor, electronic and thermal noise, nonlinear nature of tip-sample interactions and diverse operating conditions and requirements is crucial. Therefore, robustness of devices to these uncertainties is of immense importance. However, in general the existing methods do not take this into consideration. Model-based control designs, on the other hand, accommodate robustness as a primary control objective [6, 7].

#### 1.1.1.3 Bandwidth

Pivotal to harnessing the vast potential of nano-investigation is the ability to interrogate at high speeds. This need arises from the requirement for probing sample features that have sub-nanometer dimensions over areas that have macroscopic dimensions. This range of scales necessitates large throughput rates to enable interrogation of practical sized samples with characteristic dimensions in the 1- $\mu\text{m}$  to 1-mm range.

Amplitude regulation in current AFMs yields good results since the lateral positioning bandwidths are about one percent of resonant frequencies of the cantilevers (1 kHz vs 100 kHz); and therefore the cantilever typically oscillates over many cycles before it experiences appreciable change in sample topography. Therefore, the amplitude, and equivalently the amplitude-regulating control effort provides a reliable measure of the sample topography. However, when the lateral bandwidths are higher, there is appreciable change in the topography even within one or few oscillation cycles. Therefore tapping mode operation cannot harness the advantages of recently emerging high-bandwidth positioning systems, which provide bandwidths in the order of 10% – 20% of the cantilever resonant frequencies [8, 9, 10]. These recent advances in lateral positioning bandwidths necessitate the need for imaging techniques that can robustly measure sample characteristics at imaging speeds that are a substantial fraction of the probe resonance frequency.

One of the primary objective of this dissertation is to emphasize the potential of system theoretic tools to exploit bandwidth enhancements reported in nanopositioning devices. This reliance on the modern control techniques alleviates the need for specialized fabrication.

## 1.2 High-Speed AFM: State-of-the-Art

### 1.2.1 Cantilevers

It has been established that amplitude modulation will lead to erroneous topography estimates when the time-scale separation between cantilever oscillation frequency and lateral positioning frequency is not sufficiently large. Increasing the resonance frequency of cantilevers corresponding to increase in positioning bandwidths helps maintain the necessary time-scale separation between the two frequencies and provides higher speed scans [11]. However, enhancing the frequency of cantilevers comes at the cost of added cantilever stiffness. The limit on balancing these two properties is believed to be reached by Olympus (a commercial cantilever manufacturer) with a cantilever resonance of 1.2 MHz in liquids (water), stiffness of  $0.15 - 0.20$  N/m and quality factor of  $\approx 2$  [12, 13]. Similar small cantilevers for higher imaging speeds are also available from Asylum Research [13]. Cantilevers integrated with actuators and sensors for fast scanning and lithography are employed in [14].

Furthermore, the use of small cantilevers calls for modifications in sensing structure. In [15] an objective lens type detector that focuses a laser spot on small cantilevers and also collects the beam reflected off of the cantilever is deployed. An analog circuit that uses the peak-peak deflection voltage is used for amplitude computation instead of the conventional lock-in amplifier [15].

### 1.2.2 Positioners

The need to study temporal biological events over long scan ranges gives rise to the need for compact desktop-size nanopositioning systems, which can provide motion range in the order of few millimeters and yet achieve resolution in nanometers. Positioning speeds of the order of  $10 - 20\%$  of typical tapping mode cantilever frequencies have been achieved through MEMS designs [8, 9, 10]. On the other hand, commercial AFM systems have positioners that operate at  $0.5 - 3\%$  of the cantilever resonance frequencies.

In [16] both the lateral positioners ( $x$  and  $y$ ) and the vertical positioner ( $z$ ) are modified to have high bandwidths (60 kHz in  $z$  direction being the maximum). However, improvements

in bandwidth of nanopositioners are often achieved through reduction in their size [16]. The range of the  $x$  and  $y$  scanners are limited to  $1 - 4 \mu\text{m}$  and that of the  $z$  positioner to  $1 \mu\text{m}$ . As a consequence, smaller scan sizes of  $200 \text{ nm}$  and  $100$  scan lines are illustrated in [16].

Hansma's group developed relatively larger range scanners of up to  $15 \mu\text{m}$  in  $x$  and  $y$  directions, and  $6 \mu\text{m}$  in the  $z$  direction [8]. High-speed data acquisition systems were also demonstrated to realize high closed-loop bandwidths. In [17] ultra-high speed scans of collagen fibers at room temperature are reported using tuning forks scanners ( $30 - 100 \text{ kHz}$  bandwidths), but the scans are performed in the contact or constant force mode.

### 1.2.3 Role of Controls

*Cantilevers:* Cantilever arrays were used in the IBM Millipede program [18] to create a topographic high-density data storage technology that forms and detects indentations thermally. Modern control techniques were used for positioning in probe-based manufacturing as well as storage operation. This technology was a successful effort toward high throughput with nanoscale manipulation abilities. Significant and fast progress in fields like flash storage made this technology commercially nonviable.

*Positioners:* As seen in Sections 1.2.1 and 1.2.2 high-speed imaging in AFM is predominantly effected through specialized fabrication and modifications to the hardware, rather than using system theoretic tools. Use of modern control system concepts in nanopositioning systems to design simultaneously for resolution, bandwidth, and robustness requirements have been explored by the authors of [6, 19]. The authors have quantified the trade-offs between these performance objectives and shown notable increase in bandwidths in nanopositioning preserving the necessary resolution and robustness margins.

*Imaging:* Commercial AFMs typically use PID control designs for force regulation that do not utilize the dynamics of the system's underlying model since they are not model-based. In [15, 16] a dynamic PID approach is applied to keep the tip-sample interaction forces small. However, this too is not a model-based controller. Moreover, [15] and [16] rely on amplitude modulation, using the root-mean-square deflection voltage values for amplitude computation, which could result in spurious imaging at high speeds.

Use of model-based  $\mathcal{H}_\infty$  control combined with feedforward control for imaging has been reported to have better performance over traditional PID in [20]. Control tools have been employed to separate the signals used for force regulation and sample topography estimation in [21, 22], facilitating high-bandwidth sample profile estimation.

In [23, 24] observer-based techniques are applied to sample detection at high speeds and in [25] similar techniques combined with active  $Q$  control have been used to image samples with small features. However, since the observer-based methods do not have force regulation, these are unable to measure large changes in the sample topography.

### 1.3 Scope of Thesis

With the discussion so far, it has been established that advances in MEMS has notably increased nanopositioning speeds. Amplitude modulation, which is currently the most preferred mode of high-resolution imaging in AFM is not considered reliable to measure sample topography when the lateral positioning bandwidths are in the order of 15% – 20% of the cantilever resonance frequencies. This motivates the scope of this dissertation, which is to develop a novel dynamic mode of operation that enables high-bandwidth imaging in AFM and subsequent property estimation.

The amplitude signal derived from the deflection signal using the demodulation-system in AM-AFM is slow and served as an apt output to base feedback design on. However, as explained in Section 1.1.1.3 AM-AFM is unsuitable with the advent of high-speed lateral positioning since amplitude being virtually constant over an oscillation period of cantilever is no longer true. Further, this mode introduces complexities through lock-in circuits that are nonlinear and make model-based designs very cumbersome. This thesis proposes **regulating** the tip-sample interaction **force** by **feeding back** directly the cantilever **deflection** signal itself. The deflection signal is as **fast** as its resonance frequency in dynamic operation but Field Programmable Gate Array (FPGA)-based electronics provide means for closed-loop operating bandwidths in the order of a few Mhz. Recently, alternate hardware technologies (Field Programmable Analog Arrays) have also been shown to work successfully with signals of  $\approx 100$  kHz frequency while implementing  $\mathcal{H}_\infty$  controller [26].

The application of controls with respect to the AFM community is often restricted to simple PID controllers for force regulation. Force regulation in this work uses tools from robust and optimal control to design a **model-based controller**. System requirements such as regulation, robustness and noise attenuation can be distinctly quantified and designed for under the framework used. Furthermore, the control design exploits the underlying model of AFM imaging system to make the deflection signal track a suitably designed reference signal. This takes care of tip-sample interaction force regulation. Moreover, the **nonlinearities** induced by the interaction forces are **formulated as disturbance** in the proposed model making it possible to use linear control methods.

Real-time **sample topography** as well as **property estimation** are part of the thesis scope. A signal different from the force regulating signal is designed to estimate the disturbance in the model, which captures the tip-sample interactions. The merits of estimating interaction forces directly and consequently deducing sample properties from these force estimates are presented using example procedures. Performance characteristics and advantages of the proposed novel imaging mode are illustrated through simulations and preliminary experiments are used to validate proof of concept.

A notable feature of the proposed imaging mode is that it uses the control and the error signals (however large or small) to estimate sample properties and is therefore robust even to the regulation performance. In this case, regulation is required only to ensure that the tip does not entirely deviate from its behavior, for instance parachute off or crash into the sample surface.

## 1.4 Structure of Thesis

The dissertation organization is as follows. In Chapter 2 the operating principle of AFMs is presented complete with key component descriptions, and existing modes of operation. The second half of this chapter, from Section 2.4 demonstrates the systems perspective for AFM imaging framework. The new dynamic mode for high-bandwidth imaging is introduced in Chapter 3 using systems perspective from Chapter 2 as basis. A model-based control design is fundamental to developing the new imaging mode. Therefore, complete model

descriptions and optimal control framework details are explained in Chapter 3. The solution to the disturbance rejection problem through linear-matrix-inequalities (LMI) is also shown. Furthermore, performance of the designed controller is demonstrated through simulation results. Chapter 4 focuses on developing and verifying estimation methods for tip-sample forces, and consequent estimation of sample topographical and physical properties. The experimental set up, issues involved and results used for validation are given in Chapter 5. Finally, Chapter 6 summarizes the contribution and salient features of the dissertation. Also, future research considerations are briefed.



## CHAPTER 2

# IMAGING FRAMEWORK AND SYSTEMS VIEWPOINT

It is important to understand the working principle of the AFM and the existing modes of imaging in order to put high-bandwidth dynamic imaging in context. Towards this goal, the fundamental components critical for imaging in AFM are explained in Section 2.1. Suitable modeling of the micro-cantilever probe dynamics and its interactions with the sample are addressed in Section 2.2. Furthermore, a broad classification of existing scanning methods and their operational techniques are outlined in Section 2.3. Readers familiar with atomic force microscopy may skip to Section 2.4 that details the systems perspective of imaging in AFM used in this work. In this dissertation a model-based control design that can be used to incorporate a high-resolution, high-bandwidth dynamic mode of scanning is sought. This is achieved by taking a control systems perspective on imaging as shown in Section 2.4.1. In particular, the systems model for dynamic mode of imaging is discussed. The systems setup allows formulation of control objectives with respect to resolution, robustness to uncertainties and bandwidth, followed by designing of control. Following this, the basic control system formulation considered for our research problem is presented in Section 2.6

### 2.1 AFM Operation

A schematic of the components fundamental to AFM operation is shown in Figure 2.1. The key components include the micro-cantilever or the scanning probe, the sensing mechanism setup, and the lateral and vertical actuators.

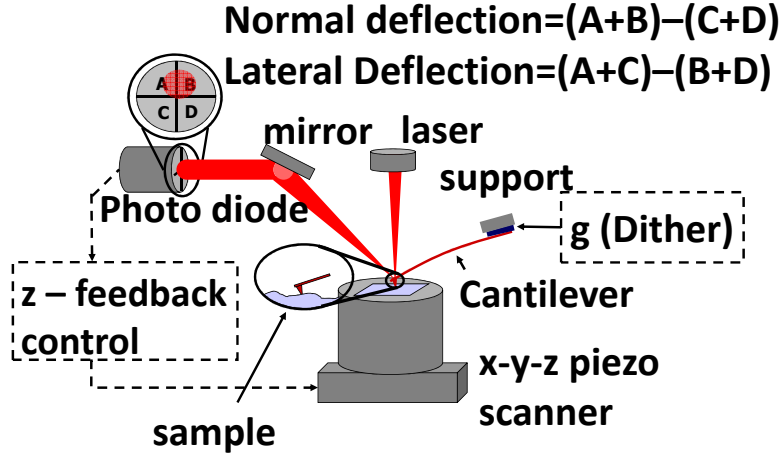


Figure 2.1: Schematic of AFM showing all the fundamental components. In the pictured configuration, both vertical and lateral piezos are located in the base or scanning stage.

### 2.1.1 Probe and Sensing

The ability of the micro-cantilever, used in an AFM, to sense small forces, in the order of pico-Newtons, forms the fundamental of its operation. The sharp tip on the cantilever senses inter-atomic forces when the tip is close to the sample. These forces lie in the range of  $10^{-7}$  -  $10^{-12}$  N. The AFM therefore enables measurement of atomic-scale Van der Waals forces, electrostatic forces, capillary forces and friction forces. The stiffness of the cantilevers are anywhere between 0.06 - 100 N/m. The cantilever are typically made of silicon, silicon nitride or silicon oxide and their lengths are between 100 - 500  $\mu\text{m}$ . The AFM cantilevers have resonance frequencies higher than 2 kHz making them insensitive to common external disturbances that are within this range.

The tip-sample interaction forces are a function of the tip-sample distance and therefore vary over a raster scan of the sample. This change in interaction forces results in a corresponding change of cantilever deflection. The sensing mechanism comprises of a laser beam incident on the cantilever and reflected onto a split photo-sensitive diode (PSD). Deflection of the cantilever owing to tip-sample interactions results in change of laser incidence angle,

which is captured by change in location of the laser spot on the PSD.

### 2.1.2 Controller

In closed-loop operation, the measured cantilever deflection or its derivative signal such as the amplitude or phase is used as the feedback controller input. The signal chosen for feedback depends on the mode of scanning. The controller regulates the measured cantilever characteristic to a reference value in order to maintain constant forcing on the sample. This is achieved by driving the  $z$  or the vertical piezo-actuator with the generated control signal. The vertical motion aims to keep the tip-sample distance constant, thereby regulating the interaction forces. As a consequence, the control signal also acts as a measure of the sample height features. Most commercial AFMs use PI (proportional-integral) or PII (proportional-double integral) control by default. These controllers are not model-based. The implementation is carried out by digital components such as DSPs and FPGAs.

### 2.1.3 Piezo-Actuators

**Dither Piezo:** The base of the cantilever is attached to a dither piezo also called as the shake piezo. During dynamic scans, the dither piezo is used to oscillate the cantilever sinusoidally. This piezo typically has very high bandwidths in the order of 600 kHz to accommodate similar orders of cantilever resonance frequencies.

**Lateral Piezo:** The sample to be scanned is mounted on a piezoelectric scanner that provides lateral movement (denoted as  $x$  and  $y$  directions). This assembly is called as the AFM's scanning stage. The lateral stage can accommodate scan sizes of up to 90  $\mu\text{m}$  at zero degree scan angle. The bandwidths are in the order of a few hundred Hz after which nonlinearities such as hysteresis and creep affect the performance. However, it has been shown that robust 2DOF control designs can significantly increase the scanner bandwidths [6].

**Vertical Piezo:** An additional piezo actuator termed the  $z$ -piezo provides vertical movement. There are two common configurations of the AFM, depending on the location of the  $z$  or vertical piezo. In the MFP-3D AFM from Asylum Research used in this work, the

$z$ -piezo-actuator is located along with the cantilever and the laser optic arrangement, in a unit called the AFM's head. As a result, the  $z$ -piezo actuation causes vertical movement of the cantilever along with its base. In the alternate configuration, the  $z$ -piezo effects vertical movement of the scanning stage and therefore the sample. Typical travel for the  $z$  piezo is around 15  $\mu\text{m}$ . Compatible extended heads with travel up to 40  $\mu\text{m}$  are available from the company.

## 2.2 Model for Imaging

The use of model-free controllers such as PI and PII in commercial AFMs fails to tap the underlying dynamics of the system. Throughout this work, all control designs are model-based. This necessitates deriving a good model for the cantilever subsystem during imaging operation. Modeling the probe as a damped harmonic oscillator with external forcing, is widely accepted in AFM literature. In general, the external forces acting on the cantilever include oscillations from the dither piezo based on the mode of operation, and the tip-sample interaction forces. Modeling considerations for the tip-sample interaction forces are detailed in Section 2.2.2

### 2.2.1 Cantilever Model

The first natural frequency dynamics of the cantilever is modeled by a spring-mass-damper system given by,

$$\begin{aligned}\frac{d^2\bar{z}}{dt^2} + \frac{\omega_n}{Q} \frac{d\bar{z}}{dt} + \omega_n^2 &= F(t), \\ \bar{y} &= \bar{z} + n.\end{aligned}\tag{2.1}$$

In (2.1), the signals  $\bar{z}$  and  $\bar{y}$  are the cantilever deflection and the measured cantilever deflection with measurement noise  $n$ . The forces on the cantilever are indicated by  $F$ . The parameters  $\omega_n$  and  $Q$  are the first natural frequency and quality factor of the cantilever. The quality factor characterizes the energy loss of the cantilever to the surrounding environment. The resonance frequencies of cantilevers typically used in AFM are in the range of 10 – 400 kHz. The value of  $Q$  could be as low as 2 under liquids to about 10,000 under

vacuum. The measurement noise  $n$  is dominated by  $1/f$  noise at low frequencies and is nearly white at frequencies beyond a few kilohertz. The modeling of the cantilever as shown in (2.1) facilitates the application of control system perspective to the imaging framework (details in Chapter 2.4).

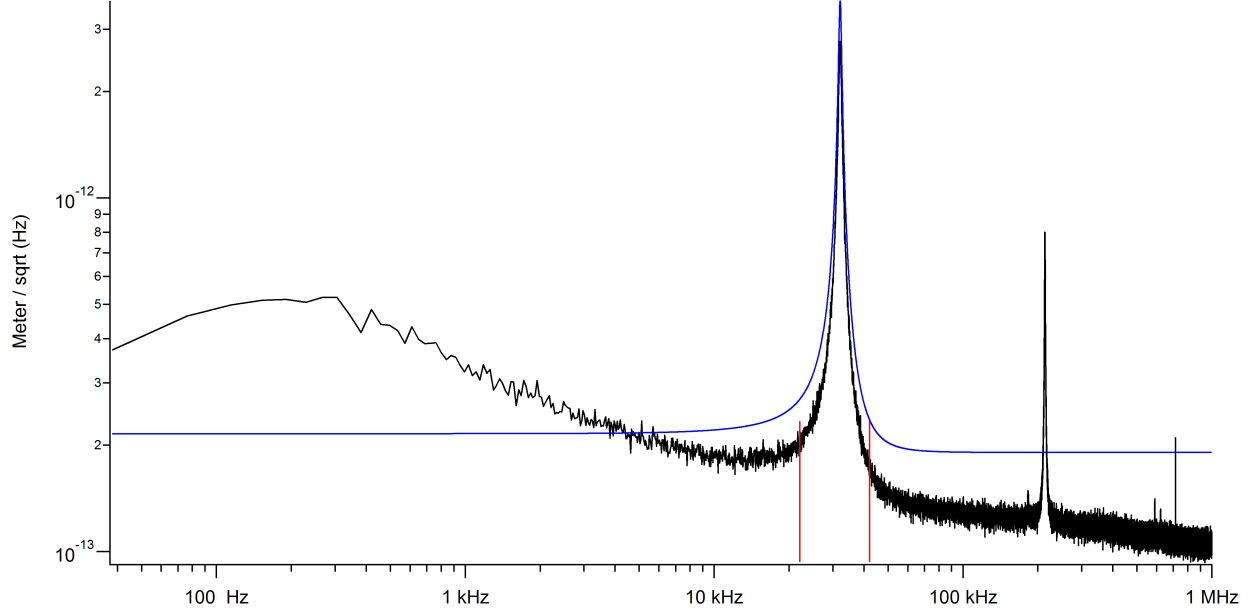


Figure 2.2: Thermal response shows  $1/f$  noise is dominant at low frequencies and thermal noise dominant over measurement noise at resonance frequencies. Blue line shows second order transfer function fit to the cantilever's first modal frequency. The red lines mark the frequency region around resonance chosen for the fit

### 2.2.1.1 Thermal Noise

At thermal equilibrium, the transfer function from the thermal noise  $\eta$  to the cantilever deflection  $p_1$  is given by,

$$G_{therm}(s) = \frac{1}{s^2 + \frac{\omega_n}{Q}s + \omega_n^2} \quad (2.2)$$

where  $\omega_n$  is the resonance frequency of the cantilever and  $Q$  denotes the quality factor. At lower frequencies, close to dc the  $1/f$  noise is predominant. However, at the resonance frequency, the thermal response of the cantilever is dominant over response due to measurement noises. This implies that near the resonance frequency the cantilever is only limited by its

thermal noise characteristics. At any given temperature, thermally restricted resolution is the best that a sensor can achieve. Consequently, the AFM cantilever exhibits very high-resolution sensing properties. In Figure 2.2 it can be seen that at the first natural frequency of the cantilever shown ( $\approx 30$  kHz), a clear second order fit (blue line) can be obtained. This along with static forcing curves may be used to determine the cantilever stiffness and quality factor. A primary candidate of the forces acting on the cantilever is the tip-sample interaction force.

### 2.2.2 Tip-Sample Interaction Models

Typically, when the probe-sample separation is large the probe does not experience any short range forces and therefore there is no deflection detected. However, when the tip gets closer to the sample, the short range Van Der Waal forces act first as an attractive force that pulls the cantilever towards the sample surface. This may cause the cantilever to jump to contact. As the separation distance decreases further, and the tip and sample come in contact elastic forces start acting. In the middle range, attraction forces act between some of the probe-sample molecule pairs (potential is proportional to  $\frac{-1}{r^6}$ ) and repulsive forces act between some other pairs (potential is proportional to  $\frac{1}{r^{12}}$ ). AFM in the dynamic mode of operation (discussed in Section 2.3.2) stays in this intermittent region, shown in Figure 2.3). The tip-sample interaction forces are the most fundamental quantities that the probe tip can detect. For instance, while scanning a compliant sample, although the probe is sensitive to any short range force coming from the sample, at a given location it cannot distinguish between the forces occurring due to sample features and those occurring due to the compliance of the sample. This division is completely determined by the physical model assumed for the tip-sample interaction forces.

The classical Hertz contact model accounts for elastic deformation of bodies under imposed loads during **contact**, however, it ignores forces of adhesion which act during intermittent contact. The later force models in literature [27, 28, 29] have developed upon Hertz model by including adhesive forces and/or Van Der Waals forces. Such models are used extensively in AFM applications to model the tip-sample interaction force. More details and equations

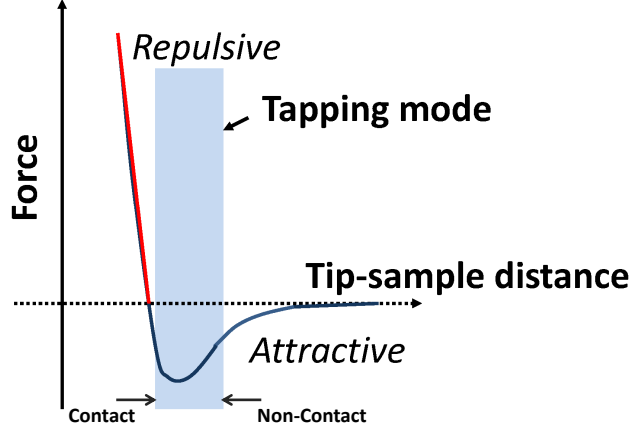


Figure 2.3: Force Vs tip-sample separation showing attractive and repulsive region. Modes of imaging in an AFM can also be characterized by the force region that the tip-sample interactions occur at.

that the physical force models represent are presented in Chapter 4.

Based on the nature of the probe tip and sample, appropriate models are chosen. The Derjaguin-Muller-Toropov model [28, 4] is applied to tips with small curvature radius and high stiffness. It is assumed that deformed surfaces geometry does not differ much from that given by the Hertz problem solution. The DMT model considers Van der Waals forces in the perimeter of the contact area. Johnson-Kendall-Roberts model [27] is applied when the tip has large curvature radius and small stiffness. The model accounts for the influence of Van der Waals forces within the contact zone. The Maugis model [29] could be applied to low as well as high adhesion systems. The model includes a weighting parameter that determines the amount of adhesion.

**Force curves** represent the relation between the cantilever deflection and tip-sample separation, or in real experiments the photo-diode voltage and tip-sample separation while forcing at a particular location. Every time a new cantilever is mounted a static force curve is used to obtain the variable called “*optical lever sensitivity*” that defines the relationship between cantilever deflection and corresponding voltage change in the PSD. A typical force curve from experiments is shown in Figure 2.4.

In the imaging mode proposed in Chapter 3 the DMT model is used for reference trajectory design (see Section 3.2. However, it must be noted that the mode design does not require a force model as long as the reference trajectory ensures that the tip stays on the sample

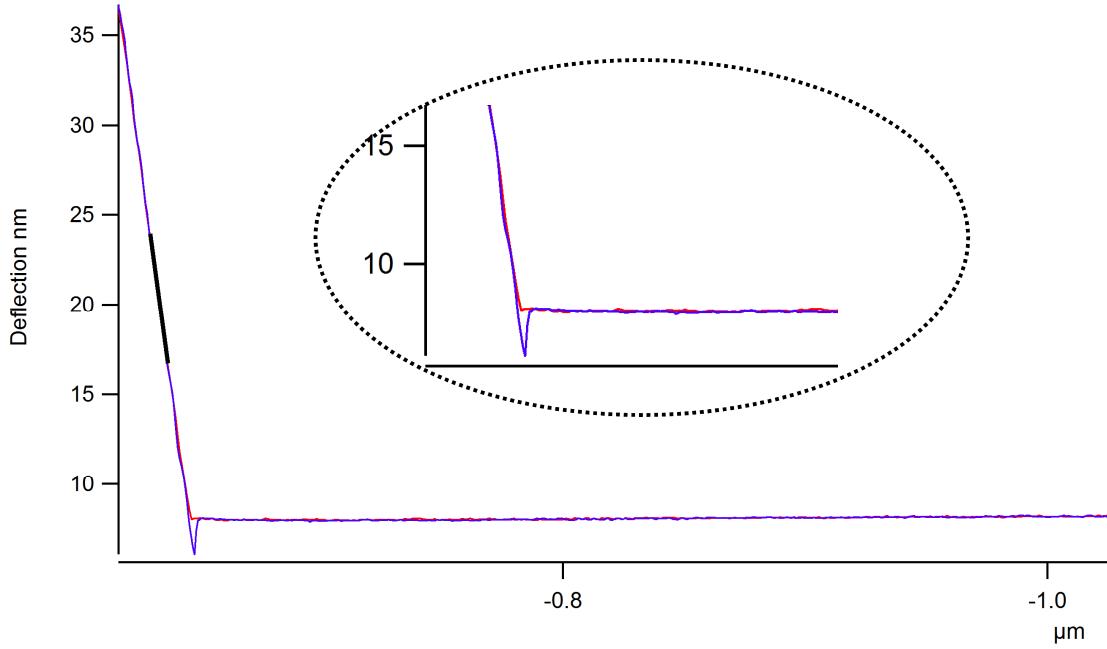


Figure 2.4: Typical force curve obtained in contact mode using a SiNi probe under water, the slope of the repulsive force region is used to determine optical lever sensitivity (in nm/V) for given cantilever. For this particular tip and sample the force curve can be well approximated by the DMT model.

surface.

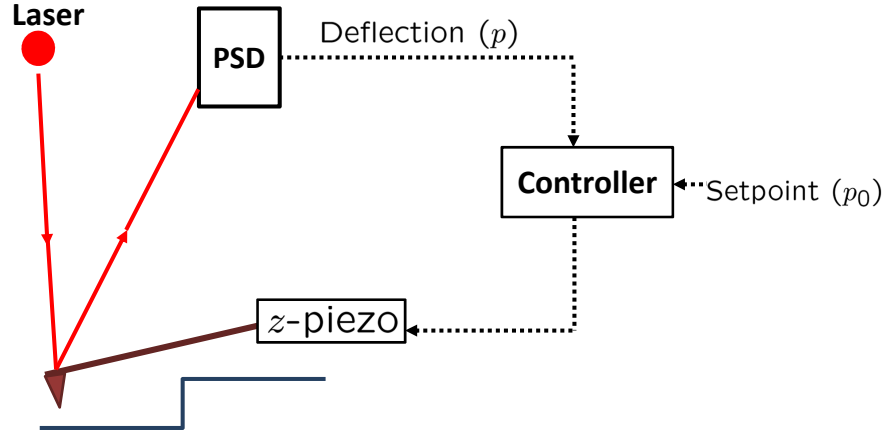
## 2.3 Modes of Scanning

The process of imaging in an AFM can be broadly classified into static and dynamic modes of imaging based on the presence or absence of forced excitation of the cantilever using the shake piezo-actuator. Dynamic mode of imaging is of particular interest for our work owing to its advantages discussed in this section.

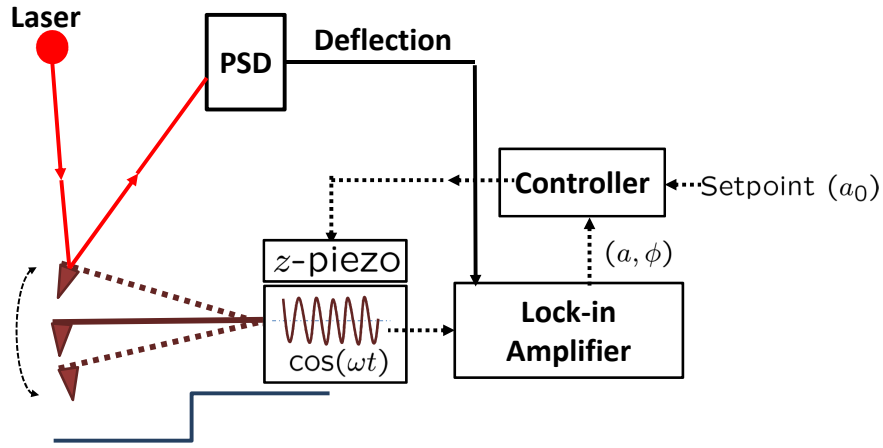
### 2.3.1 Static or Contact Mode Scanning

In the static or contact mode of operation, the cantilever is not oscillated by the dither piezo-actuator. The most common static mode of operation involves maintaining a constant force between the cantilever tip and the sample by maintaining a constant cantilever deflection (see Figure 2.5(a)). The scanning characteristics in the static mode are not confined to a





(a)



(b)

Figure 2.5: (a) Schematic of **constant force** (static) mode of scanning, the deflection signal is regulated to a set point to maintain constant tip-sample force. (b) Schematic of **tapping mode** or amplitude modulated (dynamic) mode of scanning, the lock-in amplifier computes the amplitude of oscillation that is regulated to a set point.

specific frequency. Therefore, the deflection of the cantilever due to its interaction with the sample should be large enough to overcome the measurement noise. However, it may be noted that the inter-atomic forces from the sample surface are small. Hence the stiffness of cantilevers used in static mode should be small to allow for larger deflections. In most cases, the forcing in static mode operation lies in the repulsive force region where the force values are higher.

During constant force scans, a feedback controller acts on the PSD voltage and actuates the  $z$ -piezo-actuator to regulate the voltage to a constant set point value as illustrated in Figure 2.5(a). This kind of regulation ensures a constant tip-sample distance which results in constant cantilever deflection. The feedback control signal for  $z$  is used as a measure of the sample profile.

#### 2.3.1.1 Pros and Cons

- **Ease of implementation:** Static mode implementation is simple since the tip-deflection measured by the PSD is directly used as the feedback input signal. No additional dynamics are involved.
- *Not suitable for soft samples:* The tip is constantly “*in contact*” with the sample, which causes it to drag laterally on the sample surface. Furthermore, the large forces required to get reliable deflection measurements have high potential of damaging soft sample surfaces.

### 2.3.2 Dynamic Mode Scanning

In the dynamic mode of scanning, the cantilever is sinusoidally actuated often at a frequency  $\omega$  close to its natural frequency. From the thermal noise characteristics, it is evident that the cantilever has very high resolution in the region around its resonance frequency. The interaction of the cantilever tip with the sample surface is modeled as a shift in the resonance frequency  $\omega_n$  of the cantilever (see Figure 2.6) arising from a change in the effective spring

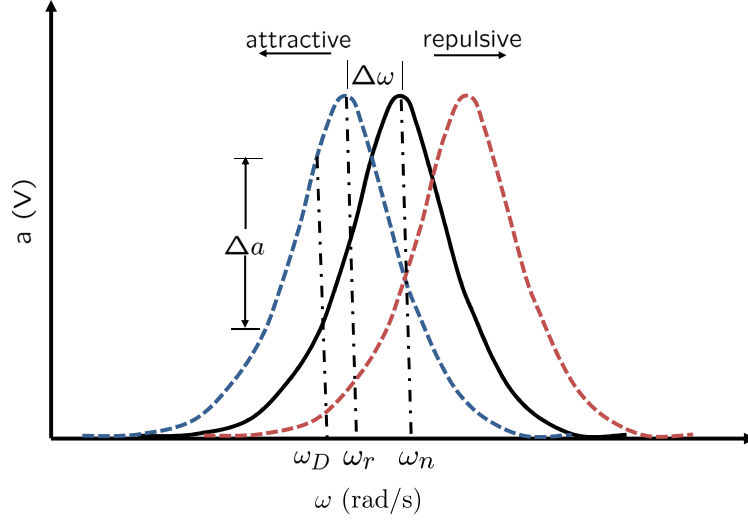


Figure 2.6: Frequency vs Amplitude curves: interaction with sample in the dynamic mode is modeled by a shift in resonance frequency and a corresponding change in oscillation amplitude.

constant of the cantilever. This can be explained as follows,

$$\begin{aligned}
 k_{eff} &= k - \frac{\partial F_{ts}}{\partial z_{ts}}, \text{ and,} \\
 \omega_r^2 &= \frac{k_{eff}}{m} \\
 \Rightarrow f &= \frac{1}{2\pi} \sqrt{\frac{k - \frac{\partial F_{ts}}{\partial z_{ts}}}{m}},
 \end{aligned} \tag{2.3}$$

where,  $m$  is the cantilever mass,  $f$  is the shifted first natural frequency in Hz, and  $k_{eff}$  denotes the effective spring constant of the cantilever when it is close to the sample. The tip-sample separation and the force are denoted by  $z_{ts}$  and  $F_{ts}$  respectively. The shifted frequency is shown as  $\omega_r$ . In the repulsive force region, the equivalent resonance frequency shifts towards lower frequency ( $\omega_r$ ) since  $\frac{\partial F_{ts}}{\partial z_{ts}} < 0$ . Correspondingly, effective resonance shifts to higher frequency values in the attractive zone.

The change in amplitude ( $\Delta a$ ) while scanning over a sample is attributed to this frequency shift, which makes the amplitude follow a new shifted curve at the frequency of oscillation (Figure 2.6). The drive frequency or the frequency at which the dither signal operates is typically taken to be  $-5\%$  of the first resonance frequency. This is done to observe significant  $\Delta a$  values as seen in Figure 2.6.

There exist two common techniques under dynamic scanning, **amplitude modulation** and **frequency modulation**. In **amplitude modulated AFM**, the change in amplitude of cantilever due to sample interaction is exploited. The deflection of the cantilever is passed through a lock-in amplifier to obtain the amplitude  $a$  and phase  $\phi$  of its oscillation. The controller regulates the amplitude signal to a constant value by moving the  $z$ -piezo-actuator and this control signal also serves as a measure of the sample topography (see Figure 2.5(b) for a schematic). Typical amplitude values range from 50 - 200 nm for cantilevers with stiffness between 2 - 50 N/m. The signal to noise ratio (SNR) is better than in contact mode operation since the imaging is done near the cantilever resonance frequency. The SNR can be improved further with cantilevers having higher quality factor  $Q$  values. This mode of operation can be used to measure larger features on the sample surface ( $\approx 200$  nm) reliably. Furthermore, the cantilever is only intermittently in contact (once every oscillation cycle) with the sample surface causing minimal or no damage. Also, unlike in contact mode scanning shear and drag forces are not present in this mode of imaging. The forcing in amplitude modulation applications is often modeled by the DMT model (Section 2.2.2).

In **frequency modulation AFM**, the cantilever is oscillated at the equivalent resonance frequency. The controller regulates the frequency shift ( $\Delta\omega$ ) to a set point frequency shift value  $\Delta\omega_0$  by altering the vertical position of the cantilever or sample. This mode of scanning is best suited for measuring small features and is usually operated under vacuum due to high quality factor ( $Q$ ) requirements.

#### 2.3.2.1 Pros and Cons

The focus is on AM-AFM or tapping mode AFM.

- **High resolution:** The resolution of sensing by the cantilever-tip is only limited by the thermal noise in the frequency range of operation.
- **Suitable for soft bio-samples:** The tip is only intermittently in contact with the sample, i.e. once every cycle of oscillation for a very small fraction of the time period. Tapping mode functions robustly under fluids, which is important when dealing with biological samples.

The forcing on the sample can be made mild by choosing the amplitude set point appropriately. An amplitude set point close to the free air amplitude of oscillation of the cantilever implies soft engagement onto the sample surface.

- *Additional nonlinear dynamics:* The lock-in amplifier used to derive the amplitude and phase of cantilever oscillation from its deflection signal introduces nonlinearities in the loop.

Thus far the imaging process in AFM and the frameworks conventionally used have been elucidated. It remains to apply a systems viewpoint to the imaging framework. This is necessary in order to formulate the scope of this work in the form of control objectives or problem. Once the control-based problem is established, a suitable design to achieve these objectives will be sought through modern control tools.

## 2.4 Control System Perspective for Imaging

The needs and challenges listed in Chapter 1 will be addressed while viewing the AFM imaging process as a feedback control system. Feedback control was present in AFMs right from their conception.

### 2.4.1 AFM Imaging from Systems Viewpoint

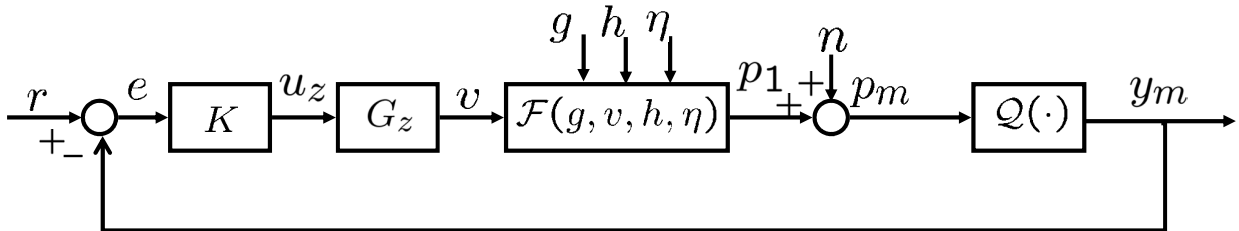


Figure 2.7: Feedback framework for imaging. In the **contact** or **constant force mode**,  $g = 0$  and  $Q = I$  (identity). The cantilever deflection is fed back to the controller. In **tapping mode** operation,  $g$  is a sinusoidal signal and  $Q$  comprises of the demodulation circuit that generates  $a$ , the amplitude and  $\phi$ , the phase of cantilever oscillation.

In Figure 2.7,  $\mathcal{F}$  denotes the tip-sample dynamic model. This is an aggregate of the cantilever dynamics as well its interactions with the sample surface. The tip-sample dynamic models depends on the dither actuation signal  $g$ , the sample topography  $h$ , the vertical actuation  $v$  through the  $z$ -piezo and the thermal noise  $\eta$ . It also depends on  $p_1$ , the cantilever deflection. The measured deflection  $p_m$  is the sum of  $p_1$  and the measurement noise in PSD  $n$ .

The dynamic block  $\mathcal{Q}$  is taken to be  $I$  when deflection is the feedback parameter, for instance contact mode. In other cases when the feedback parameter is a derivative of the cantilever deflection,  $\mathcal{Q}$  is defined appropriately such that  $y_m$  in Figure 2.7 is the intended signal, for instance amplitude or phase. Subsequently, the measured output signal  $y_m$ , which is either the measured cantilever deflection or a desired derivative of it is regulated to the reference signal value given by  $r$  in Figure 2.7. The controller  $K$  acts upon the error signal  $e$  between the output and reference signals to generate the control input  $u_z$  that drives the vertical piezo. The vertical piezo transfer function is represented by the dynamic block  $G_z$ . Sine sweep identification is performed from the input of  $G_z$ ,  $u_z$  to its output  $v$  to obtain the transfer function of  $G_z$ . The transfer function of  $G_z$  is approximately a constant at low frequencies and hence the control signal  $G_z u_z$  is used as a measure of the sample topography.

### 2.4.2 Systems Viewpoint for Tapping Mode Dynamic AFM

In the dynamic mode of operation, the dither signal is a sinusoidal signal of the form,  $g_0 \cos \omega t$  where  $g_0$  defines the amplitude of oscillation, and  $\omega$  is chosen close to the first modal frequency of the cantilever for best sensitivity. Phase or, more commonly, the amplitude of cantilever oscillation is fed back to the controller. The cantilever deflection in dynamic mode of operation, is in the order of 100 – 300 kHz. The scanning bandwidth and controller operation bandwidths are several orders lower at 0.3 – 3 kHz. Amplitude regulation in current AFMs yields good results since the lateral positioning bandwidths are only about one percent of the resonant frequencies of cantilevers. The cantilever typically oscillates over many cycles before it experiences appreciable change in sample topography. Therefore, the amplitude, and equivalently the amplitude-regulating control effort provides a reliable

measure of the sample topography. However, when the lateral positioning bandwidths are higher, there is appreciable change in the topography even within one or few oscillation cycles. In view of recent advances in positioning system designs that facilitate bandwidths in the order of 10–15% (up to  $\approx 30$  kHz) of the cantilever resonance frequencies, the tapping mode is not a reliable way of sample topography measurement. Furthermore, the vertical position of the cantilever  $v$ , which is equal to  $G_z u_z$  is used as a sample topography measure. This is validated by the fact that  $v$  compensates for the sample height effects to maintain a constant amplitude signal in tapping mode operation. At high frequencies,  $G_z$  is no more a constant and this measure therefore does not hold for high speed scans.

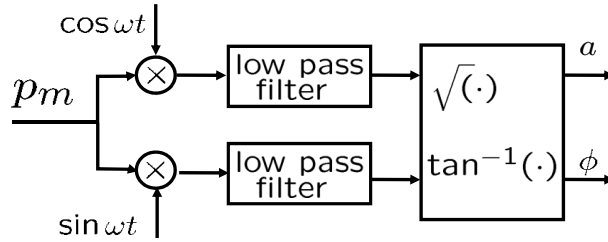


Figure 2.8: Demodulation circuit used in tapping mode AFM operation

The demodulation circuit used to compute the amplitude of oscillation  $a$  from the measured cantilever deflection is shown in Figure 2.8. The measured deflection can be modeled to be of the form  $a(t) \cos(\omega t + \phi)$ , where  $a(t)$  is very slowly varying. The demodulation operation used induces nonlinearities to the closed-loop (multiplications of  $\sin \omega t$  and  $\cos \omega t$ ) as shown in Figure 2.8. In addition, the computation of amplitude signal through this digital circuit takes a few cycles of cantilever oscillation.

## 2.5 Cantilever Subsystem and Tip-sample Model

The tip-sample dynamic model can be viewed as an interconnection between a linear function  $G_c$  and a static non-linearity given by  $F_{ts}$ .  $G_c$  represents the cantilever model where  $p_1$  is the cantilever deflection. The cantilever model (stiffness, quality factor and optical lever sensitivity) is typically got from the unforced thermal response of the cantilever. The different modes of imaging in AFM are characterized by their designs of the dither control

input  $g$  and the vertical-positioning piezoactuator input  $u_z$ , and the way they interpret the sample feature height  $h$  from the deflection measurements  $p_m$ .

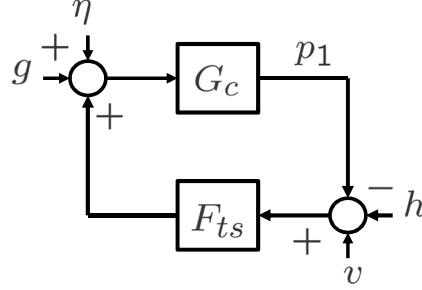


Figure 2.9: Cantilever transfer function  $G_c$  in feedback loop with tip-sample interaction force  $F_{ts}$ . This viewpoint isolates nonlinear force potential  $F_{ts}$  from the cantilever model. This function is typically bounded for the operating range of tip-sample separations.

In the AFM setup (Mfp3D from Asylum Research) used in our lab, the cantilever along with the cantilever holder and sensing tools, including the PSD, are moved in the vertical direction to compensate for sample inputs. Under dynamic mode of operation in this setup, forcing on the cantilever includes the sinusoidal dither actuation  $g$ , the thermal noise  $\eta$  and the tip-sample inter-atomic forces given by  $F(p_1 - h + v)$ . The inter-atomic force is a function of the cantilever deflection, the vertical actuation  $v$  and the sample input  $h$ . The separation between the tip and the sample is given by  $(p_1 - h + v)$  in Mfp3D AFM configuration. The interaction force is also a nonlinear function of the physical properties of the cantilever and sample.

The nonlinear interaction forces are bounded for a fixed range of tip-sample separation distance. The representation of the tip-sample dynamic model as a linear function interconnected with a static non-linearity (called as Lurè system in systems literature), when the non-linearity is bounded, is very useful for model-based control design and analysis.

## 2.6 Proposed Control System Setup for High-speed Scanning

The model for cantilever dynamics in Section 2.5 is used as a basis to model the new imaging mode. The cantilever transfer function is viewed to be interacting with the tip-sample forcing  $F_{ts}$ . Since we propose to directly use the cantilever deflection signal  $y$  for feedback, the



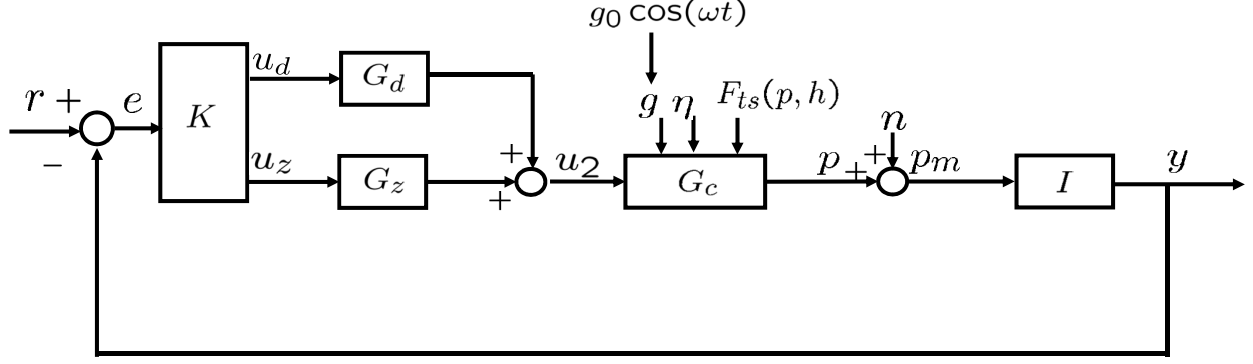


Figure 2.10: Systems representation for the proposed new dynamic mode of imaging in AFM. A tracking problem where the cantilever deflection is made to follow a reference  $r$  is formulated.

dynamics of  $\mathcal{Q}$  is replaced by identity.  $n$  denotes the measurement noise present in the system arising from the detection electronics.

The signal  $r$  in Figure 2.10 represents the reference trajectory that the cantilever deflection is required to track in order to maintain the forces between the tip and sample constant. The forcing on  $G_c$  from the nonlinear interaction forces is modeled in our imaging mode to be a extraneous disturbance signal. The feedback controller  $K$  is then designed for disturbance rejection amongst other objectives of noise attenuation and robustness.

The control signal is denoted by  $u_2$  which may be made to act on the cantilever through the shake piezo as a signal  $G_d u_d$  in addition the sinusoidal actuation  $g_0 \cos \omega t$ . At times the low frequency component of the control signal  $u_2$  may be directed through the  $z$  piezo in the form of  $u_z$ . The  $z$  piezo transfer function is represented by  $G_z$  in Figure 2.10.

## 2.7 Summary

In summary, the first part of this chapter presented basics of operation and imaging in AFM. The significance of the key components and common modes of imaging were analyzed. It was concluded that the tapping mode or dynamic mode of operation is best suited for high-resolution applications. Further the AFM imaging framework, and in particular dynamic imaging, was fit into a systems perspective. With this understanding the control-systems framework for the new dynamic imaging mode that is central to the dissertation was intro-

duced. The details of this imaging technique will be presented in the following chapter.

## CHAPTER 3

### HIGH-BANDWIDTH IMAGING MODE

The high-bandwidth imaging mode proposed is effected by a model-based control design that makes the cantilever deflection signal track a suitably designed trajectory in the dynamic mode of operation. The reference trajectory design satisfies force regulation requirements and ensures that the cantilever does not crash into or get completely detached from the sample surface. The salient features of this mode of imaging are:

- It preserves the high resolution and soft forcing properties present in prevalent dynamic modes of operation.
- The *fast* deflection signal of the cantilever is designed to track an appropriate trajectory instead of regulating a derivative signal such as the amplitude or phase.
- The control effort maybe directed through the dither or shake piezo by augmenting the sinusoidal dither signal with an additional dither control signal as well as the the vertical piezo signal.

In Section 3.1 a model to describe the cantilever dynamics is explained, which forms the basis for the model-based control design. Section 3.2 lays emphasis on the design of the reference trajectory that is used to impose force regulation on the cantilever subsystem. The forcing from the sample onto the cantilever is typically nonlinear in nature and is a function of the tip-sample distance as well as the sample and cantilever tip properties. In our design this force is modeled as a disturbance, thereby circumventing the problem of dealing with a nonlinear function and subsequent nonlinear control design (see Section 3.3). The control problem is posed, outlining the objectives, and the linear control design is described in detail in Section 3.4.

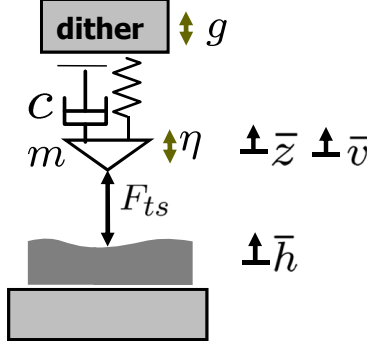


Figure 3.1: Spring-mass-damper model for cantilever subsystem

### 3.1 Model Details

In this work, the cantilever subsystem is modeled as a spring-mass-damper system with mass  $m$ , stiffness  $k$  and damping  $c$ , as shown in Figure 3.1. The governing ODE for the model considered is given by,

$$\frac{d^2 \bar{z}}{dt^2} + 2\zeta\omega_n \frac{d\bar{z}}{dt} + \omega_n^2 \bar{z} = \omega_n^2 \bar{u} + \omega_n^2 (g + \bar{v}) + \frac{1}{m} F_{ts}(\bar{z} - \bar{h}) \quad (3.1)$$

where  $\bar{z}$  is the global displacement of the cantilever,  $\omega_n$  the first modal frequency of the cantilever and  $\zeta$  the damping coefficient ( $c/m = 2\zeta\omega_n$ ). The signal  $\bar{u}$  denotes the control signal driving the cantilever, and it could comprise of dither and vertical piezo actuation, in addition to  $\bar{v}$  the vertical piezo movement. The nonlinear function  $F_{ts}$  represents the tip-sample interaction model, which is a function of the tip position ( $\bar{z}$ ) and sample topography ( $\bar{h}$ ). Some representative models in literature have been discussed in Section 2.2.2.

In the AFM configuration that we use, the sensing assembly moves with the cantilever. Therefore, the signal observed by the PSD is given by

$$\bar{p} = \bar{z} - \bar{v}.$$

Rewriting (3.1) in terms of  $\bar{p}$  and using  $(\dot{\phantom{x}})$  to represent  $\frac{d}{dt}$ , we obtain,

$$\ddot{\bar{p}} = -2\zeta\omega_n \dot{\bar{p}} - \omega_n^2 \bar{p} + \omega_n^2 g + \frac{1}{m} F_{ts}(\bar{p} + \bar{v} - \bar{h}) + \omega_n^2 (\bar{u} - \bar{v}/\omega_n^2). \quad (3.2)$$

The term  $(\bar{u} - \ddot{v}/\omega_n^2)$  is considered as the control signal to be designed and is represented by  $\bar{u}_2$  here onwards.

### 3.1.1 Non-dimensionalized State-space Representation

In the non-dimensionalized coordinates, the redefined time scale,  $\tau = \bar{\omega}t$ , where  $\bar{\omega}$  is chosen close to  $\omega_n$  for computational convenience. The notation  $(\cdot)$  implies  $\frac{d}{d\tau}(\cdot)$ . Suppose, the sinusoidal dither signal is written as  $g = b \cos(\omega t)$ , the redefined deflection, sample height, vertical actuation and control signals are  $p = \bar{p}/b$ ,  $h = \bar{h}/b$ ,  $v = \bar{v}/b$  and  $u_2 = \bar{u}_2$  respectively. The frequencies in the non-dimensionalized scale are,  $\Omega_n = \omega_n/\bar{\omega}$ ,  $\Omega = \omega/\bar{\omega}$ . The non-dimensionalized ODE is therefore deduced by, dividing both sides of (3.2) by  $\bar{\omega}^2 b$  and is written as,

$$\ddot{p} = -2\zeta\Omega_n\dot{p} - \Omega_n^2 p + \Omega_n^2 \cos(\Omega\tau) + \frac{\Omega_n^2}{F_0} F_{ts}(b\bar{p} + b\bar{v} - b\bar{h}) + \Omega_n^2 u_2. \quad (3.3)$$

Here the parameter  $F_0 = m\omega_n^2 b$  is used for simplicity.

To derive the necessary state-space equations,  $p$  is redefined as  $\begin{bmatrix} p_1 \\ p_2 \end{bmatrix}$ , and

$$\begin{aligned} \dot{p}_1 &= p_2, \\ \dot{p}_2 &= -2\zeta\Omega_n p_2 - \Omega_n^2 p_1 + \Omega_n^2 \cos(\Omega\tau) + \frac{\Omega_n^2}{F_0} F_{ts}(b\bar{p}_1 + b\bar{v} - b\bar{h}) + \Omega_n^2 u_2. \end{aligned} \quad (3.4)$$

Subsequently, defining

$$\begin{aligned} A_p &= \begin{bmatrix} 0 & 1 \\ -\Omega_n^2 & -2\zeta\Omega_n \end{bmatrix}, \\ B_p &= \begin{bmatrix} 0 \\ \Omega_n^2 \end{bmatrix}, \\ C_p &= \begin{bmatrix} 1 & 0 \end{bmatrix}, \\ D_p &= 0, \end{aligned} \quad (3.5)$$

gives the following non-dimensionalized state-space representation for the cantilever subsys-

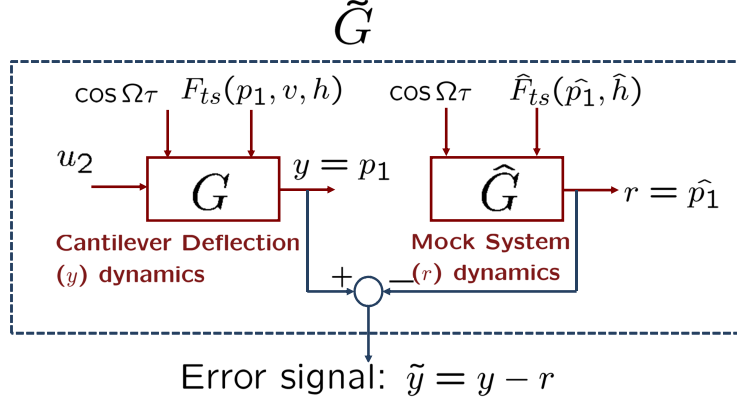


Figure 3.2: Schematic of error signal ( $\tilde{p}$ ) dynamics  $\tilde{G}$ ,  $G$  represents the physical cantilever dynamics and  $\hat{G}$  the mock system dynamics generated on the computer.

tem model,

$$\begin{aligned}\dot{p} &= A_p p + B_p(u_2 + \cos(\Omega\tau) + \frac{1}{F_0}F_{ts}), p(0) = p_0 \\ y &= C_p p + n.\end{aligned}\tag{3.6}$$

This state-space model is used as a representation of the physical cantilever subsystem for all control design considerations from here on. In this representation the output  $y$  is the measured deflection with measurement noise,  $n$ .

## 3.2 Reference Trajectory Design

A system similar to the cantilever subsystem described in (3.6) that is assumed to oscillate over an idealized, atomically flat sample, is considered and we term it as a ‘*mock system*’. The mock system inputs include sinusoidal actuation from the dither piezo and a model for the tip-sample interaction (where the sample input is assumed to be constant). The force model is used only in order to obtain a reasonable trajectory and does not influence the imaging mode otherwise in a significant manner. The actual cantilever subsystem can be thought of as the mock system augmented with forces from actual sample interactions and the controller inputs. The mock system dynamics in the non-dimensionalized coordinates defined in Section 3.1.1 are as follows,

$$\begin{aligned}\dot{\hat{p}}_1 &= \hat{p}_2, \\ \dot{\hat{p}}_2 &= -2\zeta\Omega_n\hat{p}_2 - \Omega_n^2\hat{p}_1 + \Omega_n^2\cos(\Omega\tau) + \frac{\Omega_n^2}{F_0}F_{ts}(b\bar{\hat{p}}_1 - b\bar{\hat{h}}),\end{aligned}\tag{3.7}$$

where  $\hat{p}_1$  is the mock system deflection,  $\zeta$ ,  $\Omega_n$ ,  $\Omega$ ,  $\tau$ , and  $F_0$  are as defined in Sections 3.1 and 3.1.1. The function  $F_{ts}$  represents the tip-sample interaction model, which in the case of the mock system is a function  $\hat{p}_1$  and a constant unvarying sample input  $\hat{h}$ . The signals  $\bar{\hat{p}}_1$  and  $\bar{\hat{h}}$  in (3.7) are the deflection and sample topography prior to non-dimensionalization. The same matrices as used in Section 3.1.1,  $A_p$ ,  $B_p$ ,  $C_p$  and  $D_p$  can be used to deduce the state-space representation of the mock system as follows,

$$\begin{aligned}\dot{\hat{p}} &= A_p\hat{p} + B_p(\cos(\Omega\tau) + \frac{1}{F_0}\hat{F}_{ts}), \hat{p}(0) = \hat{p}_0 \\ \hat{y} &= C_p\hat{p},\end{aligned}\tag{3.8}$$

where the state vector  $\hat{p}$  is  $\begin{bmatrix} \hat{p}_1 \\ \hat{p}_2 \end{bmatrix}$ . The force term  $\hat{F}_{ts}$  denotes  $F_{ts}(b\bar{\hat{p}}_1 - b\bar{\hat{h}})$ . The signal  $\hat{p}_1$  provides the reference trajectory that the cantilever deflection must track in order to accomplish force regulation.

### 3.2.1 Error Dynamics

The error between the cantilever deflection and designed reference trajectory is defined by  $\tilde{p} = p - \hat{p}$ . This error dynamics can be described as,

$$\begin{aligned}\dot{\tilde{p}} &= A_p\tilde{p} + B_p[u_2 + (\frac{1}{F_0}F_{ts}(b\bar{p}_1 + b\bar{v} - b\bar{h}) - \frac{1}{F_0}\hat{F}_{ts}(b\bar{\hat{p}}_1 - b\bar{\hat{h}}))], \tilde{p}(0) = p_0 - \hat{p}_0, \\ \tilde{y} &= C\tilde{p} + n.\end{aligned}\tag{3.9}$$

A simple schematic of the error dynamics, which is termed  $\tilde{G}$  is depicted in Figure 3.2. The output of the error system  $\tilde{G}$  is defined to be  $\tilde{y}$ , which is the error between the cantilever deflection signal from the physical system and the reference trajectory generated by the mock system dynamics. The reference signal in this case  $\tilde{r}$  is taken to be zero. Regulation of the error  $\tilde{y}$  to zero accomplishes the tracking objective for the deflection signal. It may be

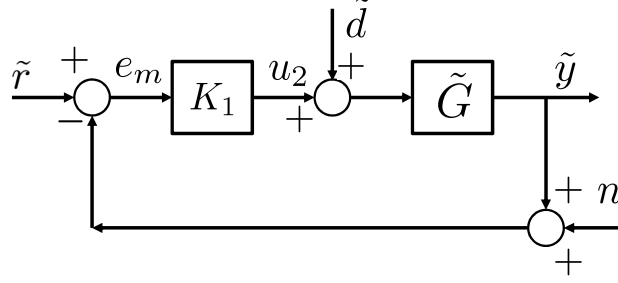


Figure 3.3: Closed-loop feedback diagram with  $\tilde{G}$  and  $K_1$ , treating inter-atomic forces between tip and sample as disturbance

noted that the tip-sample interaction terms are typically modeled using nonlinear functions.

### 3.3 Tip-Sample Interaction Forces as Disturbance

In the control design that follows, the tip-sample interaction force terms in the error dynamics described in (3.9) are treated as disturbance. With  $\tilde{G}$  representing the error dynamics, first a regulation problem is posed to regulate the output of the error system  $\tilde{y}$  (Figure 3.2) to zero. This guarantees the tracking objective of the cantilever deflection to track the reference trajectory designed. Additionally, by modeling the interaction force as a disturbance, the nonlinearities induced to the  $p$  and  $\hat{p}$  by the tip-sample interaction is captured by the disturbance term. The error dynamics in (3.9) can be rewritten as,

$$\begin{aligned}\dot{\tilde{p}} &= A_p \tilde{p} + B_p [u_2 + \tilde{d}], \tilde{p}(0) = p_0 - \hat{p}_0, \\ \tilde{y} &= C \tilde{p} + n,\end{aligned}\tag{3.10}$$

where  $\tilde{d}$  denotes the disturbance and is equivalent to  $\frac{1}{F_0}[F_{ts}(b\bar{p}_1 + b\bar{v} - b\bar{h}) - \hat{F}_{ts}(b\bar{\hat{p}}_1 - b\bar{\hat{h}})]$ . It may be noted that estimating this disturbance  $\tilde{d}$  is equivalent to estimating the tip-sample interaction forces in the real system  $F_{ts}$  since  $\hat{F}_{ts}$  is generated by the computer and therefore a known quantity.

The estimation of the interaction force between the tip and sample can be used to derive topographical as well as other physical properties of the sample. The method of estimation is explained in Section 4.1.



## 3.4 Control Design

### 3.4.1 Control Objectives

The key control aim is to regulate the error  $\tilde{y}$  to zero through disturbance rejection. The control objectives that are sought by the optimal controller are as follows,

- Regulation of  $\tilde{y}$  through disturbance rejection.
- Robust stability to any modeling uncertainties and external disturbances.
- Noise attenuation in closed-loop.
- Low effort of control.

The control design is optimized to achieve the objectives listed. The relevant closed-loop signals required for this design are,

$$\begin{aligned}\tilde{y} &= (\tilde{r} - n) + \tilde{G}S\tilde{d}, \\ e_m &= S(\tilde{r} - n) - \tilde{G}S\tilde{d}, \\ u_2 &= K_1S(\tilde{r} - n) - K_1\tilde{G}S\tilde{d},\end{aligned}\tag{3.11}$$

where  $e_m = \tilde{r} - \tilde{y} - n$ ,  $S = 1/(1 + \tilde{G}K_1)$  and  $T = 1 - S = \tilde{G}K_1/(1 + \tilde{G}K_1)$ . The error  $e_m$  can be made small by designing  $S$  such that  $S$  and consequently  $\tilde{G}S$  are small in the frequency regions where  $\tilde{r}$ ,  $n$  and  $\tilde{d}$  are dominant. The bandwidth  $\omega_{BW}$  of  $S$  characterizes the disturbance rejection bandwidth of the closed-loop system. Designing  $T$  to have small roll-off frequency and high roll-off rates ensures high resolution. Robustness to external disturbances is measured by the peak magnitude value of  $S$ . Making  $\|S\|_\infty$  to be close to 1 improves robustness to modeling uncertainties and disturbances. For the regulation problem the reference signal  $\tilde{r}$  is set to zero.

### 3.4.2 Disturbance Rejection

The desired objectives are formulated in an optimal control setting based on  $\mathcal{H}_\infty$  stacked sensitivity framework [30] (see Figure 3.4). The objectives of robust stability, disturbance

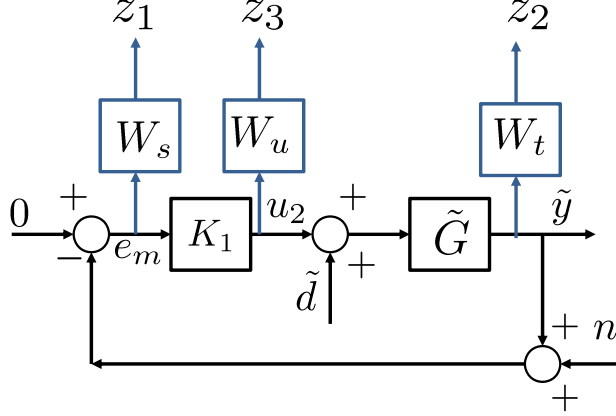


Figure 3.4: Closed-loop system with weighting functions for the  $\mathcal{H}_\infty$  stacked sensitivity framework

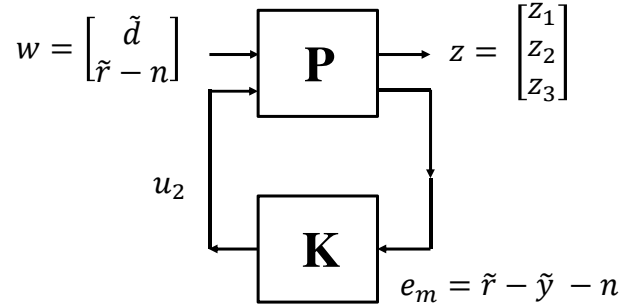


Figure 3.5: Open-loop system  $P$  in feedback with the designed controller  $K_1$

rejection and noise attenuation are realized by shaping the closed-loop transfer functions  $S$  and  $T$  using weighting functions  $W_s$  and  $W_t$ . The weighting function  $W_u$  imposes boundedness of the control signal  $u_2$ . The weighted error in regulation  $z_1 = W_s e_m$ , weighted output  $z_2 = W_t \tilde{y}$  and weighted dither control signal  $z_3 = W_u u_2$  are chosen to be the regulated outputs. The closed-loop transfer function from  $w = \begin{bmatrix} \tilde{d} & \tilde{r} - n \end{bmatrix}^T$  to  $z = \begin{bmatrix} z_1 & z_2 & z_3 \end{bmatrix}^T$  is given by,

$$\begin{bmatrix} z_1 \\ z_2 \\ z_3 \end{bmatrix} = \underbrace{\begin{bmatrix} -W_s \tilde{G} S & W_s S \\ W_t \tilde{G} S & W_t T \\ -W_u T & W_u K_1 S \end{bmatrix}}_{\Phi} \begin{bmatrix} \tilde{d} \\ \tilde{r} - n \end{bmatrix}. \quad (3.12)$$

The open-loop system  $P$  with external inputs  $[w \ u_2]$  and output  $z$  is represented as a block diagram in Figure 3.5. From (3.12) it is observed that there are a few constraints in

the minimization of the closed-loop transfer function ( $\Phi$ ) from  $w$  to  $z$ . For instance, the fundamental limitation  $S + T = I$ , conflicts with the simultaneous minimization of terms  $W_t\tilde{G}S$  and  $W_tT$ . This limits the set of feasible controllers that guarantee small values of  $\|\Phi\|_\infty$ . However, the sought objectives can be accomplished by selective minimization of certain  $\Phi$  terms.

We reduce the problem to the minimization of specific transfer functions,  $\mathbf{W}_s\tilde{\mathbf{G}}\mathbf{S}$ ,  $\mathbf{W}_s\mathbf{S}$ ,  $\mathbf{W}_t\mathbf{T}$  and  $\mathbf{W}_u\mathbf{K}_1\mathbf{S}$  by observing that this minimization achieves closed-loop properties analogous to our desired objectives. The minimization of the transfer functions  $W_s\tilde{G}S$  and  $W_sS$  accomplish the disturbance rejection and robustness to uncertainties objectives. The aims of noise attenuation and low control effort are achieved through minimization of  $W_tT$  and  $W_uK_1S$  respectively.

Such selective minimization is made possible by the multi-objective scheme proposed in [31]. The term  $-W_s\tilde{G}S$  is the transfer function from  $\tilde{d}$  to  $z_1$  and  $\begin{bmatrix} W_sS & W_tT & W_uK_1S \end{bmatrix}^T$  is the transfer function from  $\tilde{r} - n$  to  $\begin{bmatrix} z_1 & z_2 & z_3 \end{bmatrix}^T$ . These constitute the cost functions to be minimized in the multiobjective optimization problem, which is described as,

$$\min_{K_1 \in \mathbf{K}} \gamma \left\| W_s\tilde{G}S \right\|_\infty + \left\| \begin{bmatrix} W_sS \\ W_tT \\ W_uK_1S \end{bmatrix} \right\|_\infty \quad (3.13)$$

where  $\gamma$  is a parameter used to define relative importance between the two cost objectives. The set  $\mathbf{K}$  comprises of all the feasible stabilizing controllers  $K_1$ . This multiobjective optimization problem can be cast in terms of linear matrix inequalities (LMIs) [31]. Section 3.4.3 explains the details of the LMI solution formulation. The corresponding LMI conditions for our multiobjective problem can be stated as follows: A solution to the multiobjective optimization problem in (3.13) exists if there exists a solution  $(\hat{A}, \hat{B}, \hat{C}, \hat{D}, R, S, \alpha_1, \alpha_2)$  to the optimization problem,

$$\begin{aligned}
& \min \quad \gamma\alpha_1 + \alpha_2 \\
& \text{subject to} \\
& (i) \quad \begin{bmatrix} \mathcal{Q}(AR + B\hat{C}) & (*) & (*) & (*) \\ \hat{A} + (A + B\hat{D}C)^T & \mathcal{Q}(SA + \hat{B}C) & (*) & (*) \\ (U_1 + B\hat{D}H_1)^T & U_1^T S + H_1^T \hat{B}^T & -\alpha_1 I & (*) \\ V_1 R + E_1 \hat{C} & V_1 + E_1 \hat{D}C & D_1 & -\alpha_1 I \end{bmatrix} < 0 \\
& (ii) \quad \begin{bmatrix} \mathcal{Q}(AR + B\hat{C}) & (*) & (*) & (*) \\ \hat{A} + (A + B\hat{D}C)^T & \mathcal{Q}(SA + \hat{B}C) & (*) & (*) \\ (U_2 + B\hat{D}H_2)^T & U_2^T S + H_2^T \hat{B}^T & -\alpha_2 I & (*) \\ V_2 R + E_2 \hat{C} & V_2 + E_2 \hat{D}C & D_2 & -\alpha_2 I \end{bmatrix} < 0 \\
& (iii) \quad \begin{bmatrix} R & (*) \\ I & S \end{bmatrix} > 0.
\end{aligned} \tag{3.14}$$

Here  $U_j = B_1 R_j$ ,  $V_j = L_j C_1$ ,  $D_j = L_j D_{11} R_j$ ,  $E_j = L_j D_{12}$  and  $H_j = D_{21} R_j$  and the operation  $\mathcal{Q}(L) = L + L^T$ . The terms denoted by  $(*)$  can be inferred by symmetry. The convex optimization problem in (3.14) is solvable using standard tools and from its solution,  $(A_k, B_k, C_k, D_k)$  can be retrieved since  $N$  and  $M$  are invertible. See Section 3.4.3 for more details.

With appropriately designed shaping functions  $W_s$ ,  $W_t$  and  $W_u$ , the LMI solution  $[A_k, B_k, C_k, D_k]$  gives the most optimal controller  $K_1$  in the feasible set. The shaping functions are constructed carefully to achieve the performance objectives of robust stability, disturbance rejection and noise attenuation. For instance, need for high resolution requires the roll-off frequency of  $T$  to be small which is accommodated in the choice of  $W_t$ . Similarly, the high bandwidth and robustness aspects require  $S$  to be small over a wide range of frequencies and close to 1 values of  $\|S\|_\infty$ . This is addressed by the choice of  $W_s$ .

### 3.4.3 LMI Solution

The formulation of the multiobjective optimization problem in the LMI framework in [31] is presented in this section. First, the generalized plant matrix  $P$  (see Figure 3.5) is considered,

which takes the form,

$$\begin{bmatrix} z_1 \\ z_2 \\ z_3 \\ e_m \end{bmatrix} = \underbrace{\begin{bmatrix} -W_s\tilde{G} & W_s & -W_s\tilde{G} \\ W_t\tilde{G} & 0 & W_t\tilde{G} \\ 0 & 0 & W_u \\ -\tilde{G} & I & -\tilde{G} \end{bmatrix}}_P \begin{bmatrix} \tilde{d} \\ r-n \\ u_2 \end{bmatrix}. \quad (3.15)$$

As defined in Section 3.4.2,  $w = \begin{bmatrix} \tilde{d} & \tilde{r} - n \end{bmatrix}^T$  and  $z = \begin{bmatrix} z_1 & z_2 & z_3 \end{bmatrix}^T$ . Then state-space realization of  $P$  is given by,

$$\begin{aligned} \dot{x} &= Ax + B_1w + Bu_2, \\ z &= C_1x + D_{11}w + D_{12}u_2, \\ e_m &= Cx + D_{21}w \end{aligned} \quad (3.16)$$

where  $A$ ,  $B_1$  and  $B$  are the appropriate state-space matrices for the cantilever subsystem model. The other system matrices follow from (3.15) and  $x$  is the system state vector. The state-space representation of the feedback controller  $K_1$  is written as,

$$\begin{aligned} \dot{x}_k &= A_kx_k + B_ke_m, \\ u_2 &= C_kx_k + D_ke_m, \end{aligned} \quad (3.17)$$

with  $x_k$  being the state vector of  $K_1$ . The overall closed-loop function  $\Phi$  in terms of this state-space realization can now be computed as,

$$\begin{aligned} \Phi &= \left[ \begin{array}{cc|c} A + BD_kC & BC_k & B_1 + BD_kD_{21} \\ \hline BkC & A_k & B_kD_{21} \\ \hline C_1 + D_{12}D_kC & D_{12}C_k & D_{11} + D_{12}D_kD_{21} \end{array} \right] \\ &=: \left[ \begin{array}{c|c} \bar{A} & \bar{B} \\ \hline \bar{C} & \bar{D} \end{array} \right] \end{aligned} \quad (3.18)$$

We seek an optimal controller of the form (3.17) that imposes  $\mathcal{H}_\infty$  performance on the specific transfer functions,

$$\begin{aligned}\Phi_1 &= W_s \tilde{G} S, \\ \Phi_2 &= \begin{bmatrix} W_s S & W_t T & W_u K_1 S \end{bmatrix}^T.\end{aligned}\tag{3.19}$$

This allows us to follow the LMI framework adopted in [31] and [6]. Therefore, we define the following  $L_j$  and  $R_j$  matrices for  $j = 1, 2$ ,

$$L_1 = \begin{bmatrix} 1 & 0 & 0 \end{bmatrix} \quad R_1 = \begin{bmatrix} 1 & 0 \end{bmatrix}^T,\tag{3.20}$$

$$L_2 = \begin{bmatrix} 1 & 0 & 0 \\ 0 & 1 & 0 \\ 0 & 0 & 1 \end{bmatrix} \quad R_2 = \begin{bmatrix} 0 & 1 \end{bmatrix}^T.\tag{3.21}$$

The choice of the  $L_j$  and  $R_j$  matrices in (3.20) and (3.21) are such that,  $\Phi_1 = L_1 \Phi R_1$  and  $\Phi_2 = L_2 \Phi R_2$ . Let  $U_j = B_1 R_j$ ,  $V_j = L_j C_1$ ,  $D_j = L_j D_{11} R_j$ ,  $E_j = L_j D_{12}$  and  $H_j = D_{21} R_j$ . Also,  $\bar{B} R_j$ ,  $L_j \bar{C}$  and  $L_j \bar{D} R_j$  are denoted by  $\bar{B}_j$ ,  $\bar{C}_j$  and  $\bar{D}_j$  respectively. Then each  $\Phi_j$  for  $j = 1, 2$ , is

$$\Phi_j = \left[ \begin{array}{c|c} \bar{A} & \bar{B}_j \\ \hline \bar{C}_j & \bar{D}_j \end{array} \right].\tag{3.22}$$

In order to impose the  $\mathcal{H}_\infty$  performance objective, we require  $\|\Phi_j\|_\infty < \alpha_j$  for  $\alpha_j > 0$ . This is equivalent to the existence of  $P_j > 0$  such that,

$$\begin{bmatrix} \bar{A}^T P_j + P_j \bar{A} & (*) & (*) \\ \bar{B}_j^T P_j & -\alpha_j I & (*) \\ \bar{C}_j & \bar{D}_j & -\alpha_j I \end{bmatrix} < 0,\tag{3.23}$$

see [32]. However, this is not directly in the LMI form since the terms in (3.23) are not linear in the variables to be designed,  $(A_k, B_k, C_k, D_k)$ . In order to get LMI realization the

following condition is imposed,

$$P_j = P, \text{ (for } j = 1, 2)$$

and the following transformations are performed. The following decomposition of the solution  $P$  is used,

$$P = \begin{bmatrix} S & N \\ N^T & ? \end{bmatrix}, \quad P^{-1} = \begin{bmatrix} R & M^T \\ M^T & ? \end{bmatrix} \quad (3.24)$$

where ?s denote insignificant terms. Further we define a transformation in terms of the following matrices

$$\Pi_1 = \begin{bmatrix} R & I \\ M^T & 0 \end{bmatrix}, \quad \Pi_2 = \begin{bmatrix} I & S \\ 0 & N^T \end{bmatrix}. \quad (3.25)$$

The decomposition of  $P$  in (3.24) and the fact that  $PP^{-1} = P^{-1}P = I$  implies  $MN^T = I - RS$ ,  $P\Pi_1 = \Pi_2$ . The redefined variables,

$$\begin{aligned} \hat{A} &= NA_k M^T + NB_k CR + SBC_k M^T \\ &\quad + S(A + BD_k C)R, \\ \hat{B} &= NB_k + SBD_k, \\ \hat{C} &= C_k M^T + D_k CR, \\ \hat{D} &= D_k, \end{aligned} \quad (3.26)$$

are used to formulate the optimization problem in terms of LMIs. Upon imposing  $\mathcal{H}_\infty$  performance on both  $\phi_1$  and  $\phi_2$ , we get equations of the form shown in (3.23). Through appropriate congruent transformations  $\text{diag}(\Pi_1, I, I)$ , the LMI conditions (i) and (ii) in (3.14) are deduced. Subsequently,  $\Pi_1^T P \Pi_1$  gives the inequality condition (iii) in (3.14).

From the optimized variables  $(\hat{A}, \hat{B}, \hat{C}, \hat{D}, R, S)$ , with  $M$  and  $N$  being invertible, the

matrices  $(A_k, B_k, C_k, D_k)$  are got as follows:

$$\begin{aligned}
A_k &= N^{-1}(\hat{A} - (\hat{B} - SB\hat{D})CR - SB(\hat{C} - \hat{D}CR) \\
&\quad - S(A + B\hat{D}C)R)M^{-T} \\
B_k &= N^{-1}(\hat{B} - SB\hat{D}) \\
C_k &= (\hat{C} - \hat{D}CR)M^{-T} \\
D_k &= \hat{D}
\end{aligned} \tag{3.27}$$

The state-space matrices  $(A_k, B_k, C_k, D_k)$  represent the optimal controller  $K_1$  for the cantilever model.

#### 3.4.4 Choice of Weighting Functions

Appropriate design of the weighting functions,  $W_s$ ,  $W_t$ , and  $W_u$  (from Figure 3.4) is crucial for achieving the desired control objectives. In the stacked sensitivity framework, the loop transfer function  $G_c K_1$  is shaped by designing closed-loop functions, namely the sensitivity function  $S$  and complementary sensitivity function  $T$  as desired. Imposing  $\|W_s S\|_\infty < 1$  on the design of  $S$  applies a lower bound on the bandwidth of the closed-loop system. An upper bound is applied to the magnitude of the function  $T$  through  $1/|W_t|$  ensuring that the loop transfer function rolls off sufficiently fast at higher frequencies beyond the frequency region of interest. And the weighting function  $W_u$  is used to limit the magnitude of control input signals to  $1/|W_u|$ .

A cantilever subsystem with a natural frequency of 69.578 kHz, stiffness  $k$  of 1.43, and damping  $\zeta = 0.0033$  was considered for the following choice of weighting functions. The system equations are normalized as described in Section 3.1 with  $\bar{\omega} = \omega_n$  and  $b = 2.9155$  nm. For the design of the controller  $K_1$ , the shaping functions,  $W_s = \frac{0.3(s+35.93)}{s+0.1078}$ ,  $W_t = \frac{100(s+3.593)}{s+1078}$  and  $W_u = 0.1$  were chosen to capture the performance objectives of high bandwidth, resolution and robustness to disturbances. The choice of these transfer functions is dependent on the specific system properties and requirements. The sensitivity function  $S$  is designed to be small in a wide range of frequencies where the signals  $\tilde{r}$  and  $\tilde{d}$  are dominant. However, the reference signal in our regulation problem  $\tilde{r}$  is chosen to be zero and  $W_s$  is chosen to have a



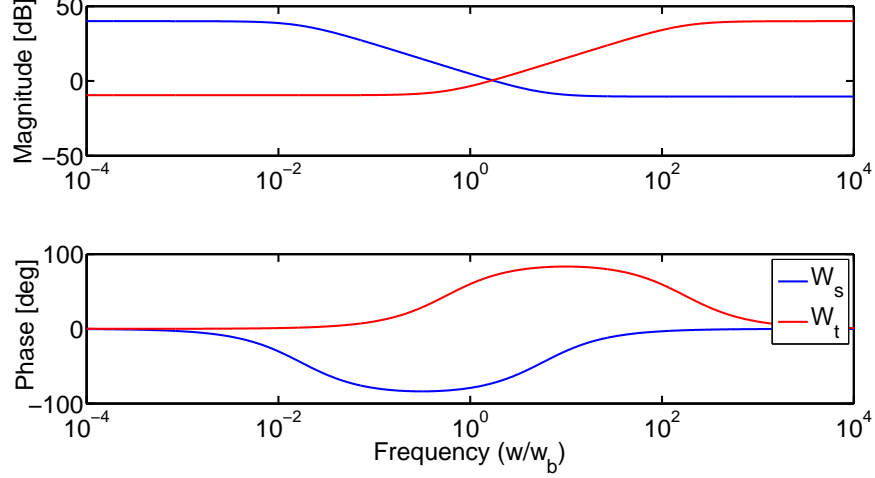


Figure 3.6: Weighting functions  $W_s$  and  $W_t$  for the design of closed-loop functions  $S$  and  $T$

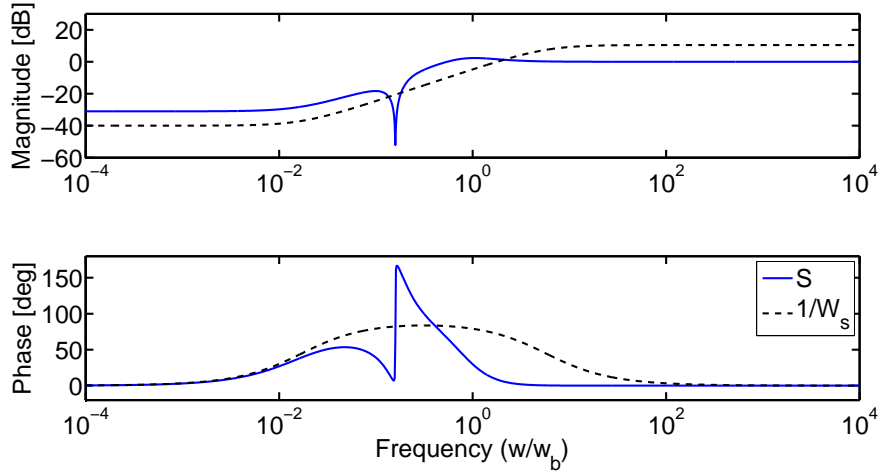


Figure 3.7: Design of sensitivity function  $S$ : Bode plot showing  $S$  and the weighting function used  $\frac{1}{W_s}$ .

disturbance rejection bandwidth of 10% – 15% of the cantilever’s first resonance frequency.

In addition,  $W_s$  ensures that  $\|S\|_\infty$  is small ( $\approx 1.3020$ ), guaranteeing the robustness condition. Although, we require  $S$  to be made small in a wide range of the operating frequency, it cannot be made small in regions where the complementary sensitivity function  $T$  is small. This is a consequence of the fundamental limitation that  $S + T = I$ . A small enough roll-off frequency and high roll-off rates for the loop function are imposed by the weighting function  $W_t$ . The weighting function  $W_u$  is chosen to be a constant that limits the control signal effort. A few values for  $W_u$  were tried to determine that limiting value at

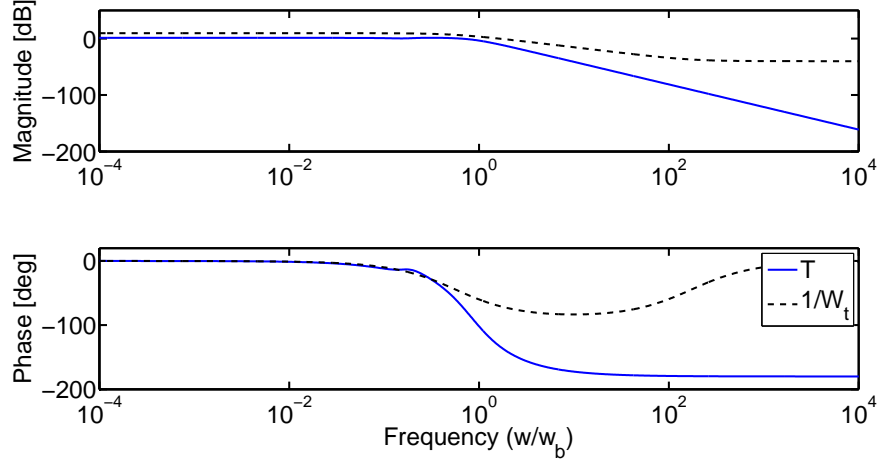


Figure 3.8: Design of complementary sensitivity function  $T$ : Bode plot showing  $T$  and the weighting function used  $\frac{1}{W_t}$ .

which the optimization fails. This parameter limits the set of feasible controllers considered during optimization.

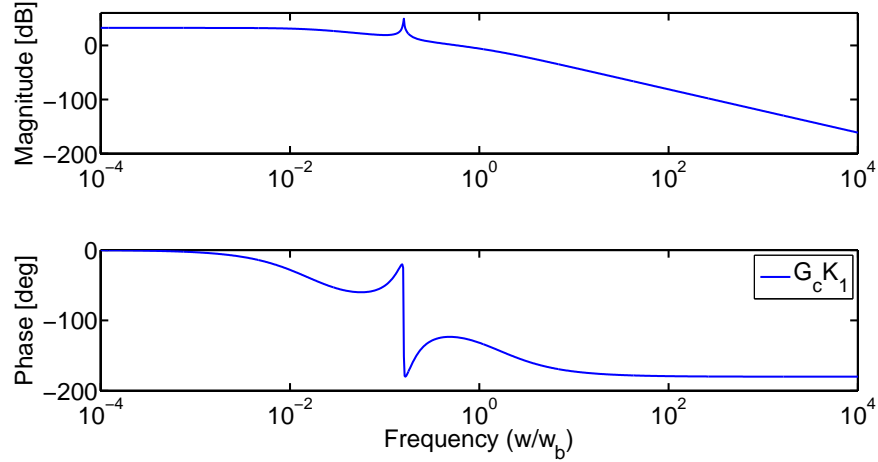


Figure 3.9: Magnitude and phase plots of the loop transfer function  $L = \tilde{G}K_1$ . The weighting functions limit the peak value and define the roll-off rates at high frequencies.

Bode plots of  $W_s$  and  $W_t$  are illustrated in Figure 3.6. This is followed by plots of the designed closed-loop transfer functions  $S$  and  $T$  in Figures 3.7 and 3.8 respectively. The weighting functions  $1/W_s$  and  $1/W_t$  are shown in black dotted lines. The performance of the optimization solution can be seen from these plots. In all the magnitude and phase plots in this section, the logarithmic frequency axis has no units owing to non-dimensionalization using  $\bar{\omega}$  (denoted by  $w_b$  in the plots).

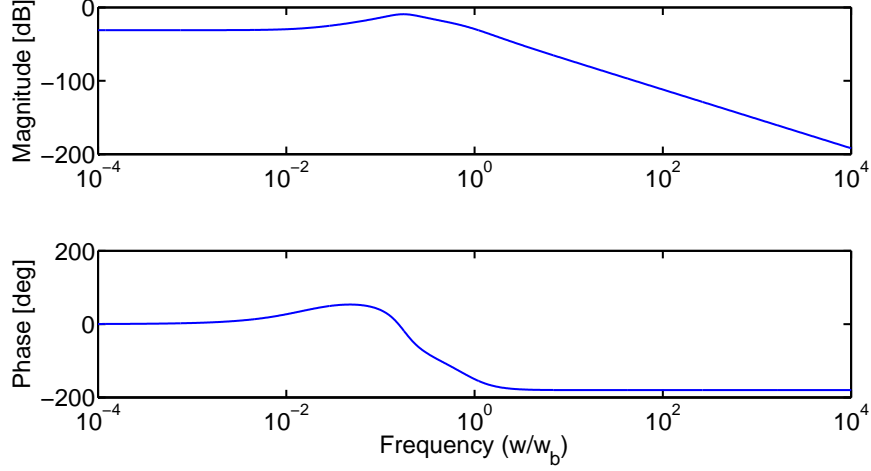


Figure 3.10: Magnitude and phase plots of the closed-loop transfer function  $G_c S$

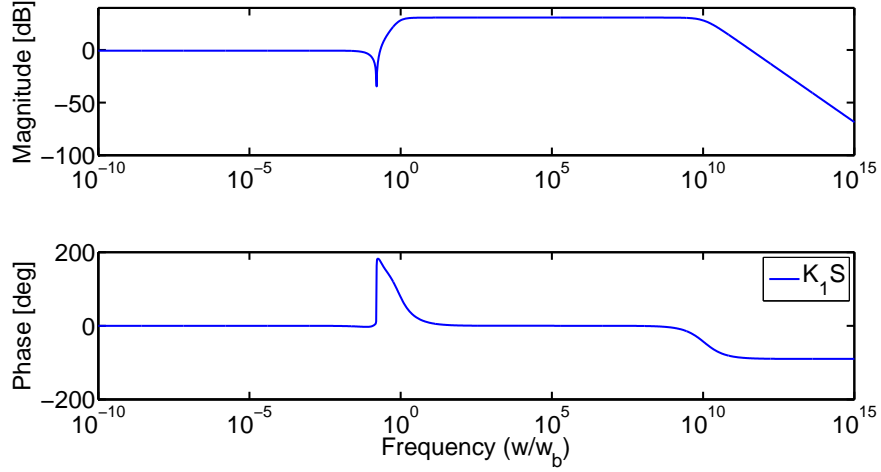


Figure 3.11: Magnitude and phase plots of the the closed-loop transfer function  $K_1 S$

### 3.4.5 Minimization Solution

In Figure 3.12 a table showing the infinity-norm values of the elements in the closed-loop matrix  $\Phi$  in (3.12) are presented along with the corresponding plot depicting the same. The terms are shown as  $\Phi_{ij}$  where  $i$  and  $j$  denote the row and column of the elements in the matrix respectively. The minimization problem with the given transfer function choices for  $W_s$ ,  $W_t$  and  $W_u$  yields  $\|\Phi_1\|_\infty = 3.4535$  and  $\|\Phi_2\|_\infty = 3.4587$ , where  $\Phi_1$  and  $\Phi_2$  are defined in (3.19). The controller  $K_1$  after minimal realization is computed to be,

$$K_1 = \frac{2.357 \times 10^{12} s^3 + 2.543 \times 10^{15} s^2 + 2.026 \times 10^{15} s + 2.899 \times 10^{15}}{s^4 + 6.84 \times 10^{10} s^3 + 7.436 \times 10^{13} s^2 + 6.616 \times 10^{14} s + 7.045 \times 10^{13}}. \quad (3.28)$$

$  \Phi  _\infty$ values	
$\Phi_{11}$	3.4535
$\Phi_{12}$	3.3300
$\Phi_{21}$	0.1192
$\Phi_{22}$	3.4456
$\Phi_{31}$	0.1126
$\Phi_{32}$	0.5063

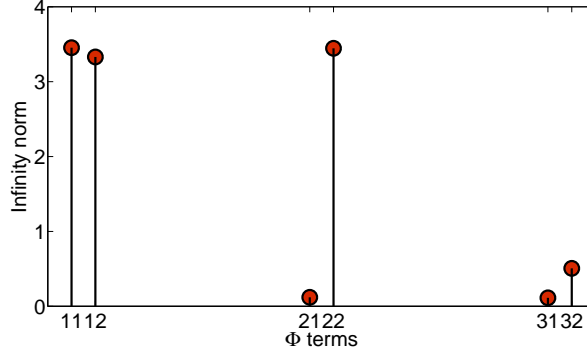


Figure 3.12:  $||\cdot||_\infty$  norms of the terms in closed-loop matrix  $\Phi$  (see (3.12)) upon minimization. The subscripts denote the position of the element in the matrix.

The magnitude and phase characteristics of the resultant loop transfer function  $\tilde{G}K_1$  is shown in Figure 3.9. The high roll-rates at higher frequencies is a consequence of the  $W_t$  design. It must be noted that as a result of non-dimensionalization,  $10^0$  on the frequency axis corresponds to the first resonance frequency of the cantilever. Closed-loop simulations of the

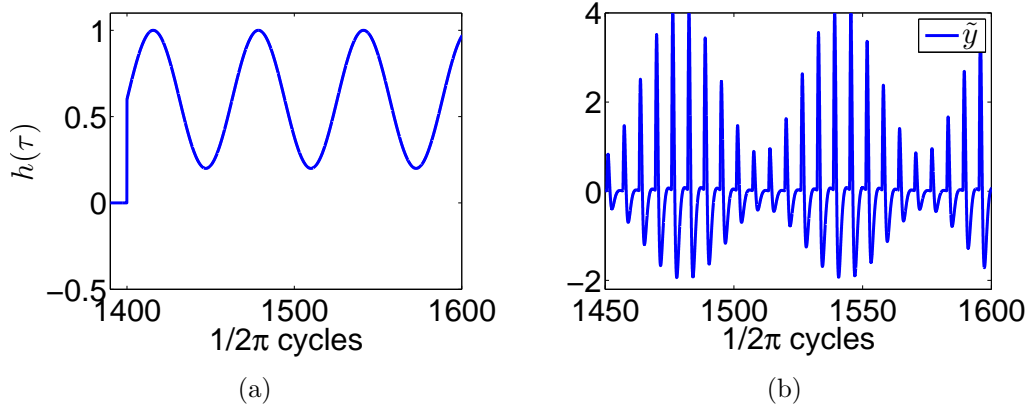


Figure 3.13: (a) shows the normalized height profile with frequency  $\frac{\omega_h}{\omega} = 0.1$  and amplitude  $\frac{a_h}{b} = 0.4$ . (b) The regulating action of the controller  $K_1$  makes  $\tilde{y} = \tilde{p}_1$  settle to zero within a cycle after every tip-sample interaction. These interactions are in the form of impulses, causing instantaneous state jumps of  $p_1$  as seen in this plot of  $\tilde{y}$ .

controller  $K_1$  in feedback with the error subsystem  $\tilde{G}$  were performed on Matlab Simulink. The normalized sinusoidal sample profile shown in Figure 3.13(a), whose amplitude is  $a_h/b$  and frequency is  $\omega_h/\omega$ . The DMT model was chosen to model the tip-sample interaction forcing in the systems  $G$  and  $\hat{G}$ , which has been widely corroborated in literature [4], [33]. The tip sample interaction  $d$  occurs in the form of impulses, each time the cantilever inter-

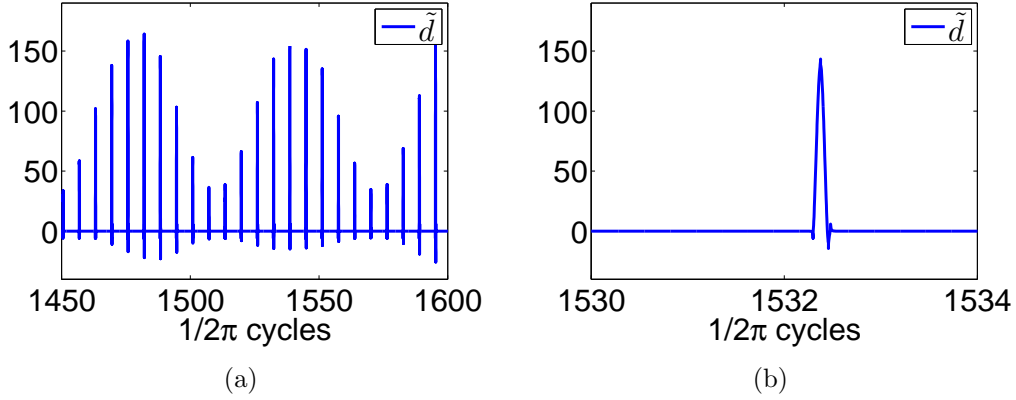


Figure 3.14: (a) The forcing from the tip sample interaction occurs as an impulse resulting in instantaneous value change of  $p_1$  and hence  $\tilde{p}$ . When the cantilever is within a small distance from the sample, the interaction force impulses occur once every period of oscillation as shown in (b). Note that the x-axis shows  $\frac{1}{2\pi}$  cycles.

acts with the sample,  $p_1$  assumes a different value instantaneously when this happens (see Figures 3.14(a), 3.14(b)). The magnitude of the resultant disturbance signal  $\tilde{d}$  is maintained small by the design of  $\hat{d}$ . However, it is not required for the mock system to have a disturbance signal  $\hat{d}$  as long as the amplitude of the reference trajectory is appropriately generated to effect the desired forcing on the sample and satisfy force regulation.

It can be observed that the interaction force  $\tilde{d}$  occurs as impulses or spikes (see Figure 3.14(a)). This is because the cantilever spends only a small fraction of each cycle in contact (i.e. within atomic scale separation) with the sample surface. Therefore, reducing the amplitude of oscillation of the cantilever will increase the time spent in contact with the sample thereby making the impulse like forcing smoother. But very low amplitudes could cause the cantilever to remain in attractive force region during most of its oscillation causing it to snap on to the surface.

The cantilever is made to stay predominantly in the repulsive region in accordance to dynamic mode of imaging in AFM. Furthermore, the regulating action of controller  $K_1$  brings  $p_1$  to  $\hat{p}_1$  or equivalently  $\tilde{p}$  to 0 within a cycle as seen in Figure 3.13(b). As long as the effective sample spatial frequency is within 15 – 20% of the cantilever resonance frequency, force regulation is attained [34]. However, this does not limit the bandwidth of sample

property or topography estimation as will be seen in Chapter 4. The loop shaping is done for the best possible force regulation bandwidth, i.e. disturbance rejection bandwidth.

### 3.5 Summary

The control system perspective from Chapter 2 was adopted and cantilever dynamics were modeled in accordance to this systems setup. A tracking problem on the cantilever deflection to achieve force regulation was successfully formulated, followed by design of a  $\mathcal{H}_\infty$ -based controller that regulates the tracking error to zero. The step-by-step details of constructing this regulating controller were discussed. Finally, the favorable performance results on simulations were presented. In the following chapter methods to estimate the rejected disturbance, followed by sample property estimation are discussed.

# CHAPTER 4

## SAMPLE PROPERTY ESTIMATION

Separation of the goals of force regulation and force estimation, allows for a high disturbance estimation bandwidth. This is explored in this chapter by designing a controller that acts upon the output of the error subsystem  $\tilde{G}$  from Section 3.2.1. It has already been established that current amplitude modulation techniques or tapping mode operation do not suffice for high-speed operations, because of change in cantilever amplitude even within a cycle of its oscillation. As a consequence, the current methods of sample topography estimation directly using the control signal are also erroneous at high-speeds.

The proposed dynamic mode of imaging compensates for the effect of forcing from the sample through force regulation. Furthermore, in place of estimating the sample topography, a transfer function that can estimate the forces due to sample interaction is sought, which gives a more direct/raw form of data. Design for disturbance estimation is given in Section 4.1. Methods to use the force data to obtain sample topography estimates are discussed in Section 4.2.2. In order to get the physical properties of sample from the force estimates, it is important to understand typical forcing models. Using these models as reference a generic force model is adopted and a few example techniques to deduce sample properties using this generic model are shown in Section 4.2.3.

### 4.1 Disturbance Estimation

This section deals with the design of controller  $K_2$  (see Figure 4.1) such that,  $\hat{\tilde{d}} = K_2 e_m$  gives an estimate of the tip sample interaction force difference  $\tilde{d}$ . In the AFM setup, the deflection  $p_1$  is measurable from sensors, and  $\hat{p}_1$  is also known since it is a state of the mock

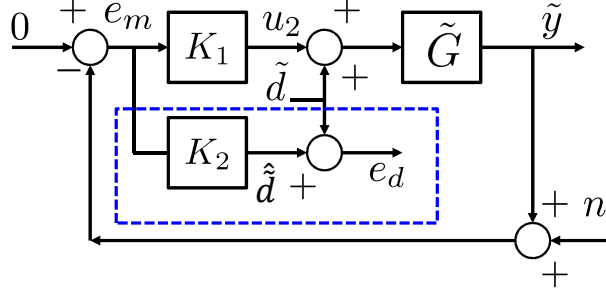


Figure 4.1: The controller  $K_2$  used to estimate the disturbance  $\tilde{d}$  from the regulation error signal  $e_m$ , highlighted by the blue box. The estimate is denoted by  $\hat{\tilde{d}}$  and the estimation error by  $e_d$ .

system. An estimate of  $\tilde{d}$  can be numerically obtained from  $\tilde{y}$  since,

$$\tilde{y} = p_1 - \hat{p}_1 = \tilde{G}S\tilde{d}. \quad (4.1)$$

Therefore,  $S^{-1}\tilde{G}^{-1}\tilde{y}$  is an estimate of  $\tilde{d}$  when  $S$  is a minimum phase transfer function.

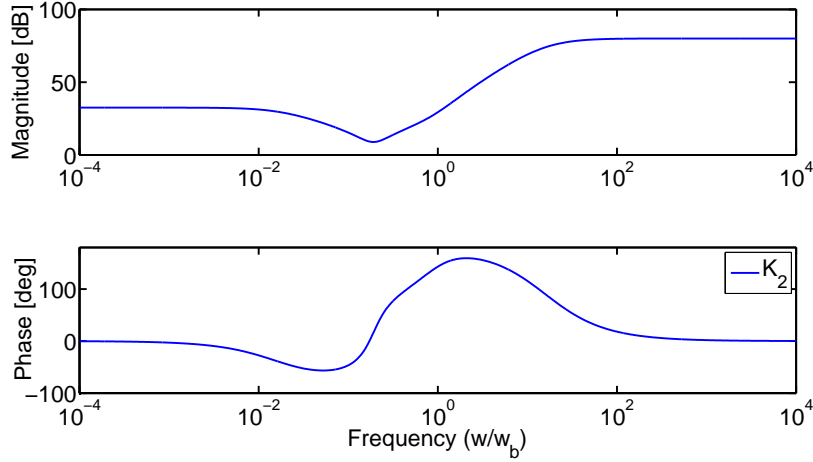


Figure 4.2: Bode diagram of the force estimating controller  $K_2$

However, when the transfer function is non-minimum phase, the Nevanlinna-Pick method can be adopted to design an appropriate inverse transfer function through a minimization problem [35]. Furthermore, we append a stable second-order low-pass filter  $\Psi$ , whose cut-off frequency  $\omega_F$  is larger than the resonance frequency and therefore larger than the highest frequency component of  $h$  considered. This guarantees that the transfer function from  $n$  to



$\hat{\tilde{d}}$  rolls off at high frequencies. Therefore, the controller  $K_2$  is designed as

$$K_2 = -S^{-1}\tilde{G}^{-1}\Psi. \quad (4.2)$$

Accordingly  $\hat{\tilde{d}} = K_2 e_m$  is used as an estimate of  $\tilde{d}$ . Irrespective of the design for  $K_1$ ,  $K_2$  is the best controller that can be designed to estimate  $\tilde{d}$  since it makes the error with respect to  $\tilde{d}$  zero. The estimation error is given by,

$$e_d = \tilde{d} - \hat{\tilde{d}} = (1 - K_2 \tilde{G} S) \tilde{d} + K_2 S n. \quad (4.3)$$

Evidently, the application of  $K_2$  in (4.2) to (4.3) makes the error  $e_d$  with respect to  $\tilde{d}$  zero. Using  $\Psi = \frac{10000}{(s+100)^2}$  the bode plot of  $K_2$  is presented in Figure 4.2. The estimates of  $\tilde{d}$ ,

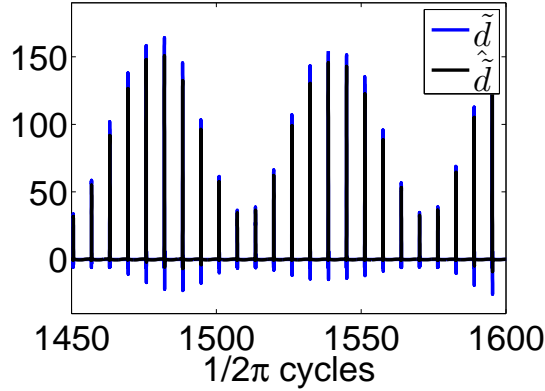


Figure 4.3: Performance of the force estimating controller  $K_2$  shown through estimates of the disturbance  $\tilde{d}$ , denoted by  $\hat{\tilde{d}}$ .

denoted by  $\hat{\tilde{d}}$ , are plotted against the cantilever oscillation cycles in Figure 4.3, which shows the performance of the estimating controller  $K_2$ . Several data points within each cycle of cantilever oscillation are required in order to obtain good estimates of the disturbance signal, which translates to the interaction forces. This calls for high-speed electronics and a much higher closed-loop bandwidth of the hardware system than is available in current commercial AFMs.

The estimation of the disturbance  $\tilde{d}$  gives us a direct estimate of the tip-sample interaction

force of the real cantilever subsystem. Since,

$$\tilde{d} = d - \hat{d},$$

and  $\hat{d}$  is a part of the mock system generated digitally,  $\tilde{d}$  can be reduced to estimates of  $d$ , which in turn represents  $F_{ts}(p_1 - h + v)$ . Therefore, the design of  $K_2$  facilitates the estimates of the tip-sample interaction forces. These estimates can be further fit with force models to compute the specific physical sample properties of interest.

## 4.2 Topography and Property Estimation

Force curves, which are plots of the interaction force against the tip-sample separation are used to obtain property estimates of the sample. Force modulation techniques were developed for samples with variations in local surface elasticity [36]. The variation in elasticity is measured by the changes in cantilever deflection under constant average force. In [37], the authors use a series of approach-retract force curves to obtain time series data of the cantilever response and thereby identify the cantilever transfer function. Here, small oscillation amplitudes are considered and the nonlinear tip-sample interaction force is assumed to be linearized and absorbed as a system internal parameter. Experiments in low damping environments have also been used to estimate the relationship between the cantilever frequency shift and the interaction potential [38]. Majority of these techniques utilize force curves taken at discrete locations on the sample quasi-statically and map them to physical properties. Although they are effective in estimating sample properties, they suffer from the disadvantages of long process time and limitations in the spatial/lateral resolution of the sample properties. Some other techniques like the contact-resonance AFM [39] estimate the visco-elastic properties of the sample without estimating the interaction forces, assuming a spring-dashpot tip-sample interaction model. The excitation of the cantilever at two frequencies (close to its natural frequency) in addition to oscillating it at resonance in tapping mode has been shown to estimate equivalent cantilever parameters at higher speeds than conventional techniques [40]. However, a simple model is assumed for the tip-sample

interaction.

Our high bandwidth imaging technique along with  $K_2$  provides dynamic estimates of the tip-sample force as against the static methods predominantly used to estimate sample properties. A brief discussion of the Hertz (short range repulsive force), DMT, JKR and Maugis models for inter-atomic forces between surfaces is presented to motivate the use of a generic force model. This generic model has been fit to the force estimates obtained through the design of  $K_2$ .

#### 4.2.1 Generic Force Model

Under the Hertz contact force model a frictionless contact without any forces of adhesion is assumed. It is appropriate for high normal loads or low surface forces. The force equations in the Hertz model are given by,

$$F_{ts} = \begin{cases} 0 & z_{ts} > 0 \\ \frac{4}{3}E^*\sqrt{R}(-z_{ts})^{\frac{3}{2}} & z_{ts} \leq 0 \end{cases}, \quad (4.4)$$

where  $R$  is the tip radius, and  $E^* = (\frac{(1-\nu_t^2)}{E_t} + \frac{(1-\nu_s^2)}{E_s})^{-1}$  is the effective Young's modulus of the tip and sample. Individual Young's moduli and Poisson's ratios are represented by  $E$  and  $\nu$ , with subscripts  $s$  and  $t$  referring to the sample and tip respectively.

DMT, JKR as well as the Maugis model are based off of the Hertz model with the addition of long range attractive Van der Waals forces. The JKR model [27] applies to highly adhesive systems with low stiffness and large tip radii, translating to compliant materials with strong adhesion properties and a blunt tip. It assumes a non-zero contact area at zero load. The contact radius at separation is modeled to be  $0.63a_0$ , where  $a_0$  is the intermolecular distance. This model predicts instability during approach and retraction of tip to or from a sample surface. During loading it models a neck forming between the tip or sample, contributing to hysteresis.

The DMT model constraints the tip-sample geometry to be Hertzian [4]. Finite stresses at contact perimeter and surface forces acting outside the contact region are considered. It

is best suited for rigid systems with small adhesion forces and sharp tips. The governing equations are given by,

$$F_{ts} = \begin{cases} \frac{-HR}{6z_{ts}^2} & z_{ts} > a_0 \\ \frac{-HR}{6a_0^2} + \frac{4}{3}E^*\sqrt{R}(a_0 - z_{ts})^{\frac{3}{2}} & z_{ts} \leq a_0 \end{cases}, \quad (4.5)$$

where  $H$  is the Hamaker's constant dependent on the materials in contact.

The Maugis model lies in the spectrum between JKR and DMT models in terms of adhesion force influence. A variable parameter  $\lambda$  is used to define the adhesion force influence in the model. When this  $\lambda = 0$  in Maugis model, it results in the Hertz model,  $\lambda < 0.1$  gives the DMT model and  $\lambda > 5$  results in the JKR model. The models described are often modified or additional terms are added depending on the operating conditions.

In our formulation for property estimation, these models are taken as a basis and a generic model is described as follows. The tip-sample interaction force in the attractive and repulsive regions,

$$F_{ts}(z_s) = \begin{cases} \alpha(a_0 - z_s)^m & z_s < 0 \\ \beta + \gamma(z_s)^n & z_s \geq 0 \end{cases}, \quad (4.6)$$

where  $\alpha$ ,  $\beta$  and  $\gamma$  are parameters governed by the properties of the interacting materials, and  $z_s = a_0 - z_{ts}$ , with  $a_0$  being the intermolecular distance and  $z_{ts}$  is the separation between probe-tip and sample. For instance, in case of the DMT model equations in (4.5),  $\alpha = \frac{-HR}{6}$ ,  $\beta = \frac{-HR}{6a_0^2}$ ,  $\gamma = \frac{4}{3}E\sqrt{R}$ , and  $m = -2$  and  $n = 3/2$ . This generic model will be employed in Section 4.2.3 where methods to derive estimates of sample physical properties are elucidated.

It is very important to note that the force models described here are merely used to develop a generic model that can be used to fit the force data with. The imaging mode measures the interaction forces which comprise all the properties of the sample. Therefore, the mode facilitates access to the most basic information available about the sample. Any property inferred from this data implies underlying assumptions inherent in the model used for interpreting the estimates.

### 4.2.2 Topography Estimates

As a next step, some relations are presented that enable the estimation of the sample topography from the estimate  $\hat{\tilde{d}}$ . The nonlinear force of the tip-sample interaction in terms of the separation between the tip and the sample is piecewise continuous and bounded for a practical range of separation distances. On application of mean value theorem the forcing term,

$$F(bp_1 - bh + bv) - F(b\hat{p}_1 - b\hat{h}) = \Theta(\tau)(b\tilde{p}_1 - bh - bv), \quad (4.7)$$

where  $\Theta = \frac{\partial F}{\partial z}$  with  $z$  lying between  $(bp_1 - bh + bv)$  and  $(b\hat{p}_1 - b\hat{h})$ . We can assume that the sample topography ( $h$ ) is approximately a constant over a period of cantilever oscillation and the integral of  $\tilde{p}_1$  is negligible owing to its small values. With these assumptions and  $v = 0$  we get,

$$\int_{T-\frac{2\pi}{\Omega}}^T [F(bp_1 - bh) - F(b\hat{p}_1)] d\tau = \int_{T-\frac{2\pi}{\Omega}}^T \Theta(\tau) d\tau (bh). \quad (4.8)$$

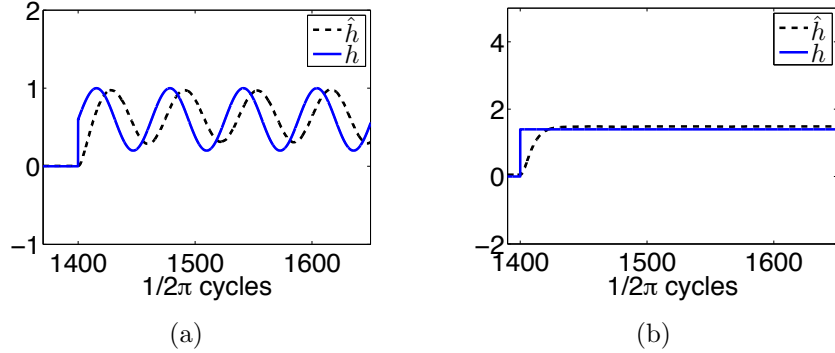


Figure 4.4: (a) and (b) show the estimates of a sinusoidal sample profile through the topography estimation. The blue lines indicate the sample profile considered while the dotted lines show the estimates.

Therefore, integration of the estimate  $\hat{\tilde{d}}$  over every period of cantilever oscillation, facilitates the estimation of the height signal  $h(\tau)$ . It may be noted that the  $z$ -piezo actuation signal  $v$  can be designed to keep  $\tilde{d}$  within the estimation bandwidth of  $K_2$ , but this is not analyzed in this paper.

It is important to note that all plots contain non-dimensionalized values unless otherwise

specified on their axes. In our simulations, a cantilever of natural frequency  $\omega_n = 69.578\text{kHz}$ , damping co-efficient  $\xi = 0.0033$  and mass  $m = 7.482 \times 10^{-12}\text{kg}$  is considered. Frequency  $\bar{\omega} = \omega_n$  and dither oscillation amplitude  $b = 2.916\text{nm}$  are used as normalization parameters wherever appropriate.

The interpretation of sample properties and topography from the interaction force estimates are significantly dependent on the physical interaction model chosen. In this section, sample topography estimates are obtained with the assumption of DMT model on the forces. The difference between the forces in the real and the mock system ( $d - \hat{d}$ ) is approximated by  $\Theta(\tilde{y} - h)$ , where  $\Theta$  is the averaged slope of the force with respect to deflection error over each cycle of cantilever oscillation. Using enough data points the unknowns,  $\Theta$  and  $h$ , the sample height profile are fit numerically. In this section, we pose a few scenarios as examples where we assume knowledge of one or more of the parameters involved in the generic interaction force model in (4.6) and propose schemes to fit the other unknowns. In the following discussion, the deflection (measured), also denoted by,  $p_1$  and the force estimate  $\hat{F}$ , which is  $\hat{\tilde{d}} + \hat{d}$  are always assumed to be known.

The estimated force difference signal is used to obtain an estimate of the height profile of the sample using the integrator operation described in (4.8).

The state of  $\dot{q} = u(T) - u(T - \frac{2\pi}{O})$  is equivalent to  $\int_{T-\frac{2\pi}{O}}^T u(\sigma) d\sigma$ . Using this relation, the integral  $\int_{T-\frac{2\pi}{O}}^T \hat{\tilde{d}}(\sigma) d\sigma$  is computed. From (4.8) if  $\hat{\tilde{d}}$  is a good enough estimate of  $\tilde{d}$ , then

$$\int_{T-\frac{2\pi}{O}}^T \hat{\tilde{d}}(\tau) d\tau \approx (\int_{T-\frac{2\pi}{O}}^T \Theta(\tau) d\tau)bh. \quad (4.9)$$

Furthermore, the integrated value of  $\Theta$  will be a constant over each cycle for the speeds of scanning considered. Consequently, the integrated values of  $\hat{\tilde{d}}$  are passed through a second order filter  $\frac{1}{(\tau_q s + 1)^2}$ . The value of  $\tau_q$  is chosen be less than  $\frac{1}{\omega_h/\bar{\omega}}$ , therefore, the filter retains frequency content of the sample topography, eliminating the high frequency components from  $p_1$  and  $\hat{p}_1$ . The filtered signals have the same frequency and proportional amplitude as  $h$ . The factor of proportionality is determined by observing the filtered signals over a few cycles and interpolating the value of the integral of  $\Theta$  over a cycle. This provides a estimate of the sample topography  $h$  as shown in Figure 4.4.

Since we use a filter of the form  $\frac{1}{(\tau_q s + 1)^2}$  in the estimation, the step function in the sample profile is not captured by the estimate  $\hat{h}$  and results in a phase difference from the original (see Figure 4.4). It must be noted that other methods to estimate the sample profile from the disturbance estimate  $\hat{d}$  are also considered. For instance, the estimate  $\hat{d}$  can be fitted to a force curve model such as the DMT model [4] to get estimates of  $h$ .

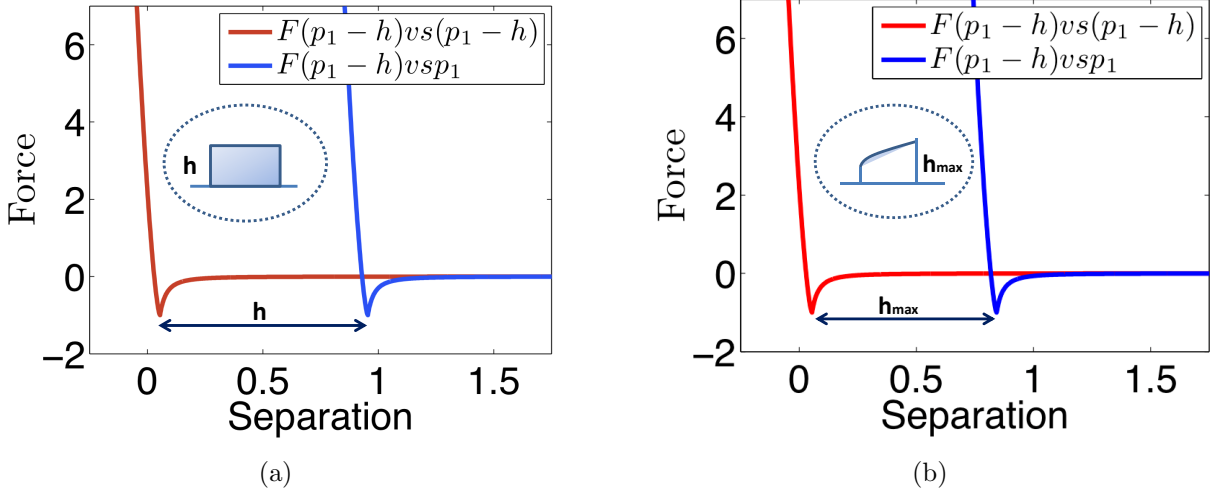


Figure 4.5: (a) and (b) The displacement of the alternate force curve against cantilever deflection from the actual force-displacement curve provides an estimate of the sample height. If the sample profile is constant over a few cantilever oscillation cycles, topographic measures can be done using the force estimates and the deflection data.

Ideally, the force curve is a plot of the interaction forces against the separation between the probe and sample surface, that is  $F(p_1 - h)$  vs  $(p_1 - h)$ . However, the probe-sample separation  $p_1 - h$  is not known since sample profile  $h$  is unknown. In our first attempt, we try to derive the properties of force-curve by analyzing the plot of force estimate  $\hat{F}(p_1 - h)$  vs the cantilever deflection  $p_1$  (see Figure 4.5(a)).

Note that the estimated force-curve plot  $F(p_1 - h)$  vs  $p_1 - h$  is a translated version of the force-estimate vs deflection plot  $\hat{F}(p_1 - h)$  vs  $p_1$ . A high bandwidth estimate of the interaction forces facilitates the estimation of sample topography by looking at the translated plots and averaging the translation over each or a few cantilever oscillation cycles where the sample profile  $h$  is approximately a constant. In typical force models as seen in Section 4.2.1, the

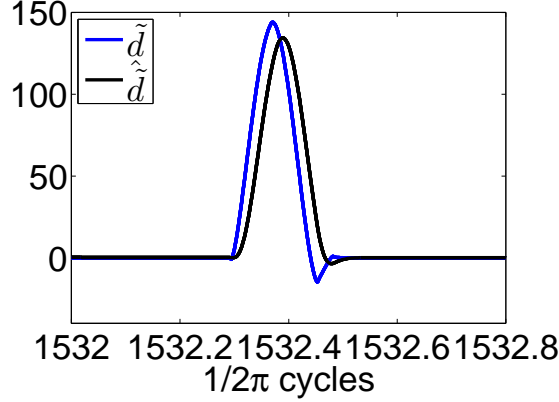


Figure 4.6: The plot of the estimate  $\hat{\tilde{d}}$  compared to original interaction force difference  $\tilde{d}$  is shown. The estimate is able to capture the repulsive force region well although with a phase lag. However, the attractive region is not captured well enough for a  $h$  of frequency equal to 10% of the cantilever resonance frequency.

repulsive tip-sample interaction force, denoted here by  $F_{ts}$  is given by,

$$F_{ts} = \beta + \gamma(z_s)^n, \quad (4.10)$$

where  $\beta$  and  $\gamma$  are parameters governed by the properties of the interacting materials, and  $z_s$  is a measure of separation between tip and sample. The repulsive forces are estimated well by the  $K_2$  design as shown in Fig.4.6

### 4.2.3 Property Estimates

The force estimates and the deflection data that are available can be used to obtain a high bandwidth sample property estimate. For this purpose, the generic force equation in (4.6) has been used. A few example cases are presented in this section to deduce sample properties following disturbance/force estimation.

The slope of the repulsive force can be estimated using the force estimate data, by plotting it against the deflection values measured (Figure 4.7(a)). The slope estimates over each cantilever oscillation cycle can provide dynamic estimates of the sample stiffness across a scan. For the next example, we assume the value of the exponent  $n$  in (4.10), which is  $\frac{3}{2}$  for the Hertz and the DMT models. Apart from  $n$  we assume no knowledge of the other tip or



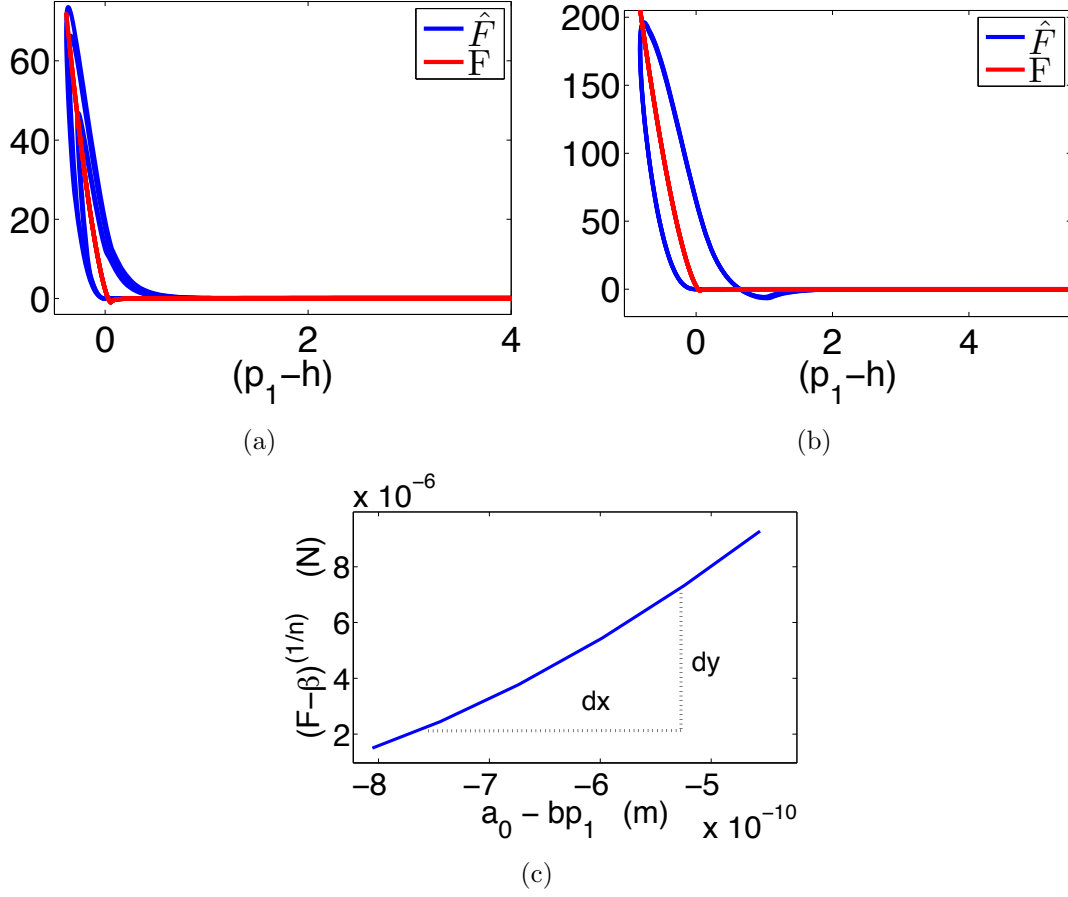


Figure 4.7: (a) The force  $F$  corresponds to the forcing term used in our simulations for the real system and  $\hat{F}$  corresponds to the estimate obtained. The phase lag in the estimate of  $\tilde{d}$  (Figure 4.6) is reflected in the plot of forces against the corresponding separations for sample. (b) shows the same for a constant sample surface. (c) The plot shows the left hand side of (4.11) plotted against the values of  $a_0 - p_1$  that are available through estimation and measurement. The slope of the plot corresponds to the value of  $\psi = \gamma^{2/3}$ .

sample properties. In this case, (4.10) can be re-written as,

$$\begin{aligned}
 (F_{ts} - \beta)^{2/3} &= (\gamma)^{2/3}(z_s), \\
 &= \psi(a_0 - p_1) + \psi(h),
 \end{aligned}
 \tag{4.11}$$

where we denote  $\gamma^{2/3}$  by  $\psi$ ,  $a_0$  is the intermolecular distance and the separation  $z_s = a_0 - p_1 - h$ . From (4.10), it is observed that the parameter  $\beta$  is the minimum value of the repulsive force with respect to the tip-sample separation distances. This can be computed numerically using the available interaction force estimate  $\hat{F} = \hat{\tilde{d}} - F(\hat{p}_1)$  within an error

of 5%. We consistently consider a set of force estimate values corresponding to the repulsive region where the tip interacts with the sample. These force estimates are plotted against the corresponding values of  $(a_0 - p_1)$ . Furthermore, the change in sample height  $h$  is negligible within the force region considered. Therefore, each of the aforementioned plots results in approximately a straight line, whose slope is an estimate of  $\psi$  from (4.11). The slopes may be averaged over several cycles to derive a reliable estimate for  $\psi$ . See Figure 4.7(c).

Other cases that can be explored are, deriving the sample's properties for a calibration sample or a sample with known sample height. This implies that an estimate of the entire  $z_s$  vector is available for use. In this case again the values of the intermolecular distance  $a_0$  and the adhesive force parameter  $\beta$  can be computed from the  $\hat{F}$  versus  $p_1$  plots. To fit the values of  $n$  and  $\gamma$ , we plot the vector containing  $\log(|F_{ts} - \beta|)$  against values of  $\log(|z_s|)$ . Please note that we have delineated only a few methodologies that can estimate the sample height and features, however other schemes remain to be explored.

### 4.3 Summary

A new signal  $\hat{d}$  was designed by enforcing a controller  $K_2$  to act upon the measured tracking error between system cantilever deflection and reference signal. This signal proved to be a good estimate of the extraneous disturbance signals that were rejected using robust control in Chapter 3. This in turn provided estimates of forces of tip-sample interaction. It is observed that since we obtain the disturbance estimates through the tracking error signal, property estimation is robust and is not significantly dependent on proper force regulation and its bandwidth

Some cases have been explored to estimate the sample height features and physical properties using this high bandwidth tip-sample interaction force estimates. The force from the sample occurs as an impulse at the frequency of cantilever oscillation, essentially every time the cantilever taps on the sample surface. The interaction force estimates are shown to capture the repulsive forces experienced by the tip well even at such high operating speeds ( $\approx 70$  kHz used in this chapter). Dynamic estimates of sample properties such as stiffness are obtained by fitting interaction models to the force estimate data. Identification of which

properties can be estimated robustly is dependent on the choice of model and experimental conditions.

# CHAPTER 5

## EXPERIMENTAL RESULTS

Preliminary experiments were conducted to validate performance of the controllers that have been verified through simulations. The issues confronted in the process of implementation and the results obtained are explained in this chapter. The roadblocks faced during attempts for in-air imaging are briefed in Section 5.1. Section 5.2. The controller design is revised for in-water imaging, and this is presented in Section 5.2.1 Also, differences in imaging in the two media are briefed. The experimental set up including the system transfer functions identified for in-water imaging case are explained in Section 5.2.2.

### 5.1 Imaging in Air: Issues

In the ideal case, experiments with tapping mode cantilevers with resonance frequencies in the order of 100 – 300 kHz would have been performed. The functional electronics in our lab does not accommodate operating in the closed-loop with data of such high frequency orders. Installing new FPGA-based electronics hardware and learning the programming know-how was not feasible in stipulated time.

While using AFM as a tool, there is no advantage to using a low frequency tip for dynamic mode imaging in air. The tapping mode cantilever market is gravitating towards mega Hertz resonance frequencies for reasons quoted in Section 1.2.1. Typically, contact mode cantilevers are the ones that lie in low frequency spectrum. However, the stiffness of these cantilevers are inadequate for scanning in air. This results in insufficient forcing and therefore spurious images while scanning.

During imaging, a fluid cell or water droplet can be used to immerse a contact mode cantilever and holder. Under water, the typical stiffness values of such cantilevers (0.15 –

0.35 N/m) render good images. Moreover, the resonance frequency of the cantilever shifts to a lower value ( $\approx \frac{1}{3}$  is the factor of reduction for water) when immersed in a fluid. This is accounted for by the viscosity of the fluid used [41]. The quality of the SiNi probes used for our experiments is not large, but with enough forcing good quality images were possible.

## 5.2 Imaging in Fluids: Proof of Concept

After consideration of options for low frequency operation in air, it was concluded that imaging in water was a good alternative. In this set up, frequencies that are within the capabilities of DSP hardware are possible in addition to rendering reliable and quality imaging. The objective is to demonstrate the validity of force regulation using deflection tracking (to a trajectory  $\hat{y}$ ) through disturbance rejection control. Before proceeding to the control design it is important to understand the behavior of the cantilever while imaging in water.

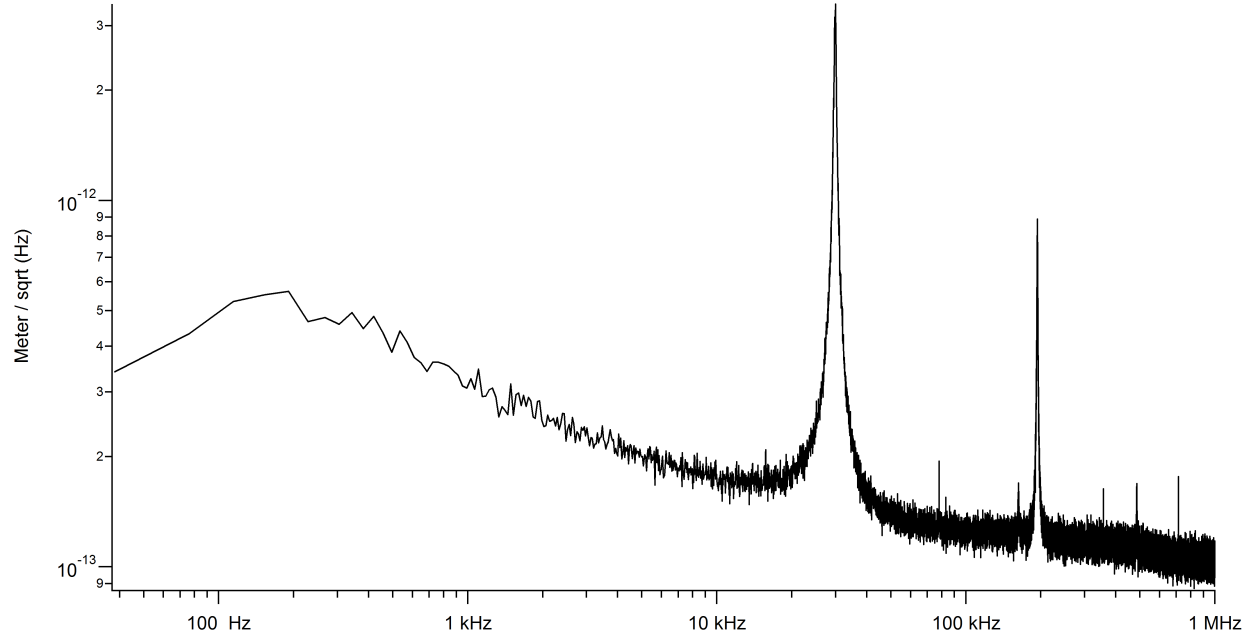
For the same cantilever, the properties in air and water differ considerably except for the stiffness that remains almost unchanged. Figure 5.1 shows the unforced thermal response for a cantilever of stiffness  $\approx 2$  N/m. The thermal response shows first natural frequency of this cantilever to be around 32 kHz when in air at a given temperature. The resonance frequency lowers by a factor of about  $\frac{1}{3}$  when placed in water, as shown in the thermal response in Figure 5.1(b). Furthermore, owing to increased damping (goes from 0.014 to 0.152 in for sample cantilever considered) the quality factor ( $Q$ ) decreases considerably.

The quality factor is defined by,

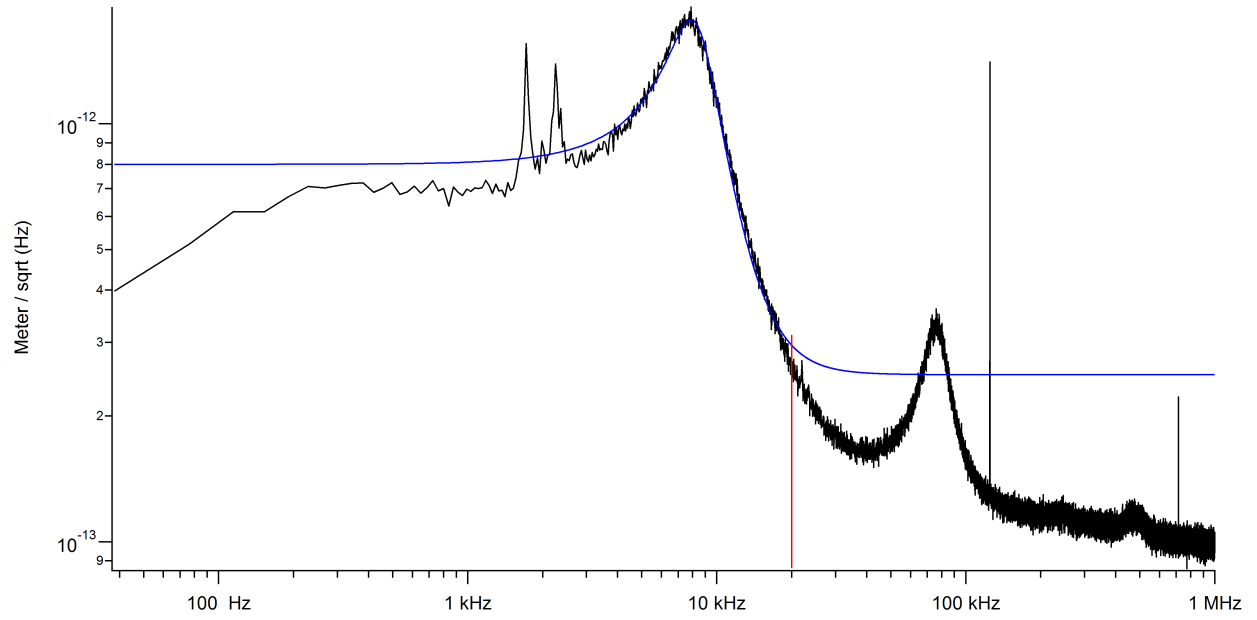
$$Q = \frac{\omega_n}{\Delta\omega},$$

where  $\Delta\omega$  is the half-power bandwidth i.e. the bandwidth over which the power of vibration is greater than half the power at the resonant frequency. This explains the broader peak of the cantilever response when used in water.

In order to determine the precise drive frequency of cantilever operation, a drive frequency sweep is performed by the shake piezo in a bandwidth around the resonant peak identified from the thermal response. For imaging in air, this peak is distinctly seen during the drive frequency sweep or tune process (see Figure 5.2(a)). It is observed that traditionally in

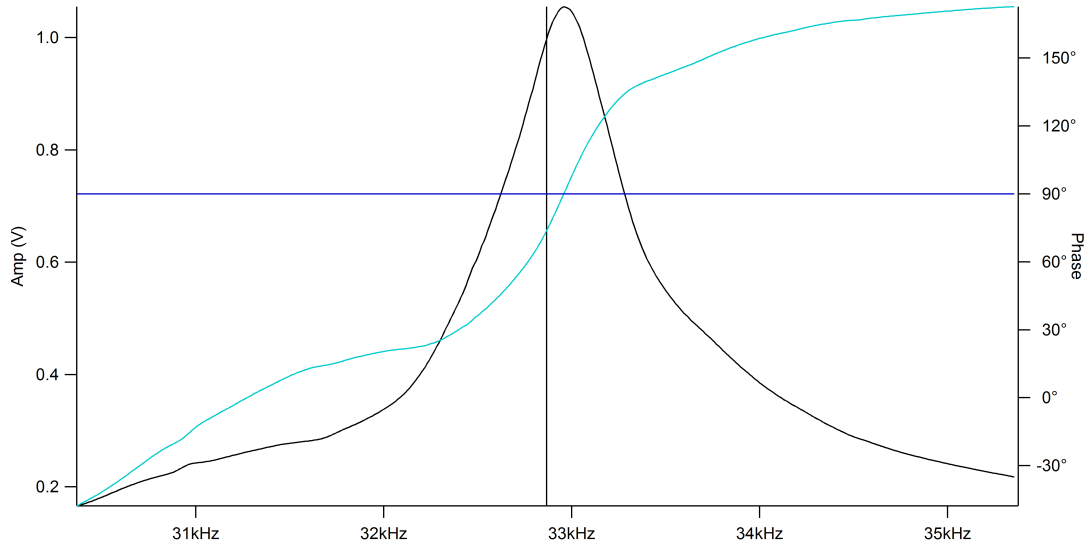


(a)

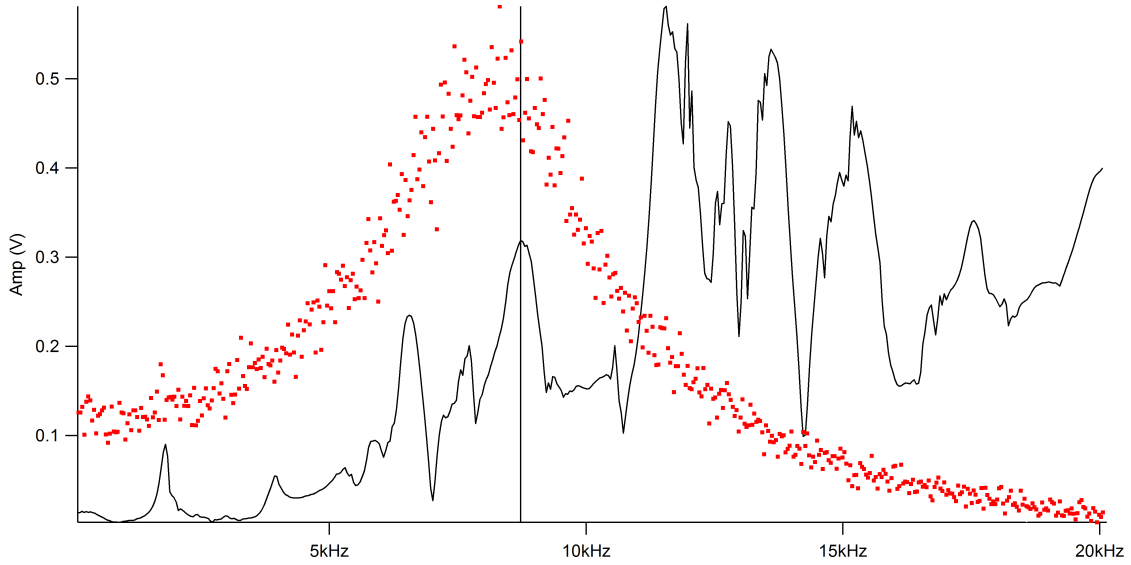


(b)

Figure 5.1: Comparison of unforced thermal responses for the same SiNi probe (a) in air and (b) immersed in water droplet. (a) shows the first resonance frequency of the cantilever at  $\approx 32$  kHz. (b) illustrates a fit to the cantilever near the lowered resonance frequency of  $\approx 8.7$  kHz, shown in blue line.



(a)



(b)

Figure 5.2: Comparison of cantilever tune graphs with dither forcing for the same SiNi probe. (a) The drive amplitude in Volts to achieve a target of 1 V in air was  $\approx 850$  mV. The fundamental resonant peak is distinctly captured as seen and the teal line illustrates the phase. The vertical black line indicates the set drive frequency which is 95% of the first modal frequency in the tune displayed. (b) When the tip and holder are immersed in water droplet a forest of peaks appear due to resonant cavity effect. A drive amplitude of  $\approx 1.98$  V was required to achieve a target amplitude of 0.3 V at the chosen drive frequency. The plot in red is the thermal response of the cantilever, which helps choose the proper resonance peak.

Mfp3D machines the shake piezo while performing the sweep oscillates the entire cantilever holder. This in turn sloshes the fluid between the probe and sample, termed a 'resonant cavity', and presents a forest of peaks in the drive frequency sweep. Often distinguishing the fundamental resonant peak from a resonant cavity peak becomes difficult. Picking the wrong peak can compromise image quality. In order to keep this error minimal the thermal response is superimposed on the tune curve as shown in Figure 5.2(b), and the most pronounced peak in the region of the fundamental resonance from thermal response is chosen. This is indicated by the vertical black line in Figure 5.2(b).

Cantilever properties comparison			
	Air	Water	Units
Resonance frequency $\omega_n$	69.8	8.74	kHz
Stiffness $k$	1.43	0.19	N/m
Quality factor $Q$	150	5	-
Damping coefficient $\zeta$	0.0033	0.159	-
invOLS	397	119	nm/V

Table 5.1: Comparison of typical cantilever properties of a tapping mode cantilever (AC240TS from Olympus) and the low frequency cantilever used in water (SiNi tips from BudgetSensors). The values in the table correspond to one sample cantilever from each category and are representative of the general behavior. The properties listed for the cantilever in water have been used for simulations in Section 5.2.1.

### 5.2.1 Control Design

The conventions followed in Section 3.4 are used for the control design in this section. The closed loop transfer functions, sensitivity function  $S$  and complementary sensitivity function  $T$  are designed using appropriate weighting functions. This provides the design for the controller  $K_1$  for a specific cantilever transfer function,  $G_c$ . The cantilever transfer function in our simulations is of the form,

$$G_c = \frac{-9.171e007}{s^2 + 1.749e004s + 3.017e009}.$$

The cantilever used for simulations has a resonance frequency of 8.7426 kHz and damping of 0.159 which is captured by the cantilever model  $G_c$ . These properties were identified using



a sample cantilever. Using the model for  $G_c$  the controller  $K_1$  is designed with the control objectives listed in Section 3.4.1. The control design follows the details in Section 3.4. Therefore, illustrations of the designed transfer functions are alone provided here. The characteristics of weighting functions  $W_s$  and  $W_t$  are shown in Figure 5.3. The resultant closed-loop transfer functions  $S$  and  $T$  are shown with respect to the weights  $1/W_s$  and  $1/W_t$  respectively in Figures 5.4 and 5.5. The closed-loop transfer function  $K_1S$  shown in Figure 5.6 demonstrates the performance of the designed minimal controller  $K_1$  given by,

$$K_1 = \frac{1.231s^3 + 536.8s^2 + 171.6s + 533.9}{s^3 + 8.87s^2 + 17.13s + 0.8319}.$$

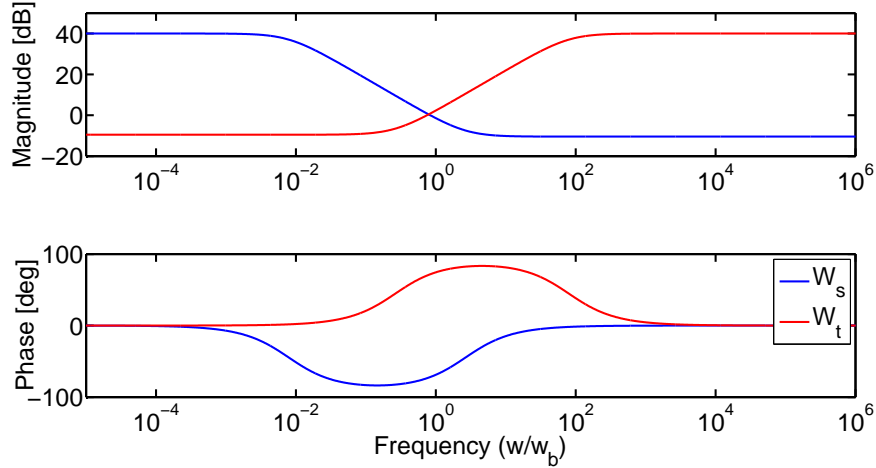


Figure 5.3: Weighting functions  $W_s$  and  $W_t$  used for the design of closed-loop functions  $S$  and  $T$  for imaging in water.

### 5.2.2 System Identification

It has been established that the cantilever dynamics are largely different while scanning in water. The system transfer functions corresponding to the actuating piezos (shake and vertical) were identified using conventional sine sweep inputs. The input and output frequency data were collected from a digital signal analyzer and transfer functions were fit to this data on Matlab. Figure 5.7 shows the transfer function from the vertical piezo input, denoted by

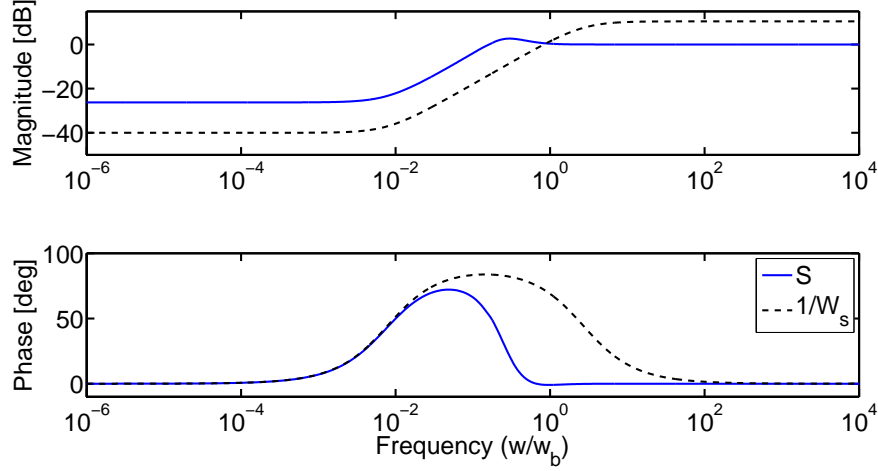


Figure 5.4: Design of the sensitivity transfer function  $S$  with  $G_c$  transfer function for in-water imaging.

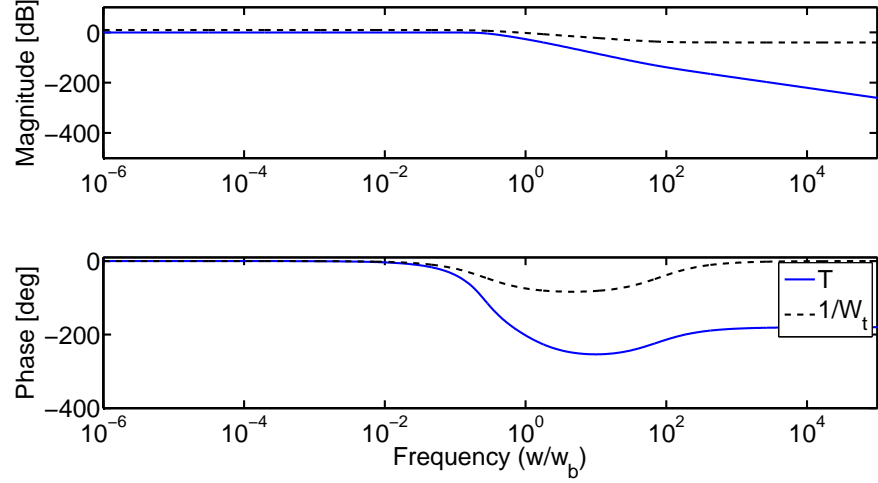


Figure 5.5: Design of the complementary sensitivity transfer function  $T$  with  $G_c$  transfer function for in-water imaging.

$u_z$  in Chapter 2, to the cantilever deflection signal  $y_m$  collected by the photo-sensitive diode sensor. The transfer function from the shake piezo input, denoted by  $u_d$ , to the cantilever deflection is shown in Figure 5.8. The data and the corresponding fit show that the dither piezo is predominantly active only beyond a frequency of 3 kHz. Therefore, the control effort cannot be directed entirely through the dither piezo. The following relation is used to design

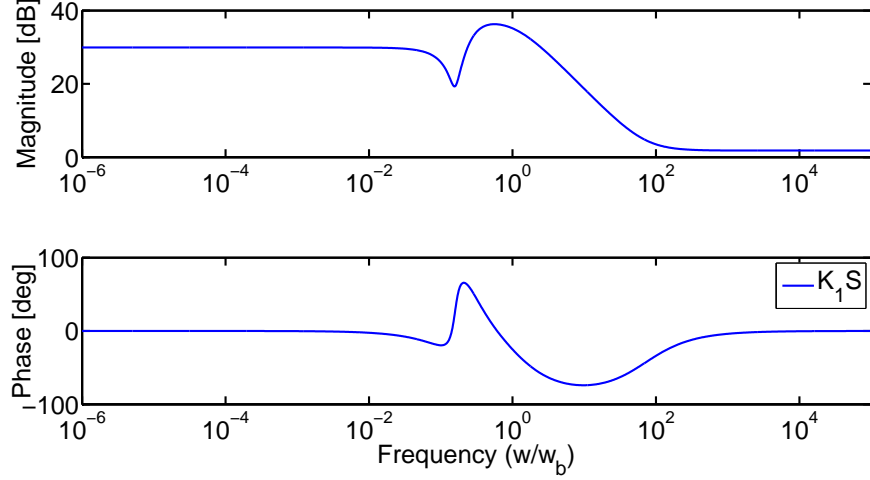


Figure 5.6: Designed closed-loop transfer function  $K_1S$  with  $G_c$  transfer function for in-water imaging.

$u_z$  and  $u_d$  from the designed control signal  $u_2$  according to the framework in Figure 3.4.

$$\begin{aligned} G_c u_2 &= G_{zc} u_z + G_{dc} u_d \\ u_2 &= G_c^{-1} G_{zc} u_z + G_c^{-1} G_{dc} u_d \end{aligned} \quad (5.1)$$

It is inferred that designing, the  $z$  piezo input

$$u_z = G_{zc}^{-1} G_c W_1 u_2, \quad (5.2)$$

and the dither piezo input

$$u_d = G_{dc}^{-1} G_c (1 - W_1) u_2, \quad (5.3)$$

satisfies (5.1). The weighting transfer function  $W_1$  is chosen to be low pass with a cut-off of 3 kHz, such that  $u_z$  handles the lower frequency actuation and the dither piezo is responsible for the higher frequencies. The weight  $W_1$  was chosen to be,

$$W_1 = \frac{1}{5.305 \times 10^{-5} s + 1}.$$

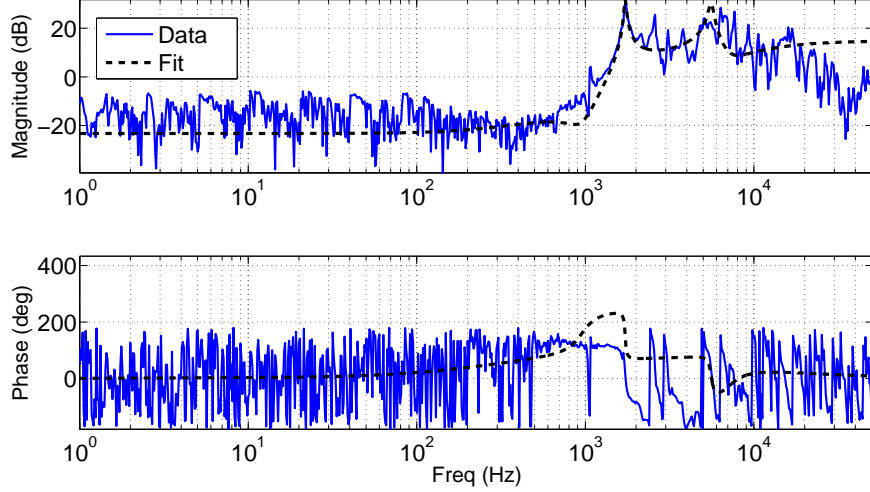


Figure 5.7: The transfer function,  $G_{zc}$ , identified between the  $z$  piezo input  $u_z$  and cantilever deflection  $y$ . The piezo was set at a DC offset of 70 V, the middle of its total range. A cantilever submerged in water with an effective resonance of 8.65 kHz was used in this identification experiment. The dotted black line is frequency response of the minimal transfer function fit numerically to the identification data collected. It is important that we have a good fit in the lower frequencies where  $u_z$  will take the maximum load of control.

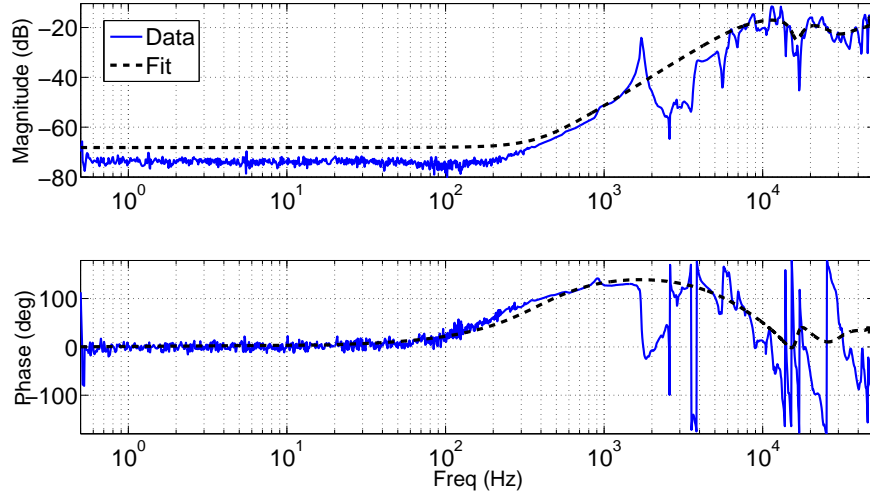


Figure 5.8: The transfer function,  $G_{dc}$ , identified between the dither piezo input  $u_d$  and cantilever deflection  $y$ . A cantilever submerged in water with an effective resonance of 8.65 kHz was used in this identification experiment. The dotted black line is frequency response of minimal transfer function fit numerically to the identification data collected.

The redefined controller is provided by the relation,

$$Q_1 = \begin{bmatrix} G_{zc}^{-1} G_c W_1 K_1 \\ G_{dc}^{-1} G_c (1 - W_1) K_1 \end{bmatrix}, \quad (5.4)$$

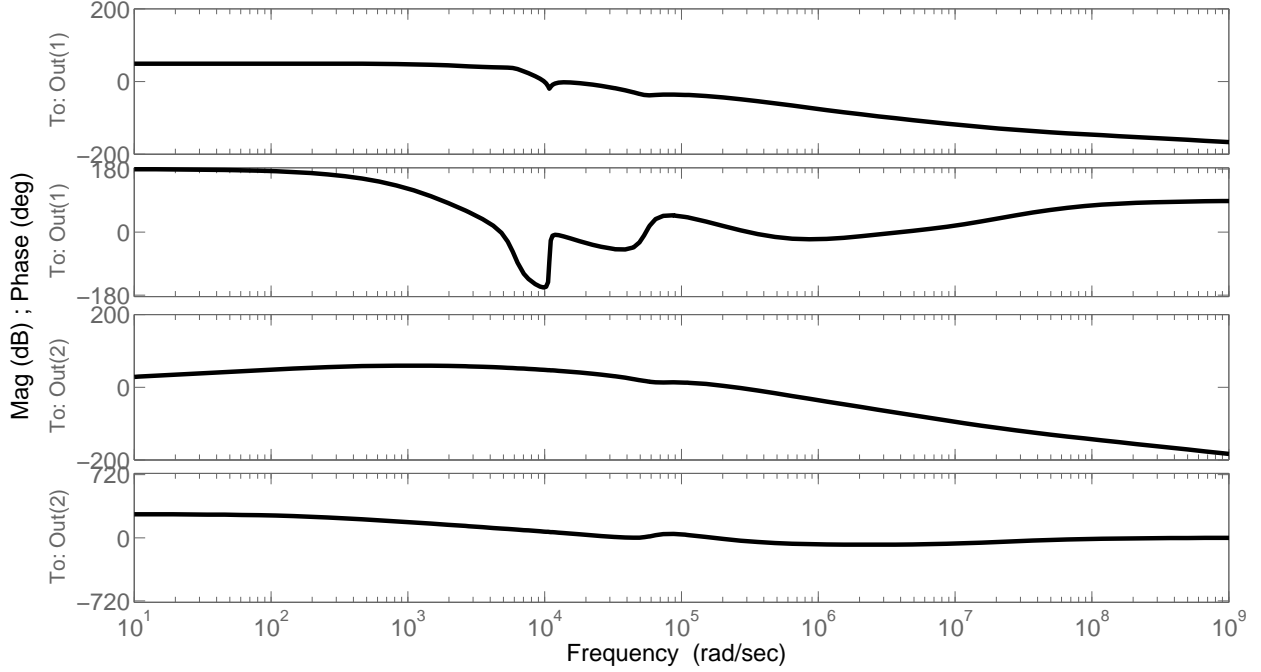


Figure 5.9: Frequency response of the transfer function  $Q_1$  in (5.4).  $Q_1$  is the system model from  $e_m$  to  $u_z$  (shown as Out(1)) and  $u_d$  (shown as Out(2)).

which takes  $e_m$  the measured error between the cantilever deflection  $y$  and the reference trajectory  $\hat{y}$  and outputs the control inputs  $u_z$  and  $u_d$  for the two driving piezos. The frequency response for  $Q_1$  is illustrated in Figure 5.9, where Out(1) denotes  $u_z$  and Out(2) denotes  $u_d$ . It is necessary to note that there is no non-dimensionalization during implementation. It was merely used as a technique to make the numerical computations and analysis more convenient.

The identified transfer function  $G_z$  between  $z$  piezo input  $u_z$  and output  $v$  is used to verify the cantilever model by using  $G_z^{-1}G_{zc}$ . The frequency response of  $G_z$  identified is shown in Figure 5.10.

### 5.2.3 Experiment Setup

An integrated Digital Signal Processing (DSP) board with on-board analog-digital (A/D) and digital-analog (D/A) conversion interfaces was used. The model of the board used is P25m from Innovative Integration that is mounted with a TI C6713 DSP chip. Figure 5.11 shows the experimental arrangement used with respect to the AFM.

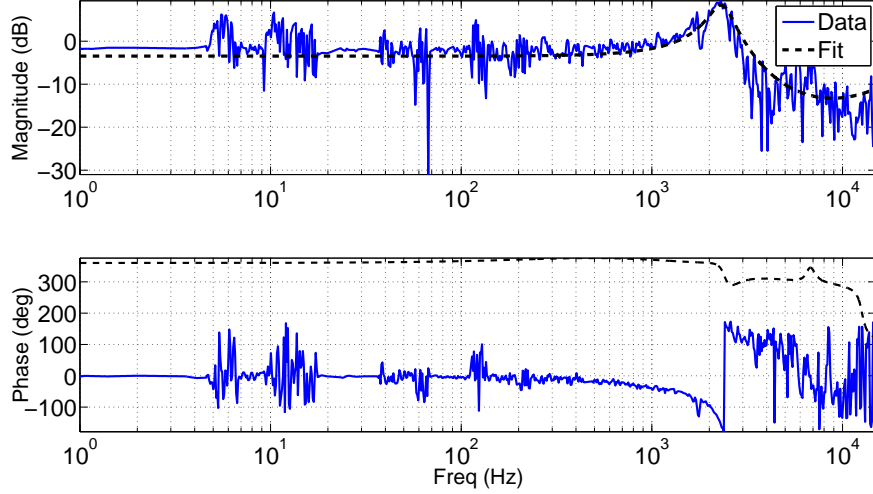


Figure 5.10: The transfer function,  $G_z$ , identified between the  $z$  piezo input  $u_z$  and output  $v$ . The piezo was set at a DC offset of 70 V, the middle of its total range. A digital signal analyzer was used for system identification giving sine sweep inputs to the system. The black dotted line shows frequency response of numerical transfer function fit obtained.

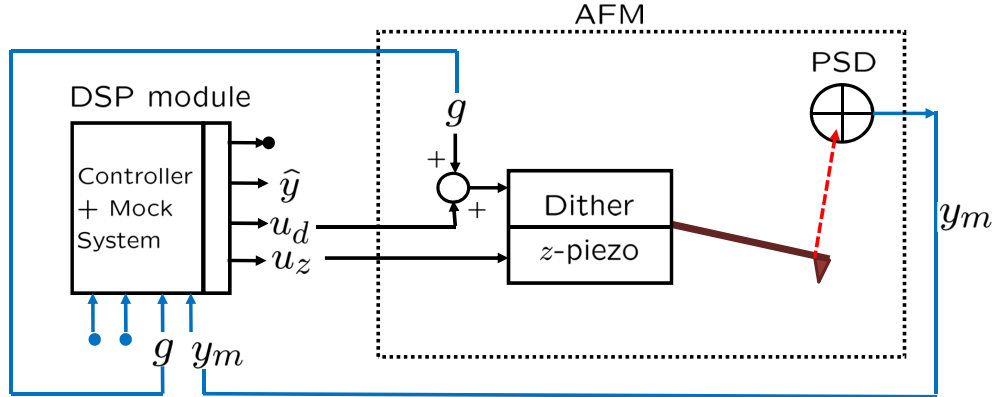


Figure 5.11: Closed-loop experimental arrangement featuring the Digital Signal Processing board complete with A/D and D/A components.

The sequence of the experiment is as follows. Upon identifying the cantilever transfer function and engaging it onto the sample surface using proportional-integral control, the raster scan in the lateral direction is begun. The cantilever deflection denoted by  $y_m$  and the sinusoidal signal  $g$  of the form  $g_0 \cos \omega t$  used to actuate the dither or shake piezo are drawn from the AFM system to the DSP's analog inputs. The DSP chip runs the controller dynamics as well as the mock system dynamics in tandem. Subsequently, the control inputs for the  $z$  and dither piezo are computed and mapped to the D/A ports of the DSP board. Thus

the closed-loop operation is completed. The reference trajectory  $\hat{y}$  generated by the mock system dynamics on the DSP and the cantilever deflection signal from PSD are collected to obtain the tracking error signal, which can then be used for disturbance/force estimation. However, it must be noted that a very high sampling rate of closed loop operation is required to robustly deduce the force and sample properties from the error data.

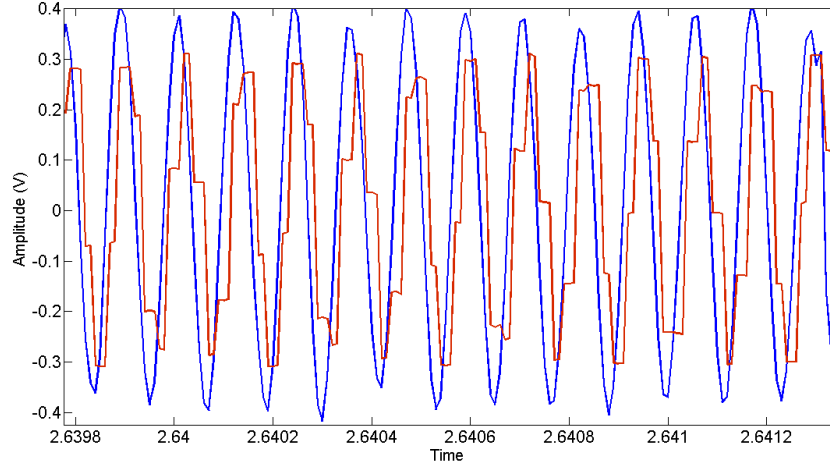


Figure 5.12: Comparison of cantilever deflection ( $y$  in blue) and reference trajectory ( $\hat{y}$  in red) in current experimental set up at 40 kHz sampling. The poor sampling is evident from the  $\hat{y}$  illustration.

With the current DSP hardware setup, the maximum achievable sampling rate was found to be 40-45 kHz. As a consequence, for a cantilever resonance frequency in the range of  $\approx 8.7$  kHz only about four points are sampled every cycle of oscillation. Owing to the lacking in hardware, it was not feasible to incorporate the modeled interaction force term  $\hat{d}$  in the mock system on the DSP module. The absence of  $\hat{d}$  implies that the disturbance encountered in the experiment is higher than what the controller was modeled for, i.e. the disturbance is now  $d$  (tip-sample interaction force) in place of  $d - \hat{d}$ . These factors result in a large initial mismatch between the cantilever deflection  $y$  and the reference trajectory  $\hat{y}$ . Furthermore, the resonant cavity owing to oscillation of the cantilever holder in water induces uncertainties in the model. Therefore, the regulation accomplished under available experimental conditions was not as expected from the simulations (see Figure 5.12). However, higher scanning rates will resolve most of these issues and is indispensable to effectively demonstrate this experiment.

### 5.3 Summary

Experimental validation with available hardware was not feasible for in-air imaging with typical tapping mode cantilevers. Efforts to develop in-house FPGA-based hardware were not successful. Therefore, a proof of concept experiment was designed where the imaging was performed in water in order to reduce the natural frequency of the cantilever and thereby the frequency of the signals to be handled by the controller. Redesign of control parameters, and issues encountered in this experiment with the current DSP-based hardware arrangement have been discussed along with the results achievable. Higher speed electronics will alleviate most of the problems faced and facilitate imaging in air, which can prove the efficacy of the designed controller better.



# CHAPTER 6

## CONCLUSION

### 6.1 Summary and Analysis

Atomic force microscopes are at the cutting edge of nanotechnology. However, considerable challenges need to be met to realize their full potential. A major setback arises from the low bandwidth of imaging in AFMs. In particular, it is a drawback while studying processes and properties of biological specimens that have variations spatially and temporally. Work done in order to address the problem of low bandwidth in the AFM community predominantly comprises of hardware design and alterations with least emphasis on control-system tools.

This dissertation has devised a new dynamic mode for AFMs that will facilitate high-speed imaging without the frills of major hardware fabrication. The mode makes extensive use of system tools. The salient features of the proposed imaging mode are:

- The control design that drives the imaging is model-based and therefore makes use of the system characteristics effectively.
- Amplitude modulation fails when the time scale separation between lateral positioning bandwidth and cantilever resonance frequency varies only by a small factor. The “fast” deflection signal of the cantilever is used instead of the traditionally used amplitude signal for force regulation.
- The cantilever deflection is controlled to track a “deflection-like” signal produced by a fictitious system that is analogous to the cantilever dynamics, except it is assumed that the sample input to the fictitious system is constant.
- The non-linearity in the system model coming from the tip-sample interaction force

is modeled as a disturbance enabling linear control design. Robust control design for force regulation through disturbance rejection has been performed. Notably, the regulation action does not affect the property estimates obtained through the imaging mode since the estimation procedures make use of the error from tracking. Regulation ensures that the tip stays close enough to the sample surface.

- The designs were all performed using the cantilever dynamic model  $G_c$ . It is important to note that the control designs could have been done for the transfer function given by  $\begin{bmatrix} G_{zc} & G_{dc} \end{bmatrix}^T$ .
- This enables consequent estimation of the disturbance through an appropriately designed signal. Disturbance estimates translate to interaction force estimate, which is the most informative/fundamental data that can be obtained from an imaging experiment.
- The interaction forces are functions of tip-sample separation (which changes in the presence of sample features) and its properties. Therefore, by suitably fitting models to the force data, sample topography as well as physical properties such as elasticity, hardness can be estimated and this has been demonstrated.
- Experimental validation of the new imaging mode by deploying it on a low resonance frequency cantilever in the available commercial AFM system was carried out.

## 6.2 Future Research Directions

The following points outlines how the scope of this dissertation can be extended to future work.

- Alternate approaches for control design such as nonlinear control design using Lyapunov functions and use of S-procedure need to be further explored. These possible approaches have been briefed in Appendix A and B.

- Considering the fact that existing dynamic modes of AFM operation use derivatives of the deflection signal such as amplitude for regulation, the implementation hardware in current modules have low sampling rates (10 – 100kHz). Whereas, the proposed imaging mode effects force regulation using the fast deflection signal whose frequency is in the order of 100 – 300kHz. Validation experiments at proportionally scaled lower frequencies could only be used to demonstrate force regulation owing to the limitations of DSP operating bandwidths.
- The high frequency cantilever oscillation necessitates sampling rates of a few MHz (3-10MHz). FPGA based boards that can take in and give out data over four channels with a closed-loop frequency of a few MHz are available. Developing a FPGA based hardware setup that can realize the required high closed-loop frequencies (in  $x$  and  $z$  directions) is being pursued. While using actual tapping mode cantilevers and high bandwidth computational power in the closed-loop video-rate imaging can be effected.
- Additionally, a high bandwidth nanopositioning system is required to demonstrate the effects of our idea. The FPGA based hardware may be used to provide inputs to the higher bandwidth lateral positioning system. The control designs demonstrated in [6] can be used to obtain further lateral bandwidth improvements in conjunction with the fast imaging.
- This dissertation has illustrated some ways to estimate sample properties from the force estimate but these are not exhaustive. Characterization of relation between robustness of estimates and force model employed should be explored.

# APPENDIX A

## ALTERNATE APPROACHES

### A.1 BACKSTEPPING

In this section, cantilever model analogous to the one in Section 3.1 is considered for the most part with certain modifications that are explained. Prior to using the disturbance rejection approach, nonlinear control design considerations were made. These are briefed in this section of the appendix.

Backstepping approach is commonly used to design stabilizing control for systems with nonlinear dynamics. Equations of the form,

$$\begin{aligned}\dot{X} &= f_x(X) + g_x(X), \psi \\ \dot{\psi} &= f_\psi(X, \psi) + g_\psi u_1,\end{aligned}\tag{A.1}$$

constitute the structure of this approach. Here,  $X \in \mathbf{R}^n$ ,  $n \geq 1$ ,  $\psi$  is typically a scalar,  $u_1$  is the scalar input to the system and the functions denoted by  $f$ 's become zero at the origin.

In the first case, a control signal  $u_2$  in addition to vertical actuation  $v$  is considered. Based on backstepping approach the vertical actuation signal  $v$  is modeled to be derived from a dynamical system as explained in the following. This is done in order to pull  $v$  out of the nonlinear function term  $F$ .

The cantilever dynamic equations are given by,

$$\frac{d^2 \bar{p}}{dt^2} + 2\zeta\omega_n \frac{d\bar{p}}{dt} + \omega_n^2 \bar{p} = u_d + \frac{1}{m} F(p_1 - h - v).\tag{A.2}$$

Here,  $u_d = b\omega_n^2 \cos(\omega t) + b\omega_n^2 \bar{u}_2(t)$ , i.e. in addition to the generic dither input  $b\omega_n^2 \cos(\omega t)$ , we consider an additional input,  $b\omega_n^2 \bar{u}_2(t)$ .

In the non-dimensionalized co-ordinates let  $\tau = \omega t$ ,  $(\cdot) = \frac{d}{d\tau}(\cdot)$ ,  $p = \bar{p}/b$ ,  $h = \bar{h}/b$ ,  $v = \bar{v}/b$ ,  $\Omega_n = \omega_n/\bar{\omega}$ ,  $\Omega = \omega/\bar{\omega}$ ,  $F_0 = m\bar{\omega}^2 b$ ,  $u_2(\tau) = \bar{u}_2(\tau/\bar{\omega})$ . And we define the states  $p_1 = p$  and  $p_2 = \dot{p}$ . Then the ODE in terms of  $p_1$  and  $p_2$  becomes,

$$\dot{p}_1 = p_2, \quad (\text{A.3})$$

$$\dot{p}_2 = -\Omega_n^2 p_1 - 2\zeta\Omega_n p_2 + \Omega_n^2 \cos(\Omega\tau) + u_2 + \frac{1}{F_0} F(bp_1 - bh - bv) \quad (\text{A.4})$$

We also assume that the vertical actuation signal  $v$  is the output of the actuator dynamics,

$$\dot{\xi} = A_f \xi + B_f u_1, \quad (\text{A.5})$$

$$v = C_f \xi, \quad (\text{A.6})$$

where  $A_f$ ,  $B_f$  and  $C_f$  matrices are representative of the modeled actuator dynamics. The signal  $u_1$  is the input to this actuator and  $\xi$  denotes the state of the system.

Following this a mock system similar to the one in Section 3.2 is defined as follows,

$$\dot{\hat{p}}_1 = \hat{p}_2, \quad (\text{A.7})$$

$$\dot{\hat{p}}_2 = -\Omega_n^2 \hat{p}_1 - 2\zeta\Omega_n \hat{p}_2 + \Omega_n^2 \cos(\Omega\tau) + \frac{1}{F_0} F(b\hat{p}_1), \quad (\text{A.8})$$

$$\hat{y} = \hat{p}_1, \quad (\text{A.9})$$

where  $\hat{y}$  describes the modeled mock system's output.

Let the error  $\tilde{p}_1$  be defined by  $p_1 - \hat{p}_1$ , and  $\tilde{p}_2 = p_2 - \hat{p}_2$ . The error dynamic equations become,

$$\tilde{p} = A\tilde{p} + Bu_2 + B\frac{1}{F_0}[F(bp_1 - bh - bv) - F(b\hat{p}_1)], \quad (\text{A.10})$$

where  $A = \begin{bmatrix} 0 & 1 \\ -\Omega_n^2 & -2\zeta\Omega_n \end{bmatrix}$ ,  $B = \begin{bmatrix} 0 \\ 1 \end{bmatrix}$ . The control signal  $u_2$  is chosen to be,

$$\begin{aligned} u_2 &= K\tilde{p} + u_{2x} + C_1(\tilde{p}_1 - v), \\ &= K\tilde{p} + u_{2x} + C_1(\tilde{p}_1 - C_f \xi). \end{aligned} \quad (\text{A.11})$$

Mean value theorem is applied to the force term  $F$  in the error dynamic equations (A.10) ,

$$\dot{\tilde{p}} = A\tilde{p} + BK\tilde{p} + Bu_{2x} + BC_1(\tilde{p}_1 - v) + B\Theta\frac{1}{F_0}(b\tilde{p}_1 - bv - bh) \quad (\text{A.12})$$

$$= (A + BK)\tilde{p} + Bu_{2x} + B(C_1 + \Theta\frac{1}{F_0})(b\tilde{p}_1 - bv) - \Theta\frac{1}{F_0}Bbh. \quad (\text{A.13})$$

The term  $(A + BK)^T P + P(A + BK)$  is assumed equal to  $-Q$  with  $Q > 0$  by design. The following Lyapunov energy function is chosen,

$$V(\tilde{p}) = \tilde{p}^T P \tilde{p} \quad (\text{A.14})$$

where matrix  $P$  is positive-definite. The derivative of the energy function yields,

$$\dot{V} = -\tilde{p}^T Q \tilde{p} + 2\tilde{p}^T P B u_{2x} + 2\tilde{p}^T P B (C_1 + \frac{1}{F_0}\Theta)[b\tilde{p}_1 - bv - \frac{\Theta b h}{C_1 + \Theta}], \quad (\text{A.15})$$

where  $\Theta = \frac{\partial f}{\partial z}(\bar{z})$  and  $\bar{z}$  lies in  $[bp_1 - bv - bh, b\hat{p}_1]$ . The variables  $K$ ,  $P$ ,  $C_1$ ,  $v$  and  $u_{2x}$  are free to be designed. However, this approach not only calls for nonlinear control design but imposes that a model of the interaction forces be known. The force model is required for computation of the slope term  $\Theta$ , which varies temporally.

Alternately, the following design could be considered,

$$\dot{p}_1 = p_2, \quad (\text{A.16})$$

$$\dot{p}_2 = -\Omega_n^2 p_1 - 2\zeta\Omega_n p_2 + \Omega_n^2 \cos(\Omega\tau) + \frac{1}{F_0}F_{ts}(bp_1 - bC_f\xi), \quad (\text{A.17})$$

$$\dot{\xi} = A_f\xi + B_f(h + v), \quad (\text{A.18})$$

$$\bar{h} + \bar{v} = C_f\xi, \quad (\text{A.19})$$

where the inputs  $h$  and  $v$  are both modeled to be raw inputs of the filter  $\xi$ . Output of filter represents the nature of sample profile signal in real samples. The state space vector  $x$  is defined as  $[p_1 \ p_2 \ \xi]^T$ . The complete system in terms of the state space co-ordinates is defined by

$$\dot{x} = Ax + B_d \cos(\Omega\tau) + B(h + v) + B_{ts}F_{ts}(C_{ts}x), \text{ where } A = \begin{bmatrix} 0 & 1 & 0 \\ -\Omega_n^2 & -2\zeta\Omega_n & 0 \\ 0 & 0 & A_f \end{bmatrix},$$

$$B_d = \begin{bmatrix} 0 \\ \Omega_n^2 \\ 0 \end{bmatrix}, B = \begin{bmatrix} 0 \\ 0 \\ B_f \end{bmatrix}, B_{ts} = \begin{bmatrix} 0 \\ \frac{1}{F_0} \\ 0 \end{bmatrix} \text{ and } C_{ts} = \begin{bmatrix} b & 0 & -bC_f \end{bmatrix}.$$

A mock system appended with an observer  $LC$  is modeled and the mock dynamics and error dynamics for error  $\tilde{x} = x - \hat{x}$  are,

$$\dot{\tilde{x}} = A\hat{x} + B_d \cos(\Omega\tau) + B_{ts}F_{ts}(C_{ts}\hat{x}) - LC(x - \hat{x}), \quad (\text{A.20})$$

$$\dot{\tilde{x}} = (A + LC)\tilde{x} + B(h + v) + B_{ts}C_{ts}\tilde{x}\frac{\partial F_{ts}}{\partial z}. \quad (\text{A.21})$$

The Lyapunov energy function  $V(\tilde{x}) = \tilde{x}^T P \tilde{x}$  is considered. Taking time derivative of  $V$  renders the relations,

$$\begin{aligned} \dot{V} &= \tilde{x}^T P [A_L \tilde{x} + B_{ts} C_{ts} \Theta \tilde{x} + B(h + v)] + [A_L \tilde{x} + B_{ts} C_{ts} \Theta \tilde{x} + B(h + v)]^T P \tilde{x}, \\ &= \tilde{x}^T [A_L^T P + P A_L] \tilde{x} + 2\tilde{x}^T P B_{ts} \Theta C_{ts} \tilde{x} + 2\tilde{x}^T P B(h + v), \\ &\leq \tilde{x}^T [A_L^T P + P A_L] \tilde{x} + 2\tilde{x}^T P B_{ts} \Theta C_{ts} \tilde{x} + 2\tilde{x}^T P B(h + v), \\ &\quad - 2\eta(\Theta + K) C_{ts} \tilde{x} (\Theta - K) C_{ts} \tilde{x}, \\ &= \tilde{x}^T [A_L^T P + P A_L] \tilde{x} + 2\tilde{x}^T P B_{ts} \Theta C_{ts} \tilde{x} + 2\tilde{x}^T P B(h + v), \\ &\quad - 2\eta((\Theta C_{ts} \tilde{x})^2 - (K C_{ts} \tilde{x})^2), \\ &= \begin{bmatrix} \tilde{x} \\ \Theta C_{ts} \tilde{x} \end{bmatrix}^T \begin{bmatrix} A_L^T P + P A_L + 2\eta K^2 I(C_{ts}^T C_{ts}) & P B_{ts} \\ B_{ts}^T P & -2\eta \end{bmatrix} \begin{bmatrix} \tilde{x} \\ \Theta C_{ts} \tilde{x} \end{bmatrix} \\ &\quad + 2\tilde{x}^T P B(h + v), \end{aligned} \quad (\text{A.22})$$

where  $K$  denotes the bound on the parameter  $\Theta$ . The term  $\dot{V}$  excluding the input terms  $h$  and  $v$  can further be written as,

$$\begin{bmatrix} \tilde{x} \\ \Theta C_{ts} \tilde{x} \frac{1}{F_0} \end{bmatrix}^T \begin{bmatrix} A_L^T P + P A_L + 2\eta K^2 C_{ts}^T C_{ts} & P \bar{B}_{ts} \\ \bar{B}_{ts}^T P & -2\bar{\eta} \end{bmatrix} \begin{bmatrix} \tilde{x} \\ \Theta C_{ts} \tilde{x} \frac{1}{F_0} \end{bmatrix}.$$

The assumptions  $\eta = \bar{\eta} \frac{1}{F_0^2}$ ,  $\bar{B}_{ts} = \begin{bmatrix} 0 \\ 1 \\ 0 \end{bmatrix}$ ,  $A_L = A + LC$  are made. This set up although

linear in  $P$  and  $\eta$  posed difficulties because the sample profile  $h$  is unknown and requires to be determined. Modeling the sample height input as a disturbance was considered before establishing the design used in this dissertation where the tip-sample interaction force term  $F$  is modeled as a disturbance enabling linear control design.

## A.2 S-PROCEDURE

S-procedure is a technique used for problems with quadratic constraints. It has wide applications in controls, which is explained in great detail along with linear-matrix-inequalities based solutions in book [42]. Firstly, the basics of S-procedure are introduced and then its application to our problem of disturbance rejection is highlighted.

For functions  $F_0$  and  $F_1 \in \mathbf{R}^{n \times n}$  such that  $F_0 = F_0^T$ ,  $F_1 = F_1^T$ , it is straightforward to prove that  $\forall z$ ,

$$z^T F_1 z \geq 0 \Rightarrow z^T F_0 z \geq 0.$$

It is true when  $\exists \tau \in \mathbf{R}$ ,  $\tau \geq 0$  and  $F_0 \geq \tau F_1$ . The converse also holds when constraint qualification,  $\exists$  a point  $\mu$  such that  $\mu^T F_1 \mu > 0$  holds. This result is termed lossless S-procedure. Proof of converse condition is not provided here.

Similarly, in case of strict inequalities if there exists  $\tau \in \mathbf{R}$ ,  $\tau \geq 0$  with  $F_0 > \tau F_1$  then  $\forall z$ ,

$$z^T F_1 z \geq 0, z \neq 0 \Rightarrow z^T F_0 z > 0.$$

Again, the converse holds if  $\exists$  a point  $\mu$  such that  $\mu^T F_1 \mu > 0$  holds.

Using error dynamic equations for  $\tilde{p} = p - \hat{p}$  from (3.9) and assuming a Lyapunov function



of the form  $V = \tilde{p}P\tilde{p}$  with  $P > 0$ , the following is true,

$$\begin{aligned}\dot{V} &= \tilde{x}^T P [A_p \tilde{p} + B_p u_2 + B_p (d - \hat{d})] + [A_p \tilde{p} + B_p u_2 + B_p (d - \hat{d})]^T P \tilde{p}, \\ &= \tilde{p}^T (P A_p + A_p^T P) \tilde{p} + 2 \tilde{p}^T P B_p u_2 + 2 \tilde{p}^T P B_p (d - \hat{d}).\end{aligned}\tag{A.23}$$

Applying mean value theorem to the forces represented as disturbances ( $d$  and  $\hat{d}$ ) as shown in Section 4.2.2, we get

$$d - \hat{d} = \Theta(p - \hat{p}).$$

Here  $\Theta$  is the slope term described in Section 4.2.2. For most applicable force models,  $\Theta$  can be sector-bounded for operating range of separation distances between tip and sample. This reduces to the condition  $(\Theta + \kappa)^T(\Theta - \kappa) \leq 0$  where  $\kappa$  defines the sector bound. Therefore  $u_2$  in (A.23) can be designed using S-procedure and corresponding LMI solution approach. This is a direction of control design that needs further exploration.

## APPENDIX B

# AVERAGING METHODS FOR AMPLITUDE DYNAMICS

Sample profile measurement in an atomic force microscope is done using either the contact mode or the tapping mode. We have considered the constant amplitude or tapping mode measurement technique for our purposes. The amplitude of oscillation changes everytime the cantilever comes across a feature on the sample. The constant amplitude mode of operation aims at maintaining this amplitude of oscillation constant, and the displacement effort required to achieve this gives a measure of the features on the sample.

### B.1 Using Lagrangian equations for $A, \phi$ dynamics

In averaging methods like KBM the input  $h(t)$  is assumed to be constant and therefore these methods are reliable only for  $h(t)$  up to a frequency of 2KHz. Assuming that the solution of the non-linearly perturbed system will be of the form  $p(t) = a \cos(\omega t + \phi)$ , the Lagrangian dynamics procedure was followed to derive the second order dynamic equations in  $a$  and  $\phi$ .

#### B.1.1 Second order equations

$$\begin{aligned} a_1 &= a \\ \dot{a}_1 &= a_2 \\ \dot{a}_2 &= a_1 \omega^2 + 2a_1 \omega \phi_2 + a_1 \phi_2^2 - a_1 \omega_n^2 + \omega_n^2 b \cos(\phi_1) - 2\zeta \omega_n a_2 \\ &\quad + \frac{1}{\pi m} \int_0^{2\pi} F(a_1 \sin(\theta) - h - v) \sin(\theta) d\theta \end{aligned}$$

$$\begin{aligned}
\phi_1 &= \phi \\
\dot{\phi}_1 &= \dot{\phi}_2 \\
\dot{\phi}_2 &= -2\frac{a_2}{a_1}\omega - 2\frac{a_2}{a_1}\phi_2 - \frac{\omega_n^2 b \sin(\phi)}{a_1} - 2\zeta\omega_n(\omega + \phi_2)
\end{aligned}$$

In the above equations,  $\theta = \omega t + \phi_1$ .

### B.1.2 Reduced - first order

The equations in the previous section have been reduced to the following form after eliminating the second order terms. These under some additional constraints are similar to KBM.

$$\begin{aligned}
2a\omega\dot{\phi} &= -a\omega^2 + a\omega_n^2 - \omega_n^2 b \cos(\phi) + 2\zeta\omega_n\dot{a} - \frac{1}{\pi m} \int_0^{2\pi} F(a_1 \sin(\theta) - h - v) \sin(\theta) d\theta \\
\dot{a}\left(\frac{2\omega}{a}\right) &= -\frac{\omega_n^2 b \sin(\phi)}{a} - 2\zeta\omega_n(\omega + \dot{\phi})
\end{aligned}$$

At higher frequencies, this model like the KBM model does not remain valid, that is it does not approximate the cantilever deflection dynamics well.

# REFERENCES

- [1] G. Binnig, C.F.Quate, and C. Gerber, “Atomic force microscope,” *Physical Review Letters*, vol. 56, no. 9, pp. 930–933, March 1986.
- [2] S. Gould, O. Marti, B. Drake, L. Hellemans, C. E. Bracker, H. PK., N. L. Keder, M. M. Eddy, and G. D. Stucky, “Molecular resolution images of amino acid crystals with the atomic force microscope,” *Nature*, vol. 332, no. 22, pp. 332–334, March 1988.
- [3] B. Drake, C. Prater, A. Weisenhorn, S. Gould, T. Albrecht, C. Quate, D. Cannell, H. Hansma, and P. Hansma, “Imaging crystals, polymers, and processes in water with the atomic force microscope,” *Science*, vol. 243, no. 4898, pp. 1586–1589, March 1989.
- [4] R. Garcia and R. Perez, “Dynamic atomic force microscopy methods,” *Surf. Sci. Rep.*, vol. 47, p. 197, 2002.
- [5] F. Giessibl, S. Hembacher, H. Bielefeldt, and J. Mannhart, “Subatomic features on the silicon (111)-(77) surface observed by atomic force microscopy,” *Science*, vol. 289, no. 5478, pp. 422–425, July 2000.
- [6] C. Lee and S. Salapaka, “Fast robust nanopositioning - a linear-matrix-inequalities-based optimal control approach,” *IEEE/ASME Transactions on Mechatronics*, vol. 14, no. 4, pp. 414–422, August 2009.
- [7] S. Salapaka, T. De, and A. Sebastian, “A robust control based solution to the sample-profile estimation problem in fast atomic force microscopy,” *International Journal of Robust and Nonlinear Control*, vol. 15, pp. 821–837, 2005.
- [8] G. Fantner, G. Schitter, and et. al. J.H. Kindt, “Components for high speed atomic force microscopy,” *Ultramicroscopy*, vol. 106, no. 8, pp. 881–887, 2006.
- [9] K. Leang and A. Fleming, “High speed afm scanner: Design and drive considerations,” in *American Control Conference*, 2008, pp. 3188–3193.
- [10] S. Polit and J. Dong, “Design of high-bandwidth high-precision flexure-based nanopositioning modules,” *Journal of Manufacturing Systems*, 2010.
- [11] D. A. Walters, J. P. Cleveland, N. H. Thomson, P. K. Hansma, M. A. Wendman, G. Gurley, and V. V. Elings, “Short cantilevers for atomic force microscopy,” *Review of Scientific Instruments*, vol. 67, pp. 3583 – 3590, Oct 1996.

- [12] M. Kitazawa, K. Shiotani, and A. Toda<sup>1</sup>, “Batch fabrication of sharpened silicon nitride tips,” *Japanese Journal of Applied Physics*, vol. 42, pp. 4844–4847, 2003.
- [13] T. Ando, “High-speed atomic force microscopy coming of age,” *Nanotechnology*, vol. 23, p. 27, January 2012.
- [14] T. Sulchek, S. C. Minne, J. D. Adams, D. A. Fletcher, A. Atalar, C. F. Quate, and D. M. Adderton, “Dual integrated actuators for extended range high speed atomic force microscopy,” *Applied Physics Letters*, vol. 75, no. 11, p. 1637, July 1999.
- [15] T. Ando, N. Kodera, E. Takai, D. Maruyama, K. Saito, and A. Toda, “A high-speed atomic force microscope for studying biological macromolecules,” *Proceedings of the National Academy of Sciences*, vol. 98, no. 22, p. 034106, 2001.
- [16] T. Ando, T. Uchihashia, and T. Fukumac, “High-speed atomic force microscopy for nano-visualization of dynamic biomolecular processes,” *Progress in Surface Science*, vol. 83, no. 7-9, pp. 337–437, November 2008.
- [17] L. M. P. et al, “Breaking the speed limit with atomic force microscopy,” *Nanotechnology*, vol. 18, no. 4, 2007.
- [18] M. H. Despont, U. Drechsler, U. T. Dürig, W. Häberle, M. I. Lutwyche, H. E. Rothuizen, R. Stutz, R. Widmer, and G. K. Binnig, “The “millipede”—more than thousand tips for future afm storage,” *IBM Journal of Research and Development*, vol. 44, no. 3, pp. 323–340, May 2000.
- [19] S. Salapaka, A. Sebastian, J. P. Cleveland, and M. V. Salapaka., “High bandwidth nano-positioner: A robust control approach,” *IEEE Transactions on Control Systems Technology*, vol. 73, pp. 3232–3241, March 2002.
- [20] G. Schitter, F. Allgower, and A. Stemmer, “A new control strategy for high-speed atomic force microscopy,” *Nanotechnology*, vol. 15, no. 1, 2004.
- [21] S. Salapaka, T. De, and A. Sebastian, “Sample-profile estimate for fast atomic force microscopy,” *Applied Physics Letters*, vol. 87, no. 5, 2005.
- [22] C. Lee and S. Salapaka, “Fast imaging with alternative signal for dynamic atomic force microscopy,” *Applied Physics Letters*, vol. 97, no. 13, 2010.
- [23] D. Sahoo, A. Sebastian, and M. V. Salapaka, “Transient-signal-based sample-detection in atomic force microscopy,” *Applied Physics Letters*, vol. 83, no. 26, pp. 5521–5523, December 2003.
- [24] D. Sahoo, A. Sebastian, and M. V. Salapaka, “Harnessing the transient signals in atomic force microscopy,” *International Jorunal of Robust and Nonlinear Control*, vol. 15, pp. 805–820, 2005.

- [25] D. Sahoo, P. Agarwal, and M. V. Salapaka, “Transient force atomic force microscopy: A new nano-interrogation method,” in *American Control Conference*, 2007, pp. 2136–2140.
- [26] G. Schitter, “Field programmable analog array (fpaa) based control of an atomic force microscope,” in *Proceedings of American Control Conference*, June 2008, pp. 2690 – 2695.
- [27] K. Johnson, K. Kendall, and A. Roberts, “Surface energy and the contact of elastic solids,” *Proceedings of the Royal Society, Lond.A*, vol. 324, no. 1558, pp. 301–313, September 1971.
- [28] B. Derjaguin, V. Muller, and Y. Toropov, “Effect of contact deformations on the adhesion of particles,” *Journal of Colloid and Interface Science*, vol. 53, no. 2, pp. 314–326, November 1975.
- [29] H. Pollock, D. Maugis, and M. Barquins, “The force of adhesion between solid surfaces in contact,” *Applied Physics Letters*, vol. 33, no. 9, pp. 798–799, November 1978.
- [30] K. Zhou, J. Doyle, and K. Glover, *Robust and Optimal Control*. Prentice Hall, Upper Saddle River, NJ 07458, 1996.
- [31] C. Scherer, P. Gahinet, and M. Chilali, “Multiobjective output-feedback control via lmi optimization,” *Automatic Control, IEEE Transactions on*, vol. 42, no. 7, pp. 896–911, July 1997.
- [32] G. Dullerud and F. Paganini, *A Course in Robust Control Theory: A Convex Approach*. Springer-Verlag, 2000.
- [33] R. Garcia and A. S. Paulo, “Attractive and repulsive tip sample interaction regimes in tapping mode atomic force microscopy,” *Phys. Rev. B*, vol. 60, no. 7, pp. 4961–4967, August 1999.
- [34] G. Mohan, C. Lee, and S. Salapaka, “Control techniques for high-speed dynamic mode imaging in atomic force microscopes,” in *Proceedings of the 50th IEEE Conference on Decision and Control and European Control Conference, CDC-ECC 2011, Orlando, FL, USA*, 2011, pp. 651–656.
- [35] J. Doyle, B. Francis, and A. Tannenbaum, *Feedback Control Theory*. New York: MacMillan, 1992.
- [36] P. Maivald, H. Butt, S. Gould, C. B. Prater, B. Drake, J. Gurley, V. Elings, and P. Hansma, “Using force modulation to image surface elasticities with the atomic force microscope,” *Nanotechnology*, vol. 2, pp. 103–106, February 1991.
- [37] M. Stark, R. Guckenberger, A. Stemmer, and R. Stark, “Estimating the transfer function of the cantilever in atomic force microscopy: A system identification approach,” *Journal of Applied Physics*, vol. 98, pp. 114 904–114 904–7, December 2005.

- [38] F. Giessibl, “A direct method to calculate tip-sample forces from frequency shifts in frequency-modulation atomic force microscopy,” *Applied Physics Letters*, vol. 78, no. 1, January 2001.
- [39] P. A. Yuya, D. C. Hurley, and J. A. Turner, “Contact-resonance atomic force microscopy for viscoelasticity,” *Journal of Applied Physics*, vol. 104, no. 7, pp. 074 916–074 916–7, June 2009.
- [40] P. Agarwal and M. V. Salapaka, “Real time estimation of equivalent cantilever parameters in tapping mode atomic force microscopy,” *Applied Physics Letters*, vol. 95, no. 8, pp. 083 113–083 113–3, September 2009.
- [41] J. Sader, “Frequency response of cantilever beams immersed in viscous fluids with application to the atomic force microscope,” *Journal of Applied Physics*, vol. 84, no. 1, pp. 64–76, 1998.
- [42] S. Boyd, L. E. Ghaoui, E. Feron, and V. Balakrishnan, *Linear Matrix Inequalities in System and Control Theory*. SIAM Studies in Applied Mathematics, 1994.